

DOCTORAL THESIS

Electrochemical Reduction of Oxygen on Platinum-Modified Carbon Materials

Erkin Najafli

TALLINN UNIVERSITY OF TECHNOLOGY
DOCTORAL THESIS
33/2025

Electrochemical Reduction of Oxygen on Platinum-Modified Carbon Materials

ERKIN NAJAFLI



TALLINN UNIVERSITY OF TECHNOLOGY

School of Engineering

Department of Materials and Environmental Technology

This dissertation was accepted for the defence of the degree 15/04/2025

Supervisor:

Dr. Ivar Kruusenberg
National Institute of Chemical Physics and Biophysics
Tallinn, Estonia

Co-supervisor:

Dr. Sander Ratso
National Institute of Chemical Physics and Biophysics
Tallinn, Estonia

Opponents:

Prof Lior Elbaz
Faculty of Exact Sciences
Department of Chemistry
Bar-Ilan University
Ramat-Gan, Israel

Prof Nadežda Kongi
Chair of Colloidal and Environmental Chemistry
Institute of Chemistry
University of Tartu
Tartu, Estonia

Defence of the thesis: 10/06/2025, Tallinn

Declaration:

Hereby I declare that this doctoral thesis, my original investigation and achievement, submitted for the doctoral degree at Tallinn University of Technology has not been submitted for doctoral or equivalent academic degree.

Erkin Najafli



signature

Copyright: Erkin Najafli, 2025

ISSN 2585-6898 (publication)

ISBN 978-9916-80-291-5 (publication)

ISSN 2585-6901 (PDF)

ISBN 978-9916-80-292-2 (PDF)

DOI <https://doi.org/10.23658/taltech.33/2025>

Printed by Koopia Niini & Rauam

Najafli, E. (2025). *Electrochemical Reduction of Oxygen on Platinum-Modified Carbon Materials* [TalTech Press]. <https://doi.org/10.23658/taltech.33/2025>

TALLINNA TEHNIKAÜLIKOOL
DOKTORITÖÖ
33/2025

**Elektrokeemiline hapniku redutseerumine
platinaga modifitseeritud
süsinikmaterjalidel**

ERKIN NAJAFLI



Contents

List of publications	6
Author's contribution to the publications	7
Introduction	8
Abbreviations and symbols	9
1 Literature review	11
1.1 Proton exchange membrane fuel cells	11
1.2 Oxygen reduction reaction	12
1.3 Oxygen reduction reaction on Pt electrocatalysts	12
1.4 Carbon nanomaterials as support for Pt electrocatalysts	13
1.5 Synthesis of CO ₂ -derived carbon nanomaterials	14
1.6 Strategies to make ORR electrocatalysts cost-effective	15
1.7 Carbon support modification techniques	17
2 Aims of the thesis and research questions	18
3 Experimental	19
3.1 Pretreatment and N-doping of XC	19
3.2 Synthesis of XC-supported electrocatalysts	19
3.3 Synthesis of CO ₂ -derived carbon	19
3.4 Synthesis of CO ₂ -derived carbon supported electrocatalysts	20
3.5 Pretreatment of CO ₂ -derived carbon	20
3.6 Synthesis of pretreated CO ₂ -derived carbon supported electrocatalysts	20
3.7 Electrochemical characterization	20
3.8 Physical characterization	22
4 Results and discussion	24
4.1 Electrochemical reduction of oxygen on platinum supported with pretreated Vulcan XC-72	24
4.2 Electrochemical reduction of oxygen on platinum supported with CO ₂ -derived carbon	32
4.3 Electrochemical reduction of oxygen on platinum supported with pretreated CO ₂ -derived carbon	44
5 Conclusions	57
References	58
Acknowledgements	67
Abstract	68
Lühikokkuvõte	69
Appendix 1	71
Appendix 2	83
Appendix 3	95
Curriculum vitae	111
Elulookirjeldus	112

List of publications

The list of author's publications, on the basis of which the thesis has been prepared:

- I **Erkin Najafli**, Maarja Grossberg, Valdek Mikli, Peter Walke, Sander Ratso, Ivar Kruusenberg, Optimizing Pt Catalyst Performance for Oxygen Reduction Reaction via Surface Functionalization of Vulcan XC-72R Carbon Black Support *Journal of Applied Electrochemistry* 2025, in press. DOI: 10.1007/s10800-024-02238-1.
- II **Erkin Najafli**, Sander Ratso, Yurii P. Ivanov, Matija Gatalo, Luka Pavko, Can Rüstü Yörük, Peter Walke, Giorgio Divitini, Nejc Hodnik, and Ivar Kruusenberg, Sustainable CO₂-Derived Nanoscale Carbon Support to a Platinum Catalyst for Oxygen Reduction Reaction *ACS Applied Nano Materials* 2023 6 (7), 5772–5780 DOI: 10.1021/acsanm.3c00208
- III **Erkin Najafli**, Sander Ratso, Amir Foroozan, Navid Noor, Drew C. Higgins, and Ivar Kruusenberg, Functionalization of CO₂-Derived Carbon Support as a Pathway to Enhancing the Oxygen Reduction Reaction Performance of Pt Electrocatalysts *Energy & Fuels* 2024 38 (16), 15601–15610 DOI: 10.1021/acs.energyfuels.4c02407

Author's contribution to the publications

Contribution to the papers in this thesis are:

- I The author conducted the synthesis of the electrocatalyst materials and carried out all the electrochemical measurements, followed by data analysis. Additionally, the author interpreted the results from the electrochemical measurements and contributed to the manuscript writing.
- II The author conducted the synthesis of the electrocatalyst materials and carried out all the electrochemical measurements, followed by data analysis. Additionally, the author interpreted the results from the electrochemical measurements and contributed to the manuscript writing.
- III The author conducted the synthesis of the electrocatalyst materials and carried out all the electrochemical measurements, followed by data analysis. Additionally, the author interpreted the results from the electrochemical measurements and contributed to the manuscript writing.

Introduction

According to the Intergovernmental Panel on Climate Change report, human-induced global warming has already reached roughly 1 °C in 2017 and it has led to many changes on the planet including extreme weather events, droughts, floods, sea level rise and biodiversity loss [1]. The development of clean energy technologies to reduce greenhouse gas emissions is among the proposed solutions for limiting the magnitude of future warming [2].

One of the promising clean energy technologies is the fuel cell which is a device used for converting chemical energy into electricity. The advantages of fuel cells include portability, almost zero pollution, high power density and quiet operation [3]. While a fuel cell can be used to convert the chemical energy of hydrogen to electricity, its operation requires an electrocatalyst which is typically platinum supported with a carbon material [4]. Due to the high cost and scarcity of platinum, the development of electrocatalysts with low platinum loading is highly desirable for the commercialization of fuel cells powered by hydrogen fuel. At the same time, carbon material used as support for Pt is commonly petroleum-sourced, thus the emergence of alternatives such as CO₂-derived carbon is equally important for sustainability. Synthesis of such support materials with tunable properties also enables nanoengineering which in turn results in better catalyst performance allowing lower Pt loading. These advances are among the key prerequisites for achieving affordable and scalable fuel cell technology to help with the decarbonization of sectors most responsible for greenhouse gas emissions.

This thesis studies the synthesis of CO₂-derived carbon as support material for Pt electrocatalyst and investigates various carbon pretreatment methods to enhance the performance of the electrocatalyst for the cathodic reaction of hydrogen fuel cells. The first chapter of the thesis is a review of the literature on the topic. In the second chapter, the aims of the study are described. The third and fourth chapters provide experimental details of the study and a discussion of the results, respectively. The thesis is based on three peer-reviewed publications [5], [6], [7].

Abbreviations and symbols

DC	Direct current
PAFC	Phosphoric acid fuel cell
SOFC	Solid oxide fuel cell
MCFC	Molten carbonate fuel cell
DMFC	Direct methanol fuel cell
AFC	Alkaline fuel cell
PEMFC	Proton exchange membrane fuel cell
MEA	Membrane electrode assembly
GDL	Gas diffusion layer
HOR	Hydrogen oxidation reaction
ORR	Oxygen reduction reaction
PEM	Proton exchange membrane
η	Overpotential
PGM	Platinum group metal
Pt/C	Platinum electrocatalyst with carbon black support
XC	Vulcan XC-72
CCU	Carbon capture and utilization
MSSC-ET	Molten salt CO ₂ capture and electrotransformation
CO ₂ -C	CO ₂ -derived carbon nanomaterials
PTFE	Polytetrafluoroethylene
DCDA	Dicyandiamide
PVP	Polyvinylpyrrolidone
EG	Ethylene glycol
RDE	Rotating disk electrode
RHE	Reversible hydrogen electrode
CV	Cyclic voltammetry
EASA	Electrochemically active surface area
RPM	Revolutions per minute
EIS	Electrochemical impedance spectroscopy
OCV	Open circuit voltage
ADT	Accelerated durability test
KL	Koutecký-Levich
j	Measured current density
j_k	Kinetic current density
j_d	Diffusion-limited current density
n	Overall number of electrons transferred per O ₂ molecule
k	Electron transfer rate constant
F	Faraday constant
D_{O_2}	Diffusion coefficient of oxygen

ν	Kinematic viscosity of the electrolyte
ω	Angular velocity of the rotating disk
C_{O_2}	Bulk concentration of oxygen
b	Tafel slope
$\log j$	Logarithm of the current density
$Q_{H-adsorption}$	Estimated hydrogen adsorption charge
L_{Pt}	Working electrode Pt loading
A_g	Geometric surface area of the working electrode
$Q_{CO-oxidation}$	Estimated CO oxidation charge
E_{onset}	Onset potential of ORR
$E_{1/2}$	Half-wave potential of ORR
SEM	Scanning electron microscopy
STEM	Scanning transmission electron microscopy
FEG	Field emission gun
EDS	Energy-dispersive x-ray spectroscopy
FFT	Fast fourier transform
IFFT	Inverse fast fourier transform
XRD	X-ray diffraction
BWF	Breit-Wigner-Fano
XPS	X-ray photoelectron spectroscopy
BE	Binding energy
BET	Brunauer-Emmett-Teller
QSDFT	Quenched solid density functional theory
TGA	Thermogravimetric analysis
I_D	Intensity of D-band in Raman spectra
I_G	Intensity of G-band in Raman spectra
I_D/I_G	Ratio of D-band and G-band intensities in Raman spectra
GFWHM	Full width at half-maximum for G peak
DFWHM	Full width at half-maximum for D peak
S_{BET}	BET surface area
S_{DFT}	Specific surface area
V_p	Total pore volume
d_p	Average pore diameter
QSDFT	Quenched solid density functional theory
HR-TEM	High-resolution transmission electron microscopy
HUPD	Hydrogen underpotential deposition
E_O^{ads}	Oxygen adsorption energy
E_O^{des}	Oxygen desorption energy
OH_{ads}	Adsorbed hydroxide

1 Literature review

1.1 Proton exchange membrane fuel cells

A fuel cell is an electrochemical device used for continuous conversion of chemical energy to electrical energy. This is achieved by using two electrodes, namely cathode and anode separated by an electrolyte to drive the desired reaction in which the fuel such as hydrogen is supplied to the cathode and an oxidant (e.g. oxygen) is fed to the anode compartment. The main function of the electrolyte is to block the flow of electrons while permitting ions to move through. Thus, the electrons are forced to move to the cathode via an external circuit producing DC (direct current) electricity. The fuel cells are commonly classified based on the type of electrolyte and fuel used in them as well as their operating temperature. The main types of fuel cells are listed below [8]:

- a) Fuel cells with high operating temperature (above 100 °C):
Phosphoric acid fuel cells (PAFC), solid oxide fuel cells (SOFC), molten carbonate fuel cells (MCFC)
- b) Fuel cells with low operating temperature:
Direct methanol fuel cells (DMFC), alkaline fuel cells (AFC) and proton exchange membrane fuel cells (PEMFC).

Also known as polymer electrolyte membrane fuel cell, PEMFC has received considerable interest from researchers in the field of energy engineering due to its promising features such as high-power density and low operating temperature that are attractive for both stationary and portable applications [9]. The core of the PEMFC technology is a membrane electrode assembly (MEA) that consists of a gas diffusion layer (GDL), a catalyst layer and, a proton exchange membrane [10], [11] as depicted in Figure 1.

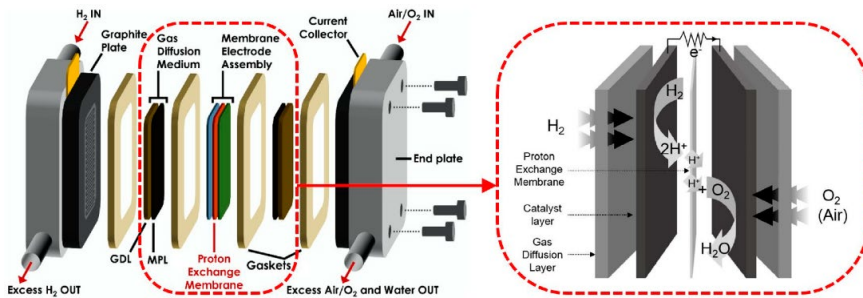
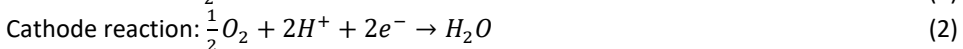


Figure 1. The structure and working mechanism of PEMFC [11].

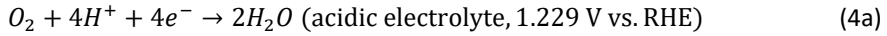
In PEMFC, hydrogen is fed into the anode as fuel to undergo a hydrogen oxidation reaction (HOR) releasing protons that move to the cathode through the membrane and electrons that are transported to the cathode via an external circuit. On the other hand, air or oxygen is supplied to the cathode compartment where oxygen atoms are electrochemically reduced to form water in an oxygen reduction reaction (ORR) when they react with the incoming protons and electrons. These half-reactions and the overall reaction are given below:



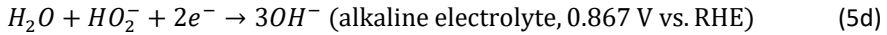
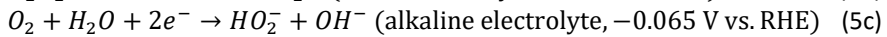
1.2 Oxygen reduction reaction

Compared to the anodic reaction of hydrogen oxidation, the oxygen reduction reaction in the cathode is more than six orders slower due to the high bond energy (498 kJ mol^{-1}) of molecular oxygen [12]. While the exact reaction pathway for ORR is unknown, commonly two pathways based on the number of transferred electrons are considered [13], [14]:

- a) 4–electron pathway in which molecular oxygen is directly reduced to water (or OH^-) in the acidic (or alkaline) electrolyte as shown in the below reactions:



- b) 2–electron pathway in which molecular oxygen is partially reduced to H_2O_2 (or HO_2^-) in the acidic (or alkaline) electrolyte as shown in the below reaction:



Here reactions 4a, 5a and 5b refer to ORR in acidic electrolyte and 4b, 5c and 5d refer to ORR in alkaline electrolyte. In PEMFCs, reactions in acidic electrolyte are relevant as proton exchange membrane (PEM) is used.

Typically, in PEMFCs the 4–electron pathway is preferred over the 2–electron pathway due to the efficiency of direction reduction and the absence of hydrogen peroxide which can damage the cell components [15].

1.3 Oxygen reduction reaction on Pt electrocatalysts

Due to the sluggish kinetics of cathodic ORR, an efficient electrocatalyst is required to accelerate the reaction by reducing the reaction overpotential, which is the extra potential beyond equilibrium potential needed to drive the reaction at a desired rate (η). In the case of fuel cells, this means that when the overpotential is large, the output voltage of a fuel cell is reduced as significant potential is lost to different overpotential sources such as activation energy of the reaction, ohmic losses due to resistance in the conductive fuel cell components and mass transport losses originating from reactant depletion or product accumulation at the electrode surface [16], [17]. Among these overpotential sources, the activation overpotential that originates from slow cathodic reaction kinetics is the most significant contributor to the total overpotential in a typical PEMFC [18]. In this work, the aim is to develop an active and durable electrocatalyst to reduce the activation overpotential of ORR, thereby significantly reducing potential losses for achieving efficient operation of PEMFC. A common method to find high–performance electrocatalyst materials for ORR is by using a descriptor–based approach where ORR descriptors such as binding energy of oxygen or hydroxyl to electrocatalyst are chosen as the most important properties linked to high electrocatalyst activity [19]. This can be explained by the Sabatier principle which states that the binding energy between the electrocatalyst and the reactant should be neither too strong nor too weak [20]. When different electrocatalysts are plotted based on these criteria, a certain ORR activity trend can be observed as shown in Figure 2 below.

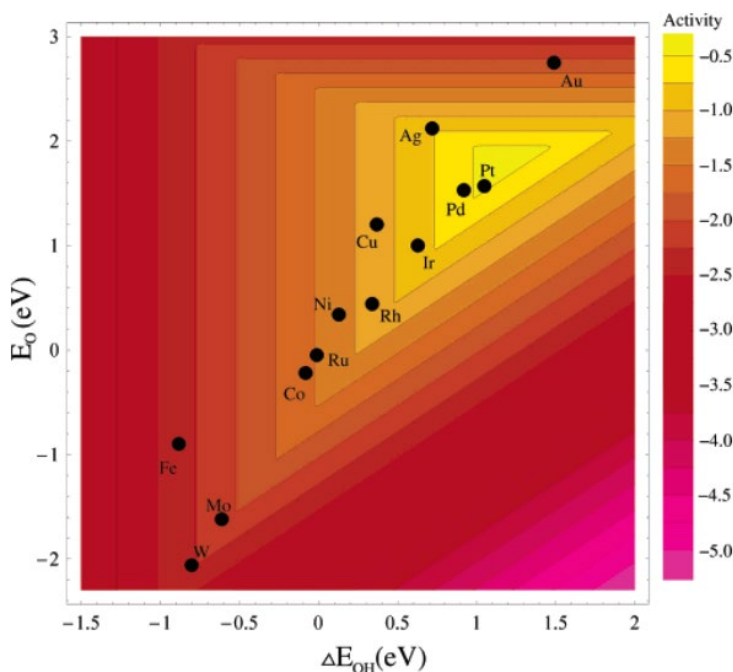


Figure 2. Trends in oxygen reduction activity plotted as a function of both the O and the OH binding energy [21].

Although oxygen binding energy is not the only important descriptor for ORR catalytic activity, when it is chosen as the main descriptor, Pt is found to be the best electrocatalyst for ORR. This agrees well with the experimental data as Pt-based electrocatalysts are considered the best-performing among all currently available electrocatalysts [22]. However, the usage of Pt electrocatalysts in PEMFCs is also one of the major concerns regarding the technology as Pt being a scarce and expensive metal accounts for about 40–55% of the overall cost of a fuel cell stack [23]. When considering the application of fuel cells only in the road transport sector (for electric vehicles), by 2050 up to 0.2 g kW^{-1} decrease is needed in the platinum content of fuel cells to keep the stock of platinum reserves positive [24]. Currently, Pt loading for PEMFCs is around 0.2 g kW^{-1} and this highlights the significant and urgent need for cutting the amount of Pt used in PEMFC stacks [25].

1.4 Carbon nanomaterials as support for Pt electrocatalysts

The high cost and scarcity associated with Pt electrocatalysts have led to the emergence of support materials that host well-dispersed Pt nanoparticles resulting in the efficient use of Pt loading [26]. The choice of support material is crucial as it can also directly influence the electrochemical activity, stability and overall performance of the electrocatalyst in PEMFC due to direct participation in the reaction steps or metal-support interaction [27], [28]. Given the challenging reaction conditions in a PEMFC, there are certain requirements for the support material: i) high electronic conductivity; ii) high electrochemical stability; iii) high specific surface area; iv) strong interaction with the metal electrocatalyst; and v) convenient recovery of metal particles from the material [29]. Carbon-based support materials and especially carbon black are

commonly used as support for Pt electrocatalysts (abbreviated as Pt/C) due to many advantages including high specific surface area, good electrical conductivity and relatively low cost [27], [30]. While the first generation of commercial Pt/C electrocatalysts used Vulcan XC-72 (shortly XC) as support, other carbon black supports such as Ketjenblack, Black Pearls and Shawinigan have been developed as well [30], [31]. Despite many advantages of conventional carbon black as a support material, it is also known to be unstable at high potentials due to weak Pt-C interactions and carbon oxidation which can result in the detachment of Pt nanoparticles [28], [32]. As a result of this, the improvement of carbon black support is an active research field and in addition to carbon black, other commonly studied carbon support nanomaterials for fuel cells include carbon nanotubes [33], diamond [34], graphite [35] and graphene [36].

1.5 Synthesis of CO₂-derived carbon nanomaterials

As a clean energy technology, PEMFCs produce very low or zero pollutant emissions during operation because the only reaction byproducts are heat and water [37], [38]. However, this is not the case for carbon black nanomaterials due to significant CO₂ emissions associated with their production. For instance, Vulcan XC-72 is a type of carbon black called “furnace black” referring to the manufacturing method where it is produced by vaporizing and pyrolyzing natural gas and aromatics oils in a furnace [39]. It has been estimated that the production of each tonne of furnace black carbon emits around 2.62 tonnes of CO₂ [40]. To ensure the sustainability of commercial PEMFC manufacturing, there is a need for development of alternative carbon support nanomaterials produced with low or zero CO₂ footprint.

This aligns well with the promise of the carbon capture and utilisation (CCU) concept which aims to capture and transform CO₂ into valuable products such as fuels and value-added chemicals via techniques such as thermochemical, electrochemical and photocatalytic transformation [41]. Compared with the other two techniques, the electrochemical transformation of CO₂ has the major advantage of using excess electrical energy coming from intermittent renewable energy sources as well as operating under milder conditions [42], [43]. While CO₂ electrochemical transformation can be performed in other electrolytes such as ionic liquids [44], solid electrolytes [45] and aqueous solution [46], high-temperature molten salts are advantageous due to their low cost, abundance, high ionic conductivity, wide electrochemical window and low vapour pressure [47].

Molten salt CO₂ capture and electrotransformation (MSCC-ET) is a technique based on a molten salt electrolyte that can produce carbon, carbon monoxide or syngas depending on the operational conditions and feeding gas via the following reactions [47]:



In reactions 6 and 7, metal carbonates (M_xCO₃) in the molten salt electrolyte are reduced to carbon while these reactions can also produce carbon monoxide as shown in reactions 6a and 7a. The anodic reaction determines if reaction 6 or 7 occurs. Furthermore,

produced CO can also undergo further reduction to produce C (reaction 8). CO₂ is typically flown through or onto the salt mixture, where it undergoes a rapid reaction with the dissolved oxides (reaction 9) to regenerate carbonates ensuring a sustainable process. It has been reported that thermodynamically C is the favoured product when electrochemical CO₂ reduction is conducted at low temperatures in molten carbonates mixture [48]. Being the most common eutectic carbonate mixture for the MSCC-ET process, Li₂CO₃-Na₂CO₃-K₂CO₃ (43.5:31.5:25 mol%) is generally used for carbon production due to its relatively low melting point of 393 °C and large electrochemical window [47], [49]. It is also known that the morphology and structure of the produced carbon can be tuned by varying the salt composition, temperature, voltage and electrode material of molten carbonate salts [50], [51]. This creates an opportunity to optimize the MSCC-ET technique for producing CO₂-derived carbon nanomaterials (shortly CO₂-C) with desired properties to be used as a support material for Pt electrocatalysts.

1.6 Strategies to make ORR electrocatalysts cost-effective

Several strategies have been developed by researchers to alleviate the high cost associated with Pt usage in ORR electrocatalysts. The main purpose of such strategies is to reduce Pt loading in the electrocatalyst or replace it with non-precious metal or metal-free electrocatalysts without sacrificing the ORR performance. For Pt-based electrocatalysts, the main approaches include tuning the size, shape and structure of metal nanoparticles, making alloys and modification of support materials [52], [53], [54], [55]. These approaches can further be classified into two types with distinct pathways to reach the same goal: increasing the number of active sites and increasing the intrinsic activity of the electrocatalyst (see Figure 3).

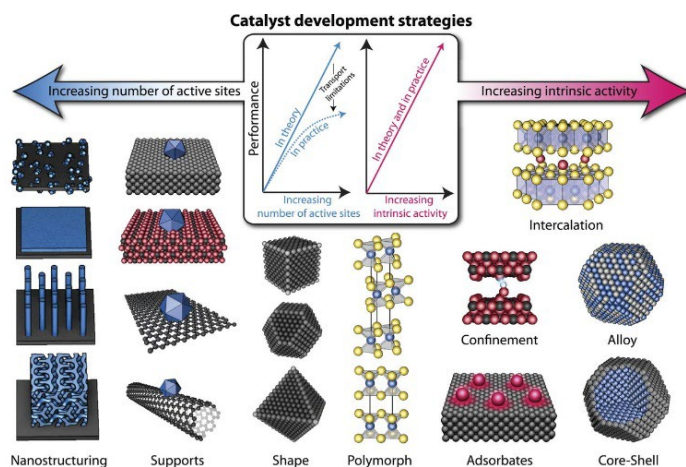


Figure 3. A diagram illustrating different types of electrocatalyst development approaches [32].

For supported Pt electrocatalysts, nanoparticle size control (nanostructuring) is particularly interesting as a certain Pt nanoparticle size window has been identified by many researchers to be optimal for achieving enhanced ORR activity [56], [57], [58], [59], [60]. For instance, Gan et al. has reported that Pt nanoparticles sized below 1.7 nm are often trapped in support micropores resulting in loss in electrocatalytic activity while Xu et al. has identified that increase in size of Pt nanoparticles causes drop in fraction of

corner and edge Pt atoms that are associated with strong affinity to oxygen species resulting in improved specific activity and durability [60], [61]. At the same time, as increase in Pt nanoparticle size also decreases EASA, optimal mass activity is reached around 4 nm and this can be used as a useful metric to predict the performance of Pt electrocatalysts [60].

The chosen synthesis method to deposit Pt nanoparticles on pre-treated carbon support is a crucial point in determining the dispersion and size of the deposited nanoparticles. One of the most prevalent methods of Pt/C electrocatalyst synthesis is the “polyol method” owing to its relatively simple and green process which allows tuning the nanoparticle size by changing the synthesis conditions [62]. It can be seen from Figure 4 that the polyol method was dominant among Pt/C synthesis methods over a span of 10 years based on the number of published research articles that preferred it over the other methods. In the polyol method, a polyol which is typically ethylene glycol is used as both solvent and reducing agent. During the synthesis, ethylene glycol is oxidized to glycolic acid by donating electrons to the reduction of metal ions that form metal colloids. In alkaline solutions, glycolic acid dissociates to glycolate anion which was found to be a stabilizing agent that controls the size of deposited Pt particles based on the pH value (which dictates the concentration of glycolate ions in the solution) [63]. Thus, the pH of the ethylene glycol solution can be adjusted to achieve the desired particle size.

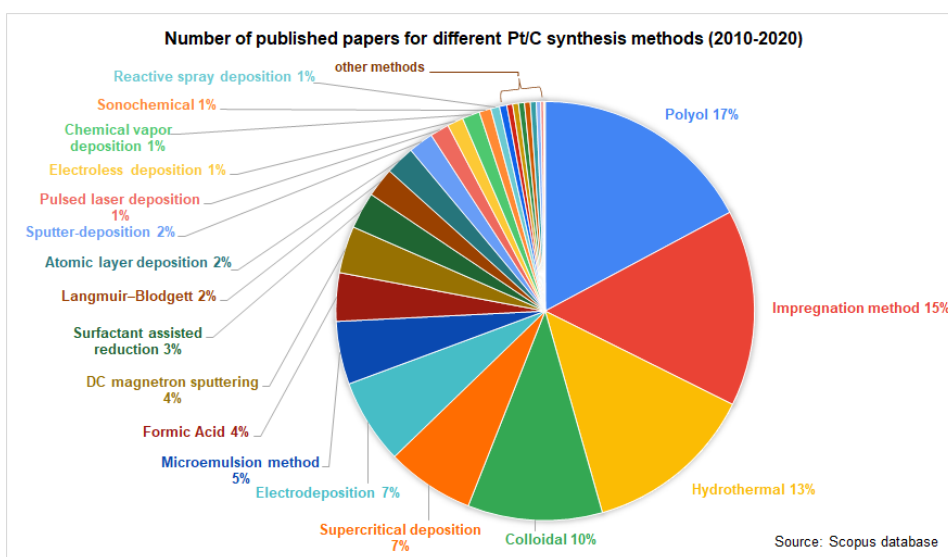


Figure 4. A pie chart showing the prevalence of different Pt/C synthesis methods based on the number of published papers.

While the approaches mentioned above bring unique properties to the synthesized material, they also come with certain disadvantages. For instance, platinum group metal-free (PGM-free) electrocatalysts often result in a thick catalyst layer in MEA that causes mass transport challenges [64], nanostructured electrocatalysts are costly to fabricate and prone to agglomeration [65] and alloy electrocatalysts leach metals gradually [66]. Compared to these approaches, support modification is a more flexible strategy that can be used in synergy with the other approaches and may lead to improvements in ORR performance when using very low Pt loadings. For instance, a combination of support

modification with Pt nanoparticle size control can be a promising strategy to avoid shortcomings of size control such as sintering and detachment of smaller Pt nanoparticles from the support surface via tuning of Pt–C interaction with support modification ensuring the complete exploitation of size control benefits [67].

1.7 Carbon support modification techniques

Apart from being an effective strategy for improving electrocatalyst performance and cost, carbon support modification techniques are becoming increasingly relevant due to concerns about carbon black's stability and its interaction with Pt nanoparticles in demanding PEMFC conditions. Carbon corrosion and detachment of Pt nanoparticles during ORR lead to significant loss in electrochemical performance of carbon-supported Pt electrocatalysts that can be alleviated by support modification [68], [69]. While carbon corrosion is often tackled with corrosion-resistant carbon material selection, Pt nanoparticle detachment has been linked to weak metal–support interaction in which support plays a bifunctional effect (geometric and electronic) [69], [70]. Strong metal–support interaction has been shown to prevent aggregation, dissolution and migration of metal nanoparticles leading to improved durability as well as facilitate the electron transfer between support and metal nanoparticle causing enhanced ORR activity [71]. Thus, both careful selection and development of carbon nanomaterials with desired geometrical and electronical properties are essential for increasing the electrocatalytic activity of carbon-supported Pt electrocatalysts.

Typical carbon black support modification techniques for PEMFC application include surface functionalization (often with oxygen and nitrogen functional groups) [72], heat treatment such as steam-etching [73], silica coating [74] and gas or plasma-phase treatment [75]. Surface functionalization methods can be further classified into oxidation, polymer grafting, impregnation and covalent functionalization [72].

Particularly, carbon black oxidation is a widely researched method that can be performed in wet conditions and in dry conditions (e.g. ozone or reactive plasma oxidation) [30], [76]. Strong acids and oxidants can be used for liquid-phase oxidation [76]. When oxygen functional groups are attached to the carbon surface after liquid-phase oxidation, they can act as anchoring points for Pt nanoparticles and improve the metal–support interaction by making the carbon more hydrophilic due to modified acid–base and redox properties [77]. For instance, carboxyl (COOH), hydroxyl (COH), and carbonyl (C=O) groups can disrupt sp² hybridization to cause more free electrons that can interact with Pt cations during electrocatalyst synthesis [78]. At the same time, increased hydrophilicity of carbon allows easier access to aqueous metal precursors and less acidic groups further optimizing the metal–support interaction ensuring less sintering and better dispersion for Pt nanoparticles [79].

In addition to the surface chemistry of carbon supports, their surface area and porosity are also important characteristics that need to be considered during support modification. While higher surface area carbon support is preferred to achieve well-dispersed and well-anchored metal particles [80], it can be disadvantageous if a large part of the surface area is composed of micropores as they can trap metal particles and block access to reactants [28]. However, when the carbon is macroporous, this can decrease the surface area and decrease the electrical conductivity of the material [77]. Thus, the chosen support modification technique should allow for tuning the microstructure of the carbon support to facilitate mass transport while serving as an efficient carrier for deposited electrocatalyst particles.

2 Aims of the thesis and research questions

The aim of this work is to develop novel Pt electrocatalysts supported with CO₂-derived carbon nanomaterial for ORR in PEMFCs. Such high-performance electrocatalysts with low Pt loading and sustainable support material are necessary for advancing the PEMFC technology for decarbonization goals. To achieve this aim, the work is divided into three parts with individual objectives:

- 1) The influence of pretreatment on electrocatalyst support material is first studied on commercial Vulcan XC-72 carbon black. The objective is to find a promising support pretreatment method that would result in enhanced ORR performance for Pt electrocatalyst [I].
- 2) The possibility of using CO₂-derived carbon nanomaterial instead of commercial carbon black support is studied. The objective is to synthesize a Pt electrocatalyst with CO₂-derived carbon support and compare its ORR performance with a commercial Pt/C electrocatalyst [II].
- 3) The influence of pretreatment on CO₂-derived carbon support is studied. The objective is to combine the findings from previous parts of the work and to develop a novel Pt electrocatalyst supported with pretreated CO₂-derived carbon support that exhibits superior ORR performance compared to the electrocatalyst with untreated CO₂-derived carbon support [III].

Based on the established objectives, research questions can be formulated as follows:

- 1) Which support pretreatment method is the most effective in enhancing the ORR performance for Pt electrocatalyst supported with commercial Vulcan XC-72 carbon?
- 2) Can CO₂-derived carbon nanomaterial replace commercial carbon black as a support material for Pt electrocatalyst while retaining promising ORR performance?
- 3) Can the optimal pretreatment method identified for Vulcan XC-72 carbon be applied to CO₂-derived carbon support for Pt electrocatalyst to achieve enhanced ORR performance compared to the electrocatalyst with untreated CO₂-derived carbon support?

3 Experimental

3.1 Pretreatment and N-doping of XC

Two chemical pretreatment solutions were used for pretreatment: 30% hydrogen peroxide (30% from Lach-Ner, s.r.o., the Czech Republic) and 65% nitric acid (65% from Sigma-Aldrich, Germany). To guarantee clean glassware, a three-neck round bottom flask was cleaned using the so-called Piranha solution prior to the pretreatment. After that, 0.5 grams of XC (from Fuel Cell Store, USA) were mixed with 500 milliliters of 5% HNO₃ and 10% H₂O₂, and the mixture was refluxed for eighteen hours at a temperature between 80 and 110 °C. The mixture was then allowed to cool to room temperature before being filtered through a polytetrafluoroethylene (PTFE) membrane and continuously rinsed with deionized water for 20 minutes. The final stage of the pre-treatment was drying the XC for 12 hours at 105 °C in an oven.

In case of N-doping, 8 g of dicyandiamide (DCDA) and 0.04 g of polyvinylpyrrolidone (PVP) powder were mixed with 0.4 g of XC. The mixture was placed in an Erlenmeyer flask and sonicated for 1.5 hours in an ultrasonic bath after ethanol was added. The mixture was then dried for approximately 80 minutes at 75 °C. Then, using a quartz boat, it was placed in an oven and purged with N₂ flow for 15 minutes. Last step was activation at 800 °C (heating rate of 10 °C per minute) for two hours under N₂ flow.

3.2 Synthesis of XC-supported electrocatalysts

pH of ethylene glycol (99.5%, Lach-Ner) was determined using a CyberScan PC 510 pH meter. By adding 0.4 ml of 1 M NaOH (98%, from Sigma Aldrich, Germany) to Ethylene glycol (EG), the pH level was tuned to 11. Next, 0.25 grams of pretreated or N-doped XC were added to 15 ml of pH-adjusted EG to be stirred for 1 hour under N₂ flow. To achieve a 20% Pt loading on XC (1:4 Pt to XC ratio), 131.25 mg of crystalline H₂PtCl₆ (99.9% metal basis, from Alfa Aesar, USA) was measured and diluted into 17 ml with deionized water. The diluted platinum precursor and EG-XC mix were refluxed for 3 hours at 115 °C with N₂ flow. Lastly, the refluxed mixture was stirred with N₂ flow overnight and washed with a continuous flow of deionized water and then with acetone for a very brief period. The sample was obtained after drying at 110 °C for 3 hours in an oven.

3.3 Synthesis of CO₂-derived carbon

Eutectic mixture of Li₂CO₃-Na₂CO₃-K₂CO₃ was made by mixing Li₂CO₃ (99%, from ACU PHARMA und CHEMIE), K₂CO₃ (99.3% p.a., Lach-Ner) and Na₂CO₃ (99% p.a., Lach-Ner) at a molar ratio of 43.5:31.5:25.0. The carbonate salt mixture was then moved into an alumina crucible, which was placed in a stainless-steel reactor. Once the mixture was melted at 450 °C, CO₂ capture began, and stainless-steel rods (SS304 from metall24.ee, Estonia) were inserted into the molten salt as both the cathode and anode. Potentiostatic electrolysis of CO₂ to generate carbon at the cathode was carried out by applying a voltage of 4 V to the electrodes, with the carbon materials collected from the cathode after deposition. The faradaic efficiency of carbon deposition was approximately 85%. Finally, the cathode was washed with 5 M HCl (Merck) to remove any solidified salt, and the produced carbon was dried.

3.4 Synthesis of CO₂-derived carbon supported electrocatalysts

Chloroplatinic acid hydrate (99.9% H₂PtCl₆ x H₂O, Aldrich) was employed as the platinum precursor for electrocatalyst synthesis. Initially, 0.2 ml of 1 M NaOH (98%, Aldrich) was added dropwise to 30 ml of ethylene glycol (99%, Lach-Ner) in a small beaker while stirring to tune the pH to 11. The pH-adjusted ethylene glycol was then poured to a three-neck round-bottom flask, followed by the addition of 0.2 g of CO₂-C, which was mixed for 90 minutes under a nitrogen atmosphere using a magnetic stirrer. Afterward, 0.105 g of the Pt precursor was diluted with 15 ml of deionized and added to the carbon-polyol mixture. The mixture was refluxed with a reflux apparatus and heated in an oil bath for 3 hours at 110–130 °C with N₂ flow. The mixture was then cooled and stirred overnight in nitrogen atmosphere. Finally, the electrocatalyst was washed with deionized water and dried in an oven at 70 °C for over 19 hours. A commercial Pt/C catalyst (19.8 wt.%, TKK) was used as a benchmark for comparison.

3.5 Pretreatment of CO₂-derived carbon

Before the pre-treatment, the synthesis flask was kept overnight in a concentrated mixture of HNO₃ (65%, Honeywell) and H₂SO₄ (96%, Lach-Ner), then thoroughly rinsed with deionized water (Milli-Q) to remove any potential impurities. The pre-treatment itself was carried out in two different aqueous solutions: a 10% H₂O₂ solution made from 30% H₂O₂ (Lach-Ner) and a 0.2 M KOH solution prepared from KOH flakes (92%, Lach-Ner). For the H₂O₂ treatment, 0.4 g of CO₂-C was dispersed in 400 ml of 10% H₂O₂, and in case of KOH treatment, 0.3 g of CO₂-C was dispersed in 300 ml of 0.2 M KOH. For 16 hours, both mixtures were refluxed at 110 °C, then washed using a continuous flow of deionized water through a nylon membrane filter (pore size 0.22 μm, Foxx Life Sciences). The pre-treated carbon materials were finally dried in an oven at 70 °C for 17 hours.

3.6 Synthesis of pretreated CO₂-derived carbon supported electrocatalysts

Compared to the initial study (II) where only CO₂-derived carbon supported electrocatalyst was prepared, pH of the ethylene glycol was adjusted to 12 in the next study (III) focused on pretreatment of CO₂-derived carbon as support material. Furthermore, the overnight stirring was performed in a flask covered with aluminum foil and the resulting electrocatalysts were also washed with acetone (99.5% from Aldrich) in addition to deionized water and dried in an oven at 70 °C for 17 hours. Apart from these, all other synthesis conditions and benchmark Pt/C used were same.

3.7 Electrochemical characterization

Electrochemical performance of electrocatalysts were evaluated by using rotating disk electrode (RDE) technique. The working electrodes were glassy carbon (Goodfellow Cambridge Ltd) with a geometric surface area of 0.2 cm² which were polished with 1 μm and 0.3 μm alumina slurries (Buehler) in a figure-eight pattern. The polished electrodes were sonicated in isopropyl alcohol (99.99% from Lachner) (I,II) or ethanol (99.5% from Berner) (III) for 5 mins followed by sonication in deionized water for another 5 mins. The electrocatalyst inks were prepared by dispersing 1 mg (I) or 4 mg (II, III) of electrocatalyst powder in 750 μl (I) or 4 ml of deionized water (II, III), followed by addition of 250 μl (I) or 50 μl (II, III) isopropyl alcohol (Lachner) and 0.405 μl (I) or 2 μl (II, III) of

5 wt. % Nafion solution (Aldrich). The ink was then sonicated for 1 hour (I) or 40 mins (II) or 30 mins (III) in cold water. It was further sonicated in ultrasonic homogenizer for 35 seconds (II). Finally, 30 μl (I) or 20 μl (II, III) of the ink was drop cast onto the polished glassy carbon electrode and dried in an oven (I), at room temperature (II) or in an incubator (III).

To prevent contamination and impurities, the electrochemical cell and its components were cleaned by soaking in a concentrated $\text{HNO}_3\text{:H}_2\text{SO}_4$ mix overnight, rinsed with deionized water and further soaked in KOH :isopropyl mix and boiled in deionized water (II) or just boiled in deionized water (III) to be rinsed again. The three-electrode RDE setup included reference electrode of saturated calomel electrode (I), silver/silver chloride electrode (SI analytics) (II) or HydroFlex reversible hydrogen electrode (Gaskatel) or (III) separated with a Luggin capillary. All reported potential values in this thesis are against reversible hydrogen electrode (RHE), unless stated otherwise. As a counter electrode, platinum wire (I) or graphite rod in a glass frit (II, III) were used.

After the electrochemical cell was filled with 0.5 M H_2SO_4 (98%, VWR) (I) or 0.1 M HClO_4 (Aldrich) (II, III) electrolyte solution and the electrodes were inserted, the solution was purged with N_2 flow (99.999%, Elme Messer) and the electrocatalyst surface was conditioned under N_2 atmosphere by applying 100 potential cycles between -0.2 V and 1.2 V (vs SCE) at 500 mV s^{-1} (I) or 200 potential cycles in the range of 0.05 V – 1.1 V (vs RHE) at 300 mV s^{-1} (II) or 50 potential cycles between 0.05 V and 1.1 V (vs RHE) at 200 mV s^{-1} with a potentiostat (Model 1010E, Gamry Instruments). Next, a cyclic voltammogram (CV) was recorded in the corresponding potential range and with N_2 atmosphere at 10 and 100 mV s^{-1} (I) or 50 mV s^{-1} (II) for estimation of electrochemically active surface area (EASA) via H-adsorption region or via CO stripping method (III) by saturating the solution with CO (98%, Elme Messer) for 1 min at a potential of 0.05 V (vs RHE), followed by N_2 purging for 10 mins to remove excess CO and lastly recording CV in the corresponding potential window at 20 mV s^{-1} . This was followed by taking another CV in N_2 atmosphere at 20 mV s^{-1} without (II) or with (III) rotation (1600 revolutions per minute, RPM) in the corresponding potential range to serve as the background current profile.

Next, the solution was saturated with O_2 (99.999%, Elme Messer) and ORR polarization curves were recorded in the corresponding potential range at 10 mV s^{-1} (I) or 20 mV s^{-1} (II, III) at rotation speeds ranging from 400 to 4400 RPM (I) or 400 to 3600 RPM (II, III) by controlling working electrode rotation with OrigaTrod apparatus (OrigaLys Electrochem SAS). The polarization curves were not background-corrected (I) or background-corrected (II) or both background and iR -corrected (III) by measuring the uncompensated resistance value with electrochemical impedance spectroscopy (EIS) at open circuit voltage (OCV) in the 10000 Hz – 10 Hz range with 10 mV amplitude. To characterize the aging of electrocatalysts, accelerated durability test (ADT) was performed by applying 500 (I) or 1000 (II, III) potential cycles between -0.2 V and 1.2 V (vs SCE) (I) or 0.6 V and 1 V (vs RHE) (II, III) in O_2 atmosphere at 500 mV s^{-1} (I) or 200 mV s^{-1} (II) or 100 mV s^{-1} (III) as well as recording ORR polarization curves (I, II) or both ORR polarization and CO stripping curves (III) before and after ADT.

The number of transferred electrons per O_2 molecule and kinetic current (for mass and specific activities) were derived by using the Koutecký–Levich (KL) equation [81]:

$$\frac{1}{j} = \frac{1}{j_k} + \frac{1}{j_d} = - \frac{1}{nFkc_{\text{O}_2}^b} - \frac{1}{0.62nFD_{\text{O}_2}^{\frac{2}{3}}v^{-\frac{1}{6}}\omega^{\frac{1}{2}}c_{\text{O}_2}^b} \quad (10)$$

Here j is the measured current density, j_k is the kinetic current density, j_d is the diffusion-limited current density, n is the overall number of electrons transferred per O_2 molecule, k is the electron transfer rate constant, F is the Faraday constant ($F = 96485 \text{ C mol}^{-1}$), D_{O_2} is the diffusion coefficient of oxygen ($1.93 \times 10^{-5} \text{ cm}^2 \text{ s}^{-1}$ in 0.1 M HClO_4 [82]), ν is the kinematic viscosity of the electrolyte ($1.009 \times 10^{-2} \text{ cm}^2 \text{ s}^{-1}$ in 0.1 M HClO_4), ω is the angular velocity of the rotating disk ($\omega = 2\pi N$, N is the linear rotating speed in rpm) and C_{O_2} is the bulk concentration of oxygen ($1.26 \times 10^{-3} \text{ mol L}^{-1}$ in 0.1 M HClO_4).

The Tafel slope (b) was calculated (II) by plotting the overpotential against the logarithm of the current density ($\log j$) for the polarization curve at 1600 rpm and fitting the linear part of the curve with the Tafel equation [81]:

$$\eta = a + b \log j \quad (11)$$

EASA (based on H-adsorption region) was calculated (I, II) by integrating the H-adsorption area of the CV to estimate the hydrogen adsorption charge ($Q_{H\text{-adsorption}}$) and plugging it into the equation below:

$$EASA_{Pt,cat} (m^2 g_{Pt}^{-1}) = \left[\frac{Q_{H\text{-adsorption}} (C)}{210 \mu\text{C cm}_{Pt}^{-2} L_{Pt} (mg_{Pt} \text{ cm}^{-2}) A_g (\text{cm}^2)} \right] 10^5 \quad (12)$$

Here, L_{Pt} is the Pt loading of working electrode and A_g is the geometric surface area of the glass carbon electrode. The charge associated with the full coverage of clean polycrystalline Pt with hydrogen monolayer was assumed to be $210 \mu\text{C cm}^{-2}$ [83]. In case of the EASA calculation with CO stripping (III), $Q_{CO\text{-oxidation}}$ was estimated by integrating the CO oxidation area instead and the charge required for CO monolayer formation on Pt surface was considered to be $420 \mu\text{C cm}^{-2}$ [84].

The mass and specific activities were calculated (III) by normalizing the kinetic current at 0.9 V vs RHE by the Pt loading on the electrode ($mg_{Pt\text{-disk}}^{-1}$) and Pt active surface area values ($\text{cm}_{Pt\text{-active}}^{-2}$), respectively. Onset potential (E_{onset}) was determined (III) by finding the potential at a current density of -0.1 mA cm^{-2} while the half-wave potential ($E_{1/2}$) was defined as the potential at half of the diffusion-limited current density in ORR polarization curves at 1600 rpm.

All of the potential values shown in the text are given versus RHE unless stated otherwise.

3.8 Physical characterization

The morphology of the samples were analyzed either by only scanning electron microscopy (SEM) (I) or by both SEM and scanning transmission electron microscopy (STEM) (II, III). To obtain SEM micrographs, Zeiss Ultra 55 with field emission gun (FEG) (I) or JEOL JSM-7500FA with a cold FEG at an acceleration voltage of 15 kV (II) or Thermo Scientific Quattro ESEM (III) was used. In case of the STEM, Spectra 300 (ThermoFisher) S/TEM at an acceleration voltage of 300 kV with high-angle annular dark field (HAADF) signal (II) or Thermo Scientific Talos 200X operated at 200 kV (III) was employed to acquire STEM micrographs. Energy-dispersive x-ray spectroscopy (EDS) was performed with JEOL JSM-7500FA (I) or with a SDD Ultim max 100 (Oxford) detector for SEM and on a Bruker Dual-X setup on the TF Spectra300 (II) or with Thermo Scientific Talos 200X (III). Micrographs were processed using ImageJ software for particle size estimation (II, III) [85]. The Fast Fourier Transform (FFT) was employed to obtain the spatial frequency data of the lattice fringes (III). After reducing noise in the FFT image and applying an Inverse

FFT (IFFT), the d-spacings were determined through line profile analysis. These calculated d-spacing values were subsequently matched against reference values for the relevant platinum planes, sourced from the Crystallography Open Database (COD: 1011113) [86].

X-ray diffraction (XRD) measurement was performed with Malvern PANalytical Xpert3 equipment by employing a Cu K α x-ray source ($\lambda = 0.154$ nm) and operating at the beam voltage and current values of 45 kV and 40 mA, respectively (I, II, III). Bragg's law was used to calculate the d-spacing (III).

Raman analysis was conducted with Horiba LabRam HR800 with a 532 nm laser line (I) or with Renishaw Invia Microscope using a 514.5 nm excitation source (II). The spectra were gathered using a 20x objective lens (with a numerical aperture of 0.4) and an estimated optical power density of several hundred kW cm⁻² at the sample surface (II). The data acquisition lasted for 30 seconds. In line with Ferrari et al.'s approach [87], the D-band was fitted using a Lorentzian function, while a Breit-Wigner-Fano (BWF) function was applied to the G-band. The peak height was employed to calculate the intensities in both instances. Background subtraction was performed with a cubic polynomial. The results presented represent the average of seven spectra.

The X-ray photoelectron spectroscopy (XPS) measurements were performed using a Kratos AXIS Supra X-ray photoelectron spectrometer, equipped with a monochromatic Al K α source (15 mA, 15 kV) to investigate the surface chemistry of the samples (III). XPS is capable of detecting all elements except hydrogen and helium, analyzes the surface to a depth of 7–10 nm, and has detection thresholds between 0.1–0.5 atomic % depending on the element. The instrument's work function was calibrated to produce a binding energy (BE) of 83.96 eV for the Au 4f_{7/2} peak of metallic gold, and the spectrometer's dispersion was adjusted to achieve a BE of 932.62 eV for the Cu 2p_{3/2} peak of metallic copper. A Kratos charge neutralizer system was applied to all the samples. Survey scans were conducted with a 300 μ m \times 700 μ m analysis area and a pass energy of 160 eV. High-resolution scans were done with the same analysis area but a pass energy of 20 eV. The spectra were charge-corrected by referencing the main line of the carbon 1s spectrum (adventitious carbon) set to 284.8 eV. The spectra were processed using CasaXPS software (version 2.3.23).

N₂ adsorption-desorption isotherms were acquired and studied by a NOVA 1200e instrument (Quantachrome) (II, III). Specific surface areas were calculated by Brunauer-Emmett-Teller (BET) method and porosity was estimated by quenched solid density functional theory (QSDFT). Mesopore-specific surface areas were found by subtracting t-plot-specific micropore surface area from total BET surface area as reported in another study [88].

The thermogravimetric analysis (TGA) was performed by heating the sample in an alumina crucible with Labsys 2000 (Setaram) thermoanalyser at a heating rate of 10 K min⁻¹ under air atmosphere (II) or with TGA/DSC3+ under air atmosphere, with a temperature range from 40 °C to 100 °C at a rate of 10 °C min⁻¹ (III).

4 Results and discussion

4.1 Electrochemical reduction of oxygen on platinum supported with pretreated Vulcan XC-72

Prior to synthesis and pretreatment of CO₂-C supported electrocatalysts, different pretreatment methods were evaluated by using Vulcan XC-72 (referred as XC) carbon black to determine a promising pretreatment solution that could be applied to CO₂-C. The protocols describing pretreatment of XC and XC-supported electrocatalyst synthesis have been discussed in sections 3.1 and 3.2. Electrochemical and physical characterization methods used for obtaining and analyzing the results are outlined in sections 3.7 and 3.8.

The electrochemically active surface area (EASA) for all electrocatalysts was determined from the cyclic voltammogram depicted in Figure 5 and summarized in Table 1. The electrocatalyst with H₂O₂-treated XC exhibited the highest EASA among the samples, being 46.3% greater than that of commercial Pt/C. While H₂O₂ treatment caused a significant increase in EASA, both HNO₃ treatment and nitrogen doping were observed to reduce the EASA of Vulcan carbon. The increased EASA in H₂O₂-treated Pt/XC-72R suggests enhanced utilization of Pt nanoparticles, likely due to oxygen-containing groups that help retain the nanoparticles on the surface during polyol synthesis.

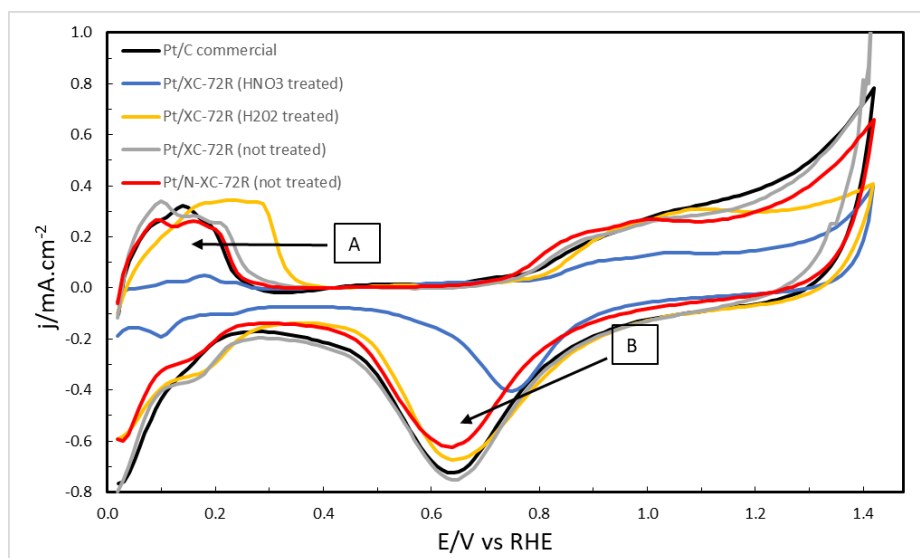


Figure 5. Comparison of cyclic voltammograms for all five samples recorded at 10 mVs⁻¹ under N₂ saturation (0.5 M H₂SO₄) at room temperature. A–hydrogen desorption region and B–oxide reduction peaks.

Table 1. EASA values for the electrocatalysts

	Pt/C (com.)	Pt/XC (HNO ₃ treated)	Pt/XC (H ₂ O ₂ treated)	Pt/XC (non-treated)	Pt/N-XC (non-treated)
EASA (m ² g ⁻¹)	77.83	13.16	113.88	83.65	65.70

ORR activity of the electrocatalysts was assessed by using a linear sweep voltammogram (LSV) generated at 1600 rpm for all samples, as shown in Figure 6. Identifying the onset potential for each sample is necessary for determining at what potential the reaction begins. The results revealed that the hydrogen peroxide and nitric acid-treated samples had superior onset potentials of 0.95 V vs RHE and 0.93 V vs RHE, respectively, compared to commercial Pt/C (0.89 V) and other electrocatalysts (N-doped XC – 0.90 V and untreated XC – 0.86 V). This demonstrates that the Pt/XC-72R material treated with hydrogen peroxide exhibited the highest electrocatalytic activity toward the ORR, which aligns well with its high electrochemically active surface area (EASA) value. Additionally, the diffusion-limited current density (j_d between 0.2 V and 0.7 V, according to the Levich equation) of this electrocatalyst reached approximately $-5.3 \text{ mA}\cdot\text{cm}^{-2}$, surpassing all other samples, further confirming its superior electrocatalytic activity. The sharp reduction wave observed for the hydrogen peroxide-treated material in the mixed kinetic-diffusion control region (0.2 V – 0.7 V) and its stable diffusion-limited current density plateau are also linked to its promising ORR characteristics. In contrast, the polarization curve for the HNO_3 -treated sample showed a slower reduction wave and lower diffusion-limited current density, indicating poorer ORR performance.

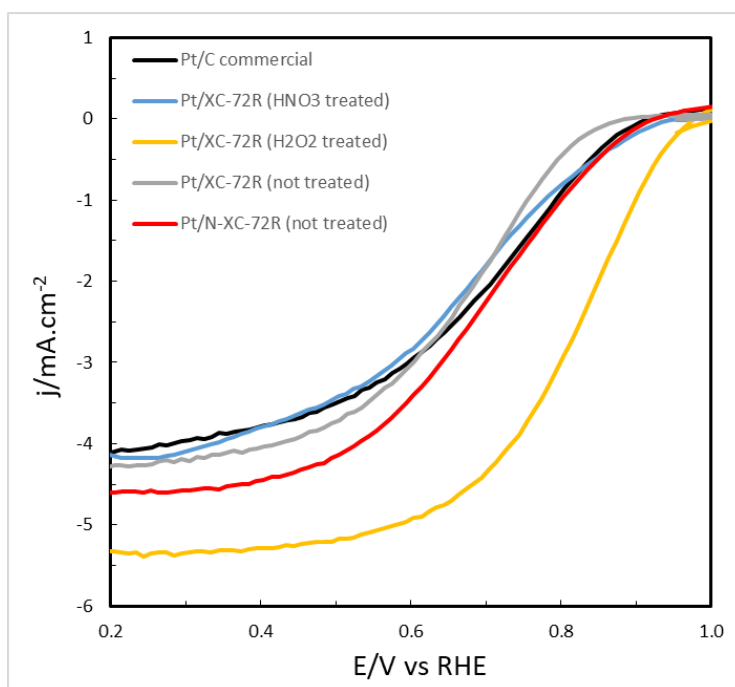


Figure 6. LSVs for all samples (recorded at 1600 rpm) at 10 mVs^{-1} under O_2 saturation in $0.5 \text{ M H}_2\text{SO}_4$.

On the contrary, there was only a slight variation between the onset potentials of Pt/N-XC-72R and the commercial Pt/C, leading to comparable electrocatalytic activity for the materials. The N-doped XC sample exhibited a slightly higher limiting current density than the commercial Pt/C, which is beneficial. However, for Pt with untreated XC support the onset potential was the lowest.

The improved performance of the H_2O_2 -treated sample is also evident in the oxide reduction peaks (Figure 5) from CV measurements recorded at 10 mV/s (with double-layer charging correction), where the peak current density is nearly as high as that of the commercial Pt/C. All the materials showed well-defined reduction peaks around 0.65 V vs RHE, except for the nitric acid-treated sample, which displayed a shifted and smaller peak at 0.76 V, likely due to slower oxide reduction kinetics. The Pt/N-XC-72R (non-treated) sample demonstrated consistent performance compared to commercial Pt/C in both CV and LSV measurements.

In summary, it is suggested that the type of pre-treatment performed can lead to varying degrees of enhanced activity, as reflected in the LSV plots of the electrocatalysts supported with nitric acid (moderate) and hydrogen peroxide (superior) treated support. Remarkably, the non-treated Pt/XC-72R also exhibited peak current density values similar to, and in some cases even slightly exceeding, the commercial sample, particularly in the oxide reduction peak (Figure 5). ORR polarization curves at different rotation rates for both the H_2O_2 -treated and non-treated materials are presented in Figure 7 as further comparison of electrocatalytic performance is necessary.

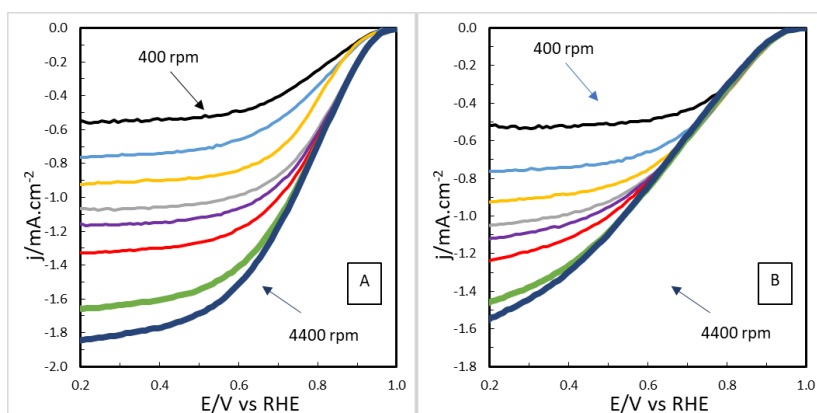


Figure 7. ORR polarization curves of A) Pt/XC-72R (H_2O_2 treated) and B) Pt/XC-72R (non-treated) samples under O_2 saturation obtained at different rotation speeds (in 0.5M H_2SO_4 at 10 mVs^{-1}).

Both graphs show a linear correlation between the diffusion-limited current and the rotation speed, though this is more apparent for the treated material. In this case, a flatter diffusion-controlled region is visible at all rotation levels, with a stable current, indicating improved performance. In contrast, the untreated sample exhibits overlapping curves that extend into the diffusion-controlled region, particularly at higher rotation speeds, and shows little to no stability in the limiting current at 4400 rpm. The slightly higher limiting current values and the well-defined plateau for the Pt/XC-72R catalyst (treated with H_2O_2) are likely due to the greater diffusion of oxygen molecules to the electrocatalyst surface, enhancing oxygen reduction properties [89]. These findings suggest that hydrogen peroxide pre-treatment of Vulcan carbon improves the electrocatalytic activity of the final electrocatalyst material in the oxygen reduction reaction (ORR).

Koutecky-Levich (KL) plots (see Figure 8) were used to analyze the electron transfer process for the electrocatalysts. The number of electrons transferred during ORR was approximately 4.4 for the H_2O_2 -treated sample at 0.6 V, which falls within the 10% deviation range commonly associated with the four-electron transfer pathway. The slight excess (~ 0.4) has also been noted in other studies [90]. While the untreated

sample showed slightly higher electron transfer values (around 5), the oxygen reduction can still be attributed to a similar four-electron pathway. Thus, both samples followed the four-electron mechanism for ORR, which is preferable to the two-electron pathway, as the latter leads to hydrogen peroxide (H_2O_2) formation, which is corrosive and reduces oxygen molecule utilization efficiency during direct reduction [91].

Moreover, both materials illustrate a linear relationship in their KL plots, indicating first-order kinetics for ORR with respect to oxygen concentration. However, the Pt/XC-72R (untreated) sample displays inconsistent and overlapping behavior, particularly at higher voltages. This irregularity could be due to experimental errors during the RDE testing or may reflect the intrinsic properties of the sample. To compare the KL analysis between the two samples, the y-intercept at 0.5 V vs. RHE (representing kinetic current density without mass transfer limitations) was visually obtained, and the results are presented in Table 2. It's worth noting that the other electrocatalyst materials also demonstrated a similar linear relationship between j^{-1} and $\omega^{-1/2}$. In Table 2 the calculated values for j_k , E_{onset} , mass activity (MA), and specific activity (SA) of electrocatalysts are compared.

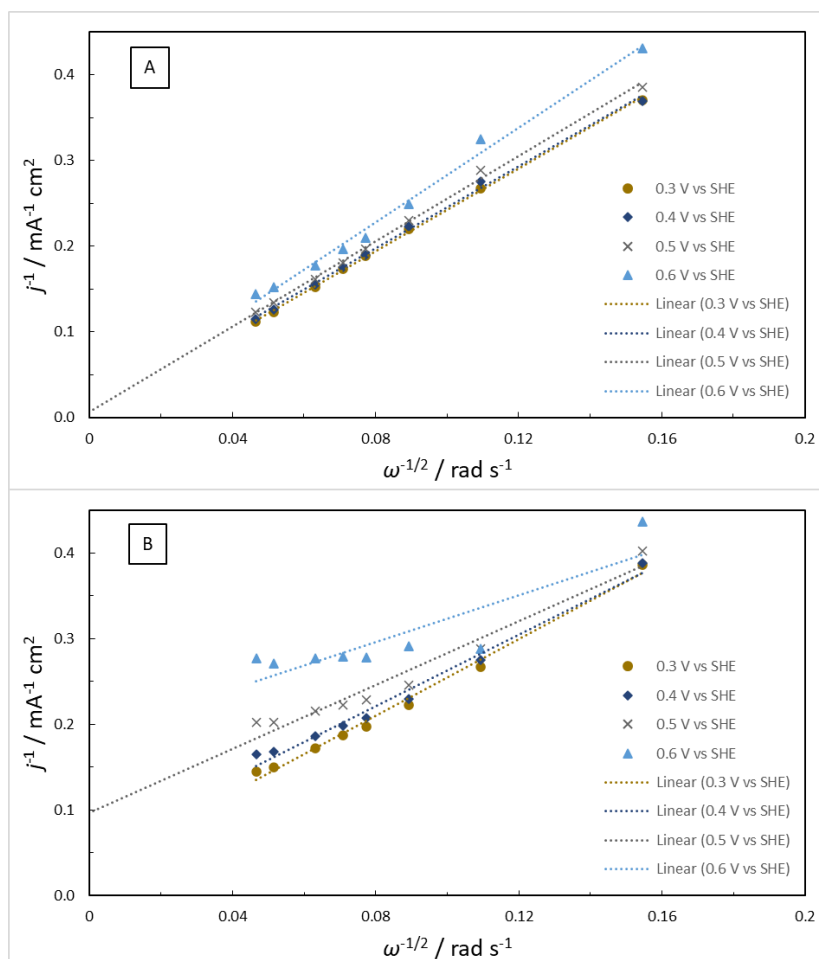


Figure 8. Koutecky–Levich plots of A) Pt/XC-72R (H_2O_2 treated) and B) Pt/XC-72R (non-treated) samples at different voltages and rotation rates.

Table 2. Kinetic current density, mass and specific activity values for all samples at 0.5 V.

	Pt/C (com.)	Pt/XC (HNO ₃ treated)	Pt/XC (H ₂ O ₂ treated)	Pt/XC (non-treated)	Pt/N-XC (non-treated)
j_k (mA cm ⁻²)	10	5	100	10	9
MA (A mg _{Pt} ⁻¹)	0.33	0.16	3.3	0.33	0.3
SA (μA cm ⁻²)	428.2	1265.8	2926.8	398.4	456.5
E_{ons} (V)	0.89	0.93	0.95	0.86	0.90

The findings indicate that the Pt/XC sample treated with H₂O₂ exhibits the highest kinetic current density at 0.5 V, which is ten times greater than that of the commercial Pt/C. In contrast, the material treated with HNO₃ showed the lowest value, only half that of the commercial Pt/C. Similarly, both the mass and specific activities of the H₂O₂-treated sample are higher than those of all other samples, demonstrating superior electrocatalytic performance, while the HNO₃-treated sample shows unexpectedly low values. This suggests that the type of pre-treatment selected significantly influences a material's ORR activity, and it can be concluded that the Pt/XC-72R catalyst treated with H₂O₂ outperformed the commercial Pt/C in nearly all aspects.

Given the promising and superior performance of the electrocatalyst treated with H₂O₂, its morphology was further investigated using SEM for detailed analysis, as shown in Figure 9.

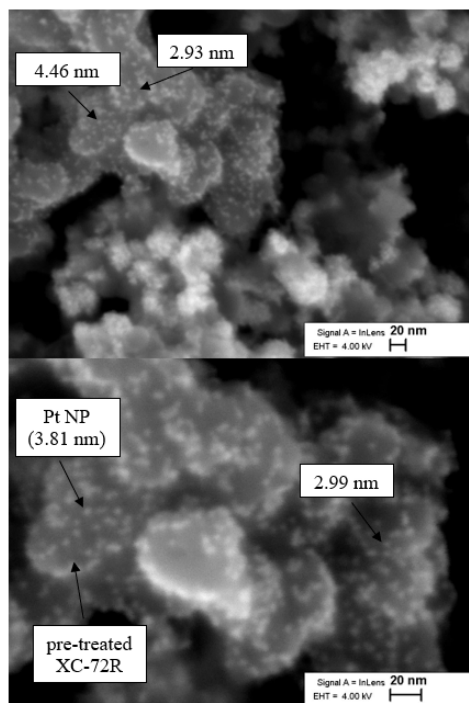


Figure 9. SEM micrographs of Pt/XC-72R (H₂O₂-treated).

The SEM microimages show that most Pt nanoparticles are evenly distributed across the XC-72R support. This uniform distribution is important for a highly efficient catalyst, as it enhances the electrochemically active surface area, thereby improving the catalyst's performance for the oxygen reduction reaction (ORR). Although some areas of agglomerated Pt are present, they make up a small part of the overall area.

In the SEM measurement also the size of the Pt nanoparticles was measured to be in a range between 2.9 nm and 4.4 nm. In a separate study, a Pt nanoparticle size of 4.4 nm was identified as optimal for achieving maximum mass activity towards ORR and high electrochemical stability [60]. While smaller particles are also present, most of the nanoparticles are found to be very close to the optimal value. This consistency aligns well with previous findings on the electrocatalytic activity of the H₂O₂-treated sample.

Furthermore, the EDS spectrum was obtained for both the general and Pt-rich areas of the electrocatalyst (see Tables 3 and 4). The spectrum from the general area confirms the presence of carbon and platinum, as well as the 1:4 stoichiometric ratio of Pt to C used in the synthesis. In the Pt-rich area, platinum's weight proportion exceeds that of carbon by approximately 53%.

Table 3. General EDS spectrum.

	Series	unn. C [wt. %]	norm. C [wt. %]	Atom. C [at. %]	Error [%]
Carbon	K-series	82.92	82.93	98.75	1.5
Platinum	M-series	17.07	17.07	1.25	0.7
Total		100	100	100	

Table 4. Pt-rich area of EDS spectrum.

	Series	unn. C [wt. %]	norm. C [wt. %]	Atom. C [at. %]	Error [%]
Carbon	K-series	23.59	23.70	83.46	3.5
Platinum	M-series	75.95	76.30	16.54	3.1
Total		99.53	100	100	

For deeper insights into the composition and crystal structure of the electrocatalysts, XRD patterns were obtained for all the samples (as illustrated in Figure 10). Additionally, the raw XC-72R material was also analyzed to identify its characteristic peaks and distinguish them from those of Pt crystallites.

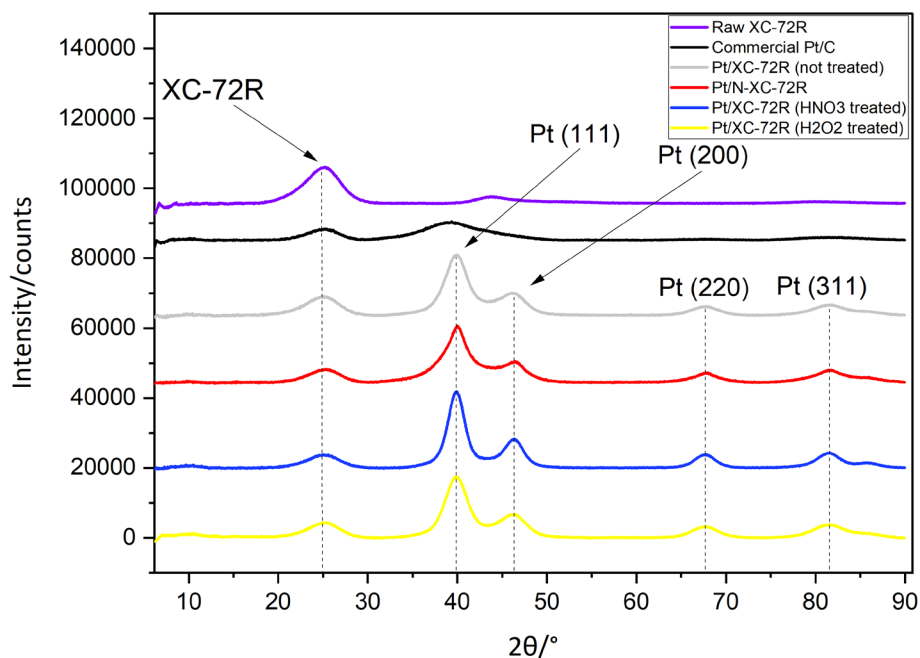


Figure 10. X-ray diffraction (XRD) patterns for all samples.

The crystallite size (in Table 5) calculated for the H₂O₂-treated Pt/XC-72R closely aligns with the measurement results from SEM analysis. Furthermore, the crystallite size of the pre-treated samples was found to be larger than that of the untreated sample, suggesting that the pre-treatment causes an increase in particle size. In this case, HNO₃ treatment could be used to produce larger particles, whereas H₂O₂ treatment might result in nanoparticles with moderate sizes. Interestingly, nitrogen doping of the untreated XC appears to produce crystallite sizes similar to those of the H₂O₂-treated electrocatalyst.

Table 5. Pt crystallite size for each sample (taken from the peak of Pt 111 plane).

	Commercial Pt/C	Pt/XC (HNO ₃ treated)	Pt/XC (H ₂ O ₂ treated)	Pt/XC (non-treated)	Pt/N-XC (non-treated)
Cr. Size	1.5 (nm)	5.0	3.9	3.6	4.0

Additionally, the results indicate that commercial Pt/C has the smallest Pt crystallite size, as evident from its peak near 40°. The XRD pattern of the commercial sample also lacked the smaller peak at 46°, which is likely due to the absence of the 200 plane in the crystal lattice and of XC-72R at 44°. However, small peaks at 67° and 81°, associated with the 220 and 311 planes, were observed, similar to the other samples.

Raman spectroscopy was conducted to investigate the structure of the carbon black in each sample, as shown in Figure 11.

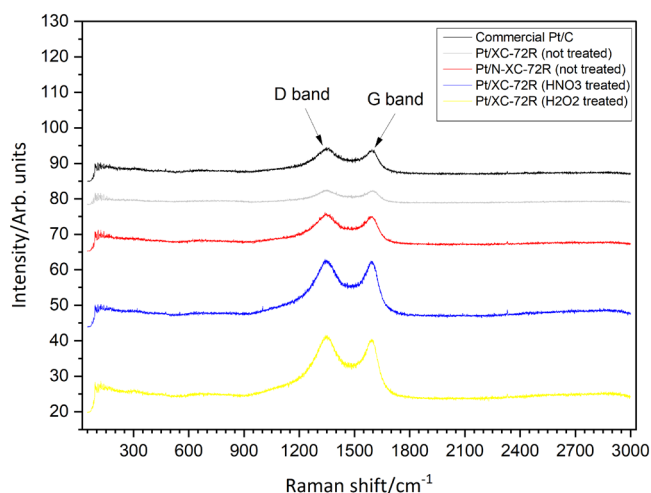


Figure 10. Raman spectra for all samples (532 nm laser line).

Three peaks, referred to as the D-band, G-band, and 2D (or G') band, are typically used to describe the Raman spectra of a material. In this study, only the first-order spectral range (1000 to 2000 cm^{-1}) is analyzed, focusing on the D and G bands, as illustrated in Figure 10. By identifying the Raman shift value of each peak, the structural properties of carbon nanomaterials can be understood. For instance, the D-band arises from the disorder at the edges of the microcrystalline structure and the G-band is associated with the presence of graphene [92].

In the spectra, the D and G bands appear around 1345 and 1595 cm^{-1} in all samples. A significant increase in the intensity of the D-band is noticeable for the pre-treated electrocatalysts, likely due to greater disorder in the XC-72R structure, which results from heat treatment and nitrogen doping in the case of the N-doped electrocatalyst. The commercial Pt/C catalyst exhibits slightly lower peak intensities compared to the other materials, which suggests a more ordered carbon black structure in this electrocatalyst. To compare the crystallinity and degree of disorder in the catalysts, the peak values obtained from the analysis are provided in Table 6, showing the Raman shifts corresponding to both the D and G bands.

Table 6. D and G-band values for all samples obtained from Raman spectra.

	Commercial Pt/C	Pt/XC (HNO ₃ treated)	Pt/XC (H ₂ O ₂ treated)	Pt/XC (non-treated)	Pt/N-XC (non-treated)
D band	1349.813 (cm^{-1})	1340.069	1342.611	1351.508	1340.493
G band	1594.693 (cm^{-1})	1590.033	1591.304	1598.930	1598.083
I_D	29.489 (arb. un.)	38.963	41.640	24.106	30.774
I_G	28.921 (arb. un.)	38.481	40.494	23.835	29.614
I_D/I_G	1.0196	1.0125	1.0283	1.0113	1.0391

The intensity ratio (I_D/I_G) is frequently used to assess the microstructure of different materials. For instance, the ratio for the H_2O_2 -treated sample is higher than for the untreated sample, likely due to reduced structural order and an increase in defects in the Pt/XC-72R (H_2O_2 -treated) electrocatalyst. The increase in defects in carbon black post-treatment is considered advantageous, as it indicates a more porous structure with more sites for platinum deposition, which in turn leads to improved Pt nanoparticle utilization, a higher electrochemically active surface area, and higher electrocatalytic activity.

On the other hand, the crystal structure of the nitric acid-treated catalyst seems slightly more ordered, similar to the untreated material, although its peak intensities are comparable to those of the H_2O_2 -treated sample. For the N-doped sample, the intensity ratio was the highest, and the peak intensities were similar to those of the commercial Pt/C catalyst, indicating a more ordered structure with fewer defects compared to the pre-treated materials. Therefore, the effect of nitrogen doping on XC-72R appears to be minimal in terms of altering carbon black's morphology.

In this study, Vulcan XC-72R carbon black was pretreated prior to the deposition of Pt nanoparticles and the effects of pretreatment on the electrochemical performance of the electrocatalysts were studied. Electrochemical tests showed that H_2O_2 -treated catalysts had the highest electrochemically active surface area (EASA), outperforming non-treated and commercial Pt/C catalysts, while HNO_3 -treated samples had lower EASA. H_2O_2 treatment improved oxygen reduction properties and kinetic activity. SEM and XRD analyses confirmed smaller Pt nanoparticle sizes for H_2O_2 -treated samples. Overall, it was found that H_2O_2 pretreatment enhanced catalytic performance for the oxygen reduction reaction (ORR). With this finding, the first objective of the PhD work was achieved and this was instrumental for the subsequent studies on CO_2 -derived carbon nanomaterials.

4.2 Electrochemical reduction of oxygen on platinum supported with CO_2 -derived carbon

The synthesis of CO_2 -derived carbon nanomaterial (CO_2 -C) and CO_2 -C supported electrocatalyst is described in sections 3.3 and 3.4. Figure 12 below depicts the steps taken for the synthesis. Detailed explanation about the electrochemical and physical characterization methods used are given in sections 3.7 and 3.8.

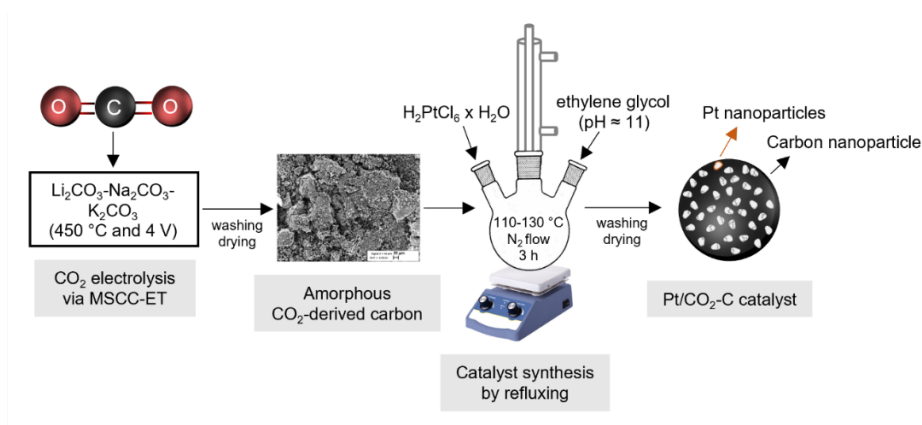


Figure 12. A schematic diagram of Pt/ CO_2 -C electrocatalyst synthesis steps.

To ensure an accurate comparison with the commercial Pt/C, EDS and TGA were conducted (Figure 13) to verify the platinum content in the electrocatalyst. Both analytical techniques indicated that the Pt/CO₂-C sample has approximately 17 wt.% Pt. The slight discrepancy from the intended 20 wt.% loading is likely due to impurities present in the sample and the incomplete reduction of the platinum salt during the synthesis process.

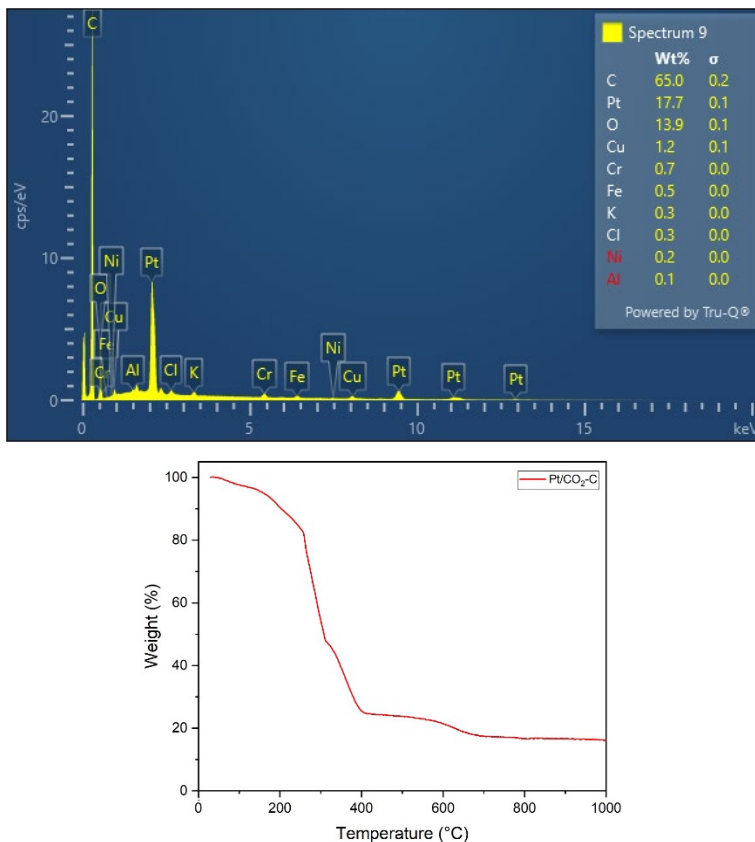


Figure 13. EDS (top) and TGA (bottom) plots for Pt/CO₂-C.

The SEM and STEM images (Figure 14) of Pt/CO₂-C reveal that Pt nanoparticles are evenly distributed across the CO₂-C support, and the morphology closely resembles that of the commercial Pt/C catalyst (Figure 15, top). In the case of raw CO₂-C, the SEM image (Figure 15, bottom) shows an amorphous structure with particles varying greatly in size. For Pt/CO₂-C, the average particle size of Pt nanoparticles on CO₂-C, as measured from the STEM images, was approximately 3.2 nm, which is similar to the particle size of the commercial sample (~3.4 nm).

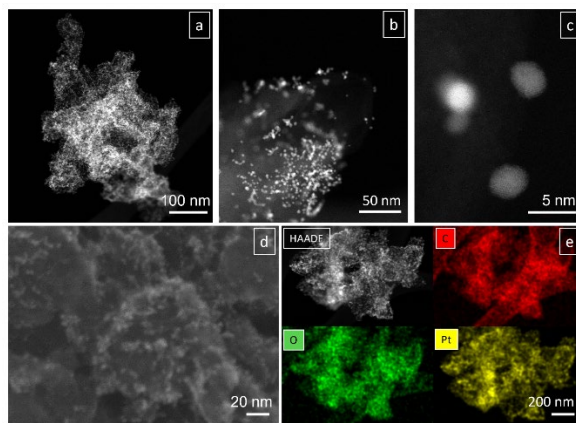


Figure 14. SEM and STEM microimages of Pt/CO₂-C. a-c HAADF-STEM images of the composite; d SEM image; e HAADF-STEM image with elemental maps (white-HAADF, red-C, green-O and yellow-Pt).

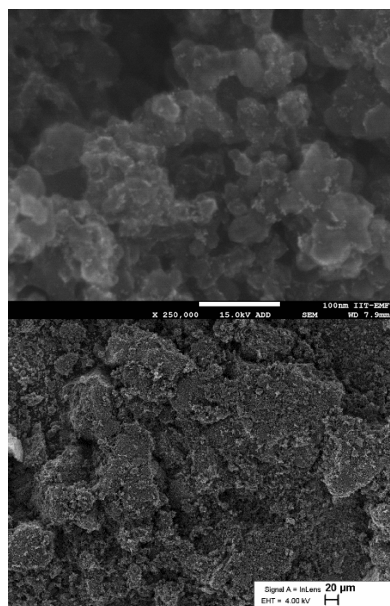


Figure 15. SEM image of commercial Pt/C (top) and raw CO₂-C (bottom).

Both materials display a narrow particle size distribution (Figure 16), indicating a uniform particle distribution. As discussed earlier, 4 nm has been suggested as the “sweet spot” for Pt nanoparticles for achieving optimal mass activity for ORR. As particle size for Pt/CO₂-C is very close to the value, this partially accounts for the higher mass activity of Pt/CO₂-C for ORR that is discussed next. It is important to note that, beyond the synthesis conditions, the choice of support also influences Pt nanoparticle size by controlling the degree of agglomeration of individual particles. Hence, CO₂-C emerges as a promising support material for adjusting the size of Pt nanoparticles.

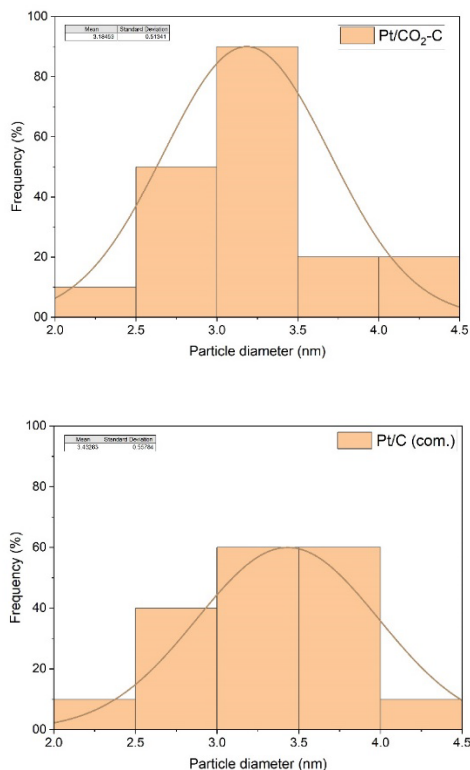


Figure 16. Particle size distribution histograms of Pt/CO₂-C (top) and commercial Pt/C (bottom).

XRD patterns for both samples are shown in Figure 17, alongside corresponding reference patterns. The primary difference between the observed patterns is due to the type of support material used during synthesis. For the Pt/CO₂-C sample, a distinct peak appears near a 2θ angle of 29.4° , which is associated with the chromite (Cr_2FeO_4) XRD pattern around 30° , originating from the stainless-steel electrodes employed in the CO₂-C synthesis. A smaller shoulder peak near 43° is also linked to the chromite pattern. Although literature does not provide specific information on the electrocatalytic properties of chromite, studies have shown that Cr and Fe transition metals can enhance catalytic activity toward ORR when combined with Pt [93]. However, it's important to note that the XRD and TGA results indicate the chromite content in Pt/CO₂-C is minimal, suggesting that Cr and Fe have a negligible impact on the electrocatalytic performance of Pt/CO₂-C. For both samples, the 2θ angles near 40° and 46° correspond to the Pt (111) and Pt (002) planes, respectively. In weakly adsorbing electrolytes, such as the HClO₄ solution used in this study, the Pt (111) facet has been shown to exhibit superior ORR activity compared to Pt (100) [94]. Consequently, the presence of Pt (111) facets in Pt/CO₂-C is considered advantageous.

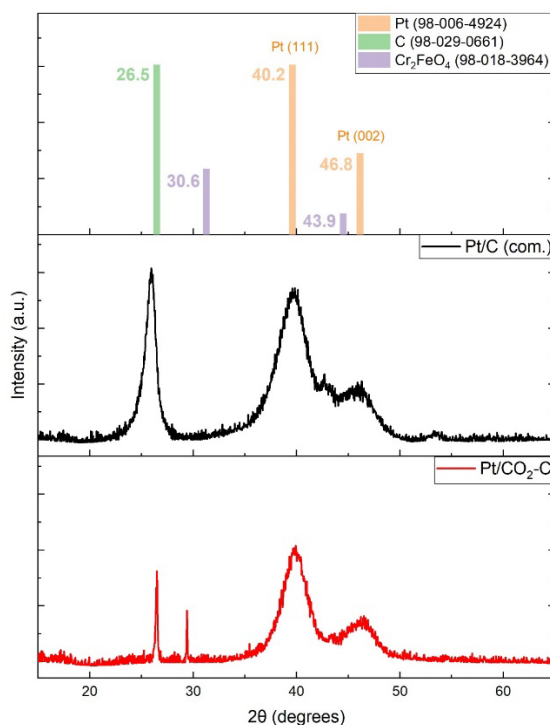


Figure 17. XRD patterns for commercial Pt/C and Pt/CO₂-C.

Raw CO₂-C, Pt/CO₂-C, and commercial Pt/C were also studied with Raman analysis. Typically for Raman spectra of carbon, 1000 cm⁻¹ to 2000 cm⁻¹ is the most important range as two distinct peaks of the D-band at approximately 1350 cm⁻¹ and the G-band at around 1600 cm⁻¹ are detected in this range. The D-band indicates structural disorder within the carbon, while the G-band results from in-plane vibrations of sp²-bonded carbon atoms [87]. Representative raw spectra and the cumulative fitted curves for each nanomaterial are displayed in Figure 18, indicating that the CO₂-C largely maintains its structure after platinum deposition. However, several notable differences arise when comparing the stock CO₂-C and Pt/CO₂-C. For example, both the I_D/I_G ratio and the full width at half maximum values in the spectra are reduced for Pt/CO₂-C (Table 7). These shifts suggest an increase in the graphitization of the carbon and a reduction in structural disorder after platinum deposition. A similar observation was reported by another research group studying carbon nanofibers coated with platinum nanoparticles [95]. It has been observed that platinum nanoparticles tend to attach primarily to defect sites or edges in unmodified carbons, which may clarify why the crystal structure of the carbon becomes more ordered after platinum loading—potentially explaining the narrower and sharper G-band seen in the Pt/CO₂-C [96]. Thus, the disordered structure of CO₂-C is considered advantageous for the uniform dispersion of platinum, enhancing electrocatalytic performance. In contrast, greater differences were noticed in the commercial sample. The I_D/I_G ratio in this sample is slightly higher than that of Pt/CO₂-C, but the FWHM values for the peaks are much smaller, indicating a more uniform structural distribution. Additionally, a prominent 2D band appears near 2700 cm⁻¹, resembling spectra of defective graphene [97].

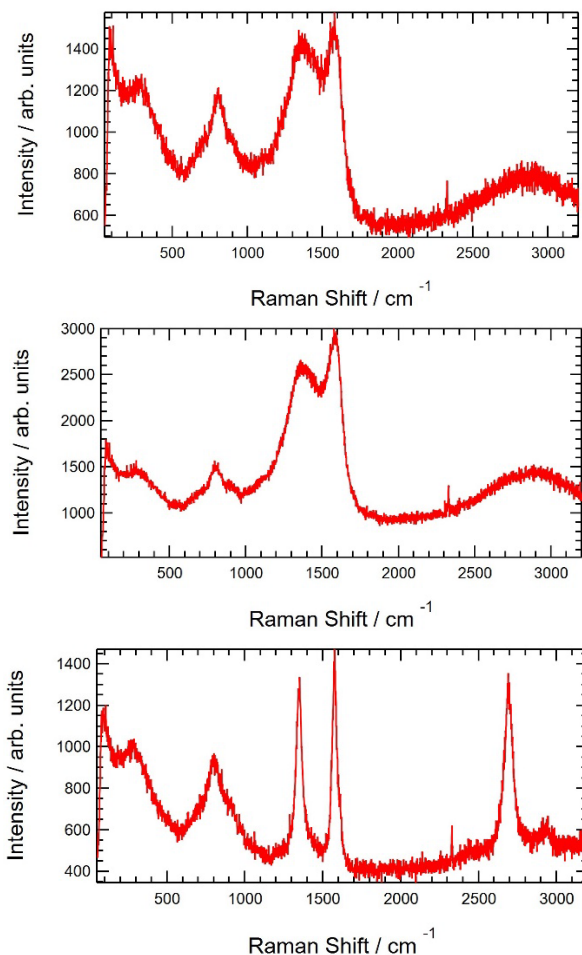


Figure 18. Raman spectra of raw CO₂-C (top), Pt/CO₂-C (middle) and commercial Pt/C (bottom).

Table 7. Raman characteristics of the studied nanomaterials.

Catalyst	I_D/I_G (arb. unit)	G_{FWHM} (cm ⁻¹)	D_{FWHM} (cm ⁻¹)
Raw CO ₂ -C	0.94 ± 0.04	117 ± 3	245 ± 11
Pt/CO ₂ -C	0.8 ± 0.1	112 ± 3	228 ± 30
Pt/C (com.)	0.9 ± 0.1	40 ± 2	51 ± 7

Ratio of the intensities of D and G peaks (I_D/I_G), full width at half-maximum for G (G_{FWHM}) and D peaks (D_{FWHM}). Uncertainties are taken as one standard deviation in all cases and multipeak fitting was performed to extract band parameters.

The textural properties of both samples were analyzed using N₂ physisorption, and the results are presented in Table 8 below. The BET and QSDFT (Quenched solid density functional theory) analyses indicate that the Pt/CO₂-C sample has a significantly larger surface area compared to the commercial sample. This increased surface area is beneficial because it allows for more active sites for the reaction, enhancing the overall

electrocatalytic performance. Additionally, the total pore volume of Pt/CO₂-C was marginally greater than that of Pt/C, while its average pore size was smaller than the commercial Pt/C. According to the pore size distribution charts (Figure 19), Pt/CO₂-C mainly contains mesopores, with a minor presence of micropores. In contrast, the commercial sample is predominantly mesoporous, with almost no detectable micropores. It has been suggested that a mesoporous carbon support structure is preferred for fuel cell electrocatalysts since mesopores promote better dispersion and utilization of metal particles, aiding the reaction [98]. In contrast, micropores could trap nanoparticles and limit access to reactants.

Table 7. Textural properties of electrocatalysts.

Catalyst	S_{BET} (m ² g ⁻¹)	S_{DFT} (m ² g ⁻¹)	V_p (cm ³ g ⁻¹)	d_p (nm)
Pt/CO ₂ -C	145.3	118.6	0.5	6.9
Pt/C (com.)	31.9	40.9	0.4	25.5

BET surface area (S_{BET}), specific surface area (S_{DFT}), total pore volume (V_p) and average pore diameter (d_p).

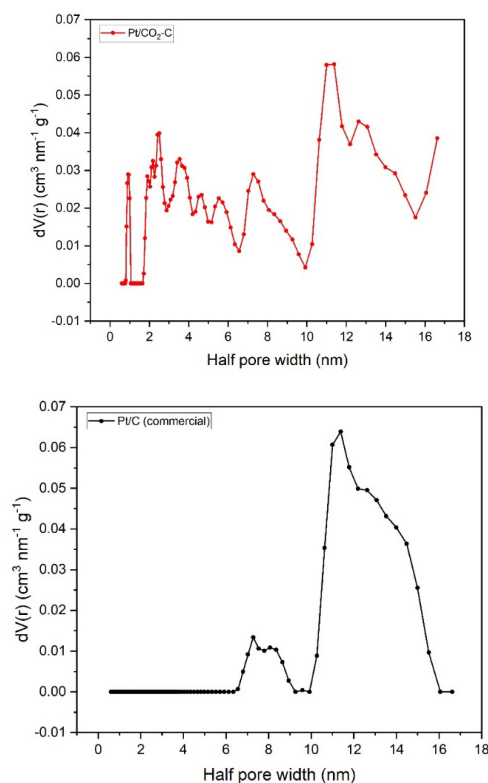


Figure 19. N₂ physisorption study results. Pore size distribution graphs of Pt/CO₂-C (top) and commercial Pt/C (bottom) calculated using the QSDFT.

The performance of the electrocatalysts in half-cell tests was evaluated using the RDE method and the oxygen reduction reaction (ORR) polarization curves recorded at 1600 rpm are displayed in Fig. 20a.

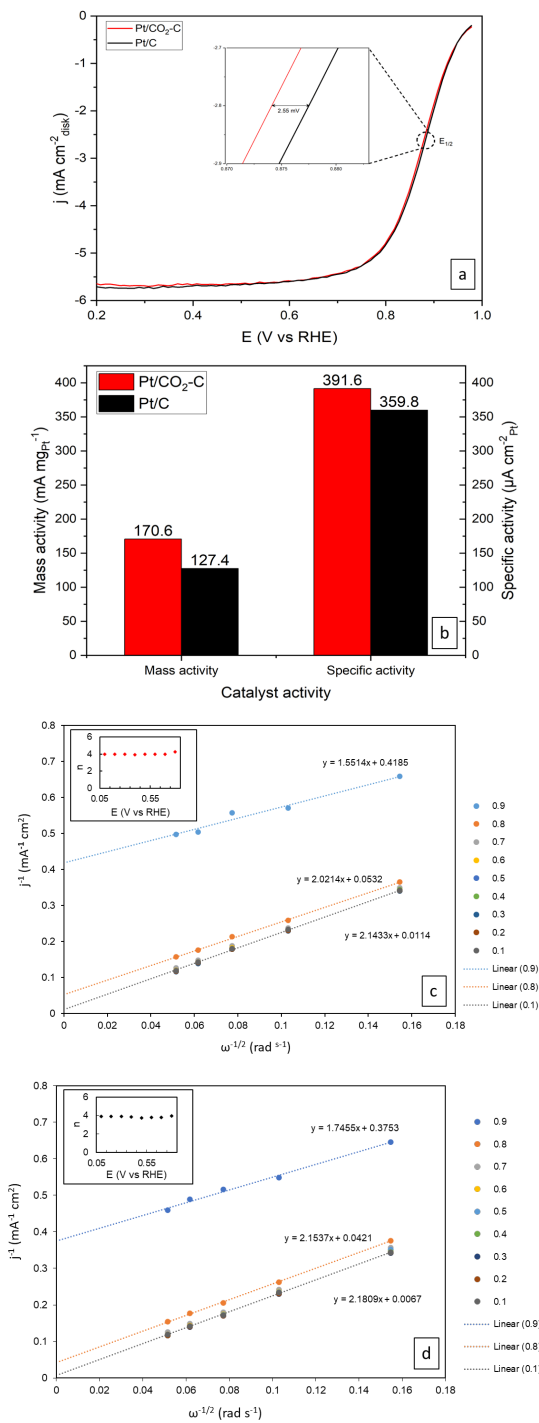


Figure 20. Electrochemical characterization results. **a** ORR polarization curves (anodic sweep) of Pt/CO₂-C and Pt/C (commercial) in O₂-saturated 0.1 M HClO₄ at 20 mV s⁻¹ with a rotation rate of 1600 rpm; **b** Comparison of mass and specific activities for both catalysts; Koutecký–Levich plots for **c** Pt/CO₂-C and **d** Pt/C commercial with the number of electrons transferred per O₂ molecule (n) in the insets.

Several key electrocatalytic performance metrics are summarized in Table 8. Based on the half-wave potential ($E_{1/2}$) and onset potential (E_{onset}), the electrocatalytic activity of Pt/CO₂-C is nearly equivalent to that of the commercial Pt/C. Notably, in terms of onset potential, Pt/CO₂-C demonstrates superior activity, with a positive shift of approximately 3.5 mV, reducing the overpotential for the ORR.

Table 8. Electrocatalytic performance metrics of the samples.

Catalyst	E_{onset} (V vs RHE)	$E_{1/2}$ (V vs RHE)	EASA (m ² gPt ⁻¹)	MA at 0.9 V vs RHE (mA mgPt ⁻¹)	SA at 0.9 V vs RHE (μ A cm ⁻² Pt)
Pt/CO ₂ -C	0.990	0.873	43.56	170.6	391.6
Pt/C (com.)	0.987	0.876	35.41	127.4	359.8

Additionally, the mass and specific activity of Pt/CO₂-C are approximately 33% and 9% higher, respectively, than those of commercial Pt/C, as shown in Fig. 20b. This suggests that, despite the commercial electrocatalyst's slightly higher Pt loading, Pt/CO₂-C exhibits a larger electrochemically active surface area (EASA), allowing more Pt nanoparticles (per mg and cm² of the electrocatalyst) to participate in the reaction. This improved Pt utilization contributes to enhanced reaction kinetics. This finding aligns with the previously discussed relationship between nanoparticle size and the electrocatalyst's maximum mass activity.

In addition to polarization curves, Koutecký–Levich and Tafel plots are employed to determine the number of electrons involved in the oxygen reduction reaction and to identify the reaction's rate-determining step. The analysis of the K–L plots (Fig. 20c, d) derived from polarization curves at different rotation rates (Figure 21) indicates that ORR proceeds predominantly through the 4-electron pathway for both catalysts, a mechanism commonly associated with polycrystalline platinum surfaces [99] and considered to be advantageous over the 2-electron pathway as discussed earlier.

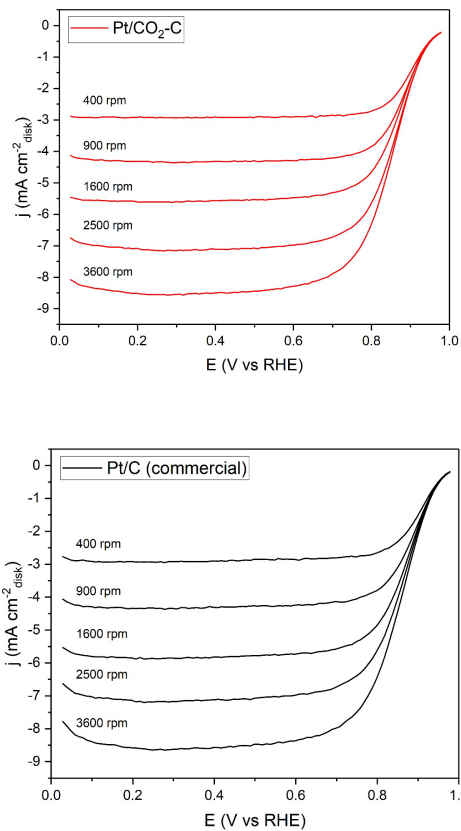


Figure 21. ORR polarization curves (anodic sweep) of Pt/CO₂-C and Pt/C (commercial) in O₂-saturated 0.1 M HClO₄ at 20 mV s⁻¹ with different rotation rates.

For Tafel plots, a widely studied Pt/C catalyst is reported in the literature to exhibit slopes of approximately 60 mV dec⁻¹ at low overpotentials and 120 mV dec⁻¹ at high overpotentials under acidic conditions. The deviations observed in this study (Fig. 22) can be attributed to various factors, including the specific exposed facets of Pt crystals [100], the purity of the electrolyte, and the selected range for linear curve fitting [101].

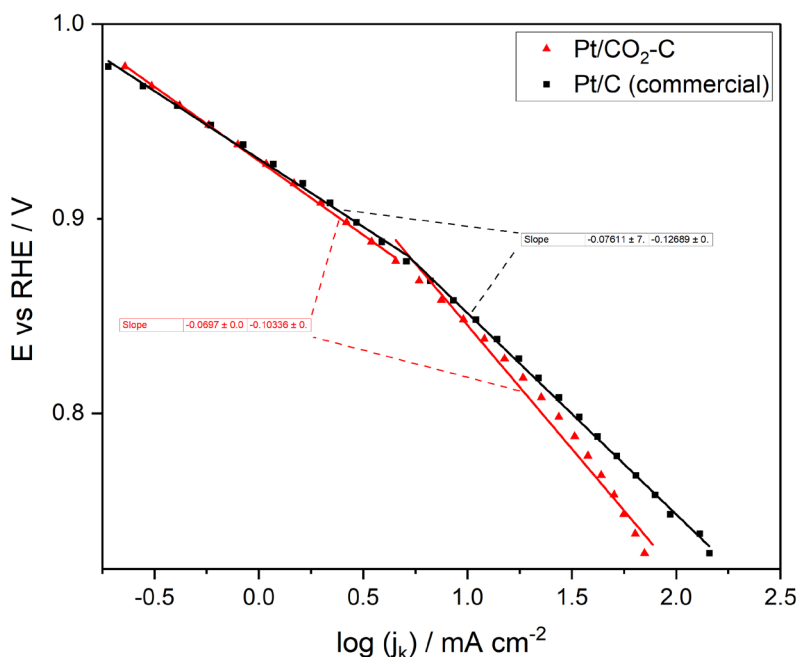


Figure 22. Tafel plots of Pt/CO₂-C and Pt/C (com.) at 1600 rpm with corresponding linear fits and calculated Tafel slope values.

At low overpotentials (greater than 0.88 V versus RHE), both Pt/CO₂-C and commercial Pt/C exhibit slopes close to 70 mV dec⁻¹, aligning with findings by Marković et al., which attribute this value to the Pt (111) crystal facet in 0.1 M HClO₄ [102]. The removal of OH* species has been proposed as the rate-limiting step for this region [99], [103]. At higher overpotentials (less than 0.88 V versus RHE), the slopes increase to approximately 105 mV dec⁻¹ for Pt/CO₂-C and 130 mV dec⁻¹ for the commercial Pt/C. These values closely resemble those associated with the Pt (110) crystal facet reported in the same study, approaching the 120 mV dec⁻¹ value that indicates the initial electron transfer to O₂ as the rate-limiting step [104]. The lower slope observed for Pt/CO₂-C at higher overpotentials suggests a superior electrocatalytic activity compared to the commercial Pt/C. However, it should be noted that there is ongoing debate regarding the accurate determination of the rate-limiting step in the oxygen reduction reaction (ORR) on Pt and its agreement with the actual reaction kinetics [100], [101], [105].

To evaluate the durability of the electrocatalysts, an accelerated durability test involving 1000 potential cycles was conducted within a voltage range of 0.6 V to 1 V versus RHE. Following the test (as shown in Fig. 23), the half-wave potential of Pt/CO₂-C showed a negative shift of approximately 2.8 mV, compared to a shift of about 3.9 mV for the commercial Pt/C benchmark. Additionally, the mass activities at 0.9 V vs RHE decreased by 5% for Pt/CO₂-C and by 12% for the commercial Pt/C. These findings indicate that Pt/CO₂-C exhibits enhanced durability under the tested conditions. It is worth noting that the support material plays a crucial role in determining the overall durability of the electrocatalyst [98] which further demonstrates that CO₂-C is a suitable support material for enhancing electrocatalyst durability.

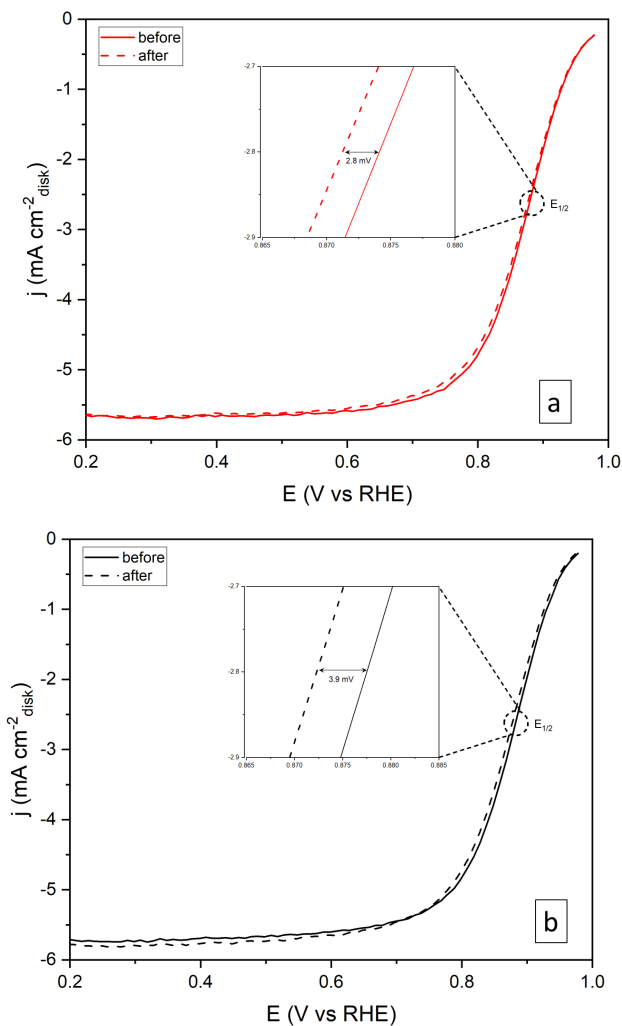


Figure 23. Accelerated durability test results. ORR polarization curves (anodic sweep) of **a** Pt/CO₂-C and **b** Pt/C (commercial) in O₂-saturated 0.1 M HClO₄ at 20 mV s⁻¹ taken before and after 1000 potential cycles between 0.6 V and 1 V vs RHE at 200 mV s⁻¹.

In this study, carbon nanomaterial was derived from CO₂ via the MSCC-ET technique and used as support material for the Pt electrocatalyst. The prepared electrocatalyst demonstrated a higher surface area than commercial Pt/C and superior electrochemical activity, including higher onset potential, mass and specific activity, and better durability. These improvements were attributed to the interaction between the CO₂-derived carbon support and Pt nanoparticles, showcasing the potential of this sustainable material for fuel cell applications. As planned in the second objective of the work, this study proved the possibility of replacing commercial carbon black support of Pt electrocatalyst with CO₂-derived carbon and revealed the promising ORR performance of the Pt electrocatalyst supported with CO₂-derived carbon.

4.3 Electrochemical reduction of oxygen on platinum supported with pretreated CO₂-derived carbon

The pretreatment of CO₂-derived carbon (CO₂-C) and the synthesis of pretreated CO₂-C supported electrocatalyst are described in sections 3.5 and 3.6. Detailed explanation about the electrochemical and physical characterization methods used are given in sections 3.7 and 3.8.

The platinum loading in each electrocatalyst was determined through thermogravimetric analysis. Based on the TGA results (Figure 24), it was established that the commercial Pt/C sample contains 20 wt % Pt, while the Pt loadings for Pt/CO₂-C, Pt/H₂O₂-CO₂-C, and Pt/KOH-CO₂-C are 35 wt %, 31 wt %, and 30 wt %, respectively.

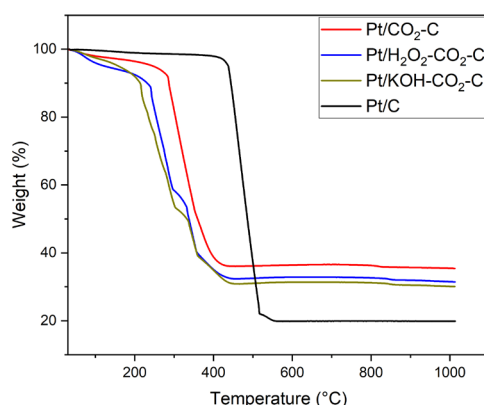


Figure 24. Thermogravimetric analysis results for all samples.

STEM and TEM images (Figure 25) of the electrocatalyst samples were examined to assess the physical characteristics. Regarding the uniform distribution of Pt nanoparticles on the carbon support, the Pt/KOH-CO₂-C sample exhibited the most homogeneous distribution, followed by Pt/H₂O₂-CO₂-C, commercial Pt/C, and Pt/CO₂-C, in that order. Although the CO₂-C-supported samples showed overall homogeneous nanoparticle distribution, STEM images revealed that their uniformity was lower compared to commercial Pt/C. Further analysis identified localized areas of nanoparticle agglomeration in the synthesized samples, which is attributed to their higher Pt loading compared to the commercial Pt/C electrocatalyst.

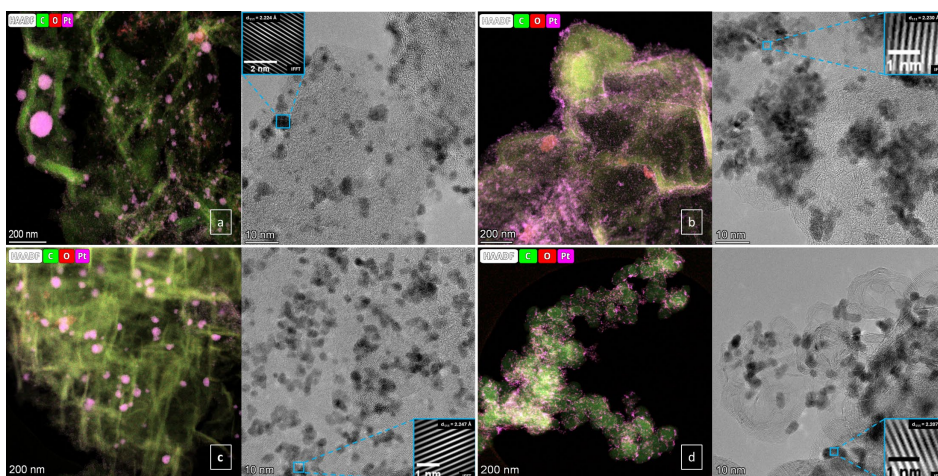


Figure 25. HAADF-STEM (with elemental mapping) and TEM images of (a) Pt/CO₂-C, (b) Pt/H₂O₂-CO₂-C, (c) Pt/KOH-CO₂-C and (d) commercial Pt/C samples. The insets with HR-TEM images show the IFFT of the region designated with the blue box.

The particle size distribution of the electrocatalysts were analyzed based on the plotted histograms (Figure 26). The histograms indicate that the Pt nanoparticles on the H₂O₂-CO₂-C support range in size from 2 to 10 nm, with a mean particle size of approximately 5.7 nm. Compared to other samples, this distribution is broader, as also confirmed by STEM micrographs. The Pt/KOH-CO₂-C and commercial Pt/C samples exhibit similar mean particle sizes, but the smallest Pt nanoparticles were observed in the Pt/CO₂-C electrocatalysts. Compared with the previous study, increasing the pH of the ethylene glycol solution resulted in even smaller nanoparticles (2.96 nm compared to 3.18 nm). High-resolution transmission electron microscopy (HR-TEM) images of all samples revealed regions with visible lattice fringes (Figure 25, insets). These regions were analyzed to estimate d-spacing values, all of which were approximately 2.2 Å, consistent with the (111) plane of Pt ($d_{111} = 2.263$ Å) [86].

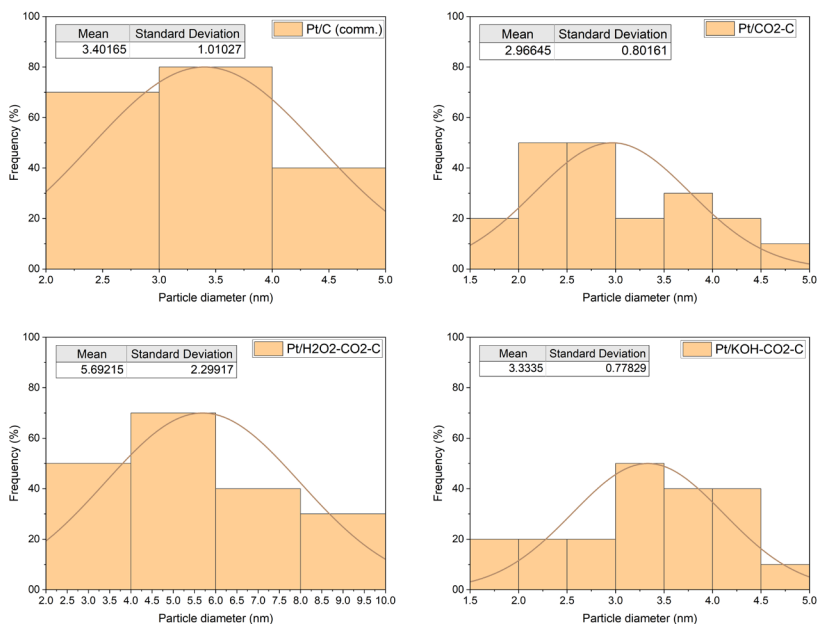


Figure 26. Particle size distribution histograms of all samples.

The nitrogen physisorption analysis was used to estimate the BET and mesopore-specific surface areas (Figure 27) of the electrocatalysts. The findings reveal structural changes in the sample porosity due to various pre-treatment methods. Using Pt/CO₂ as a reference, it was noted that both KOH and H₂O₂ pre-treatments of the carbon support created additional mesopores and increased the BET surface area. This is attributed to the corrosive behaviour of KOH and the oxidative effect of H₂O₂, which combine adjacent micropores to form mesopores, as explained by Kumar et al [79].

Compared to Pt/CO₂-C, the KOH treatment led to a modest increase in mesopore-specific surface area (from 22.74 to 23.88 m² g⁻¹). In contrast, H₂O₂ pre-treatment resulted in a large enhancement from 22.74 to 48.5 m² g⁻¹ with a total BET surface area increase of 33.49 m² g⁻¹. However, merging micropores can be detrimental, as they may promote Pt nanoparticle aggregation within these spaces. This behaviour was observed in STEM micrographs, particularly for Pt/H₂O₂-CO₂-C (Figure 25b).

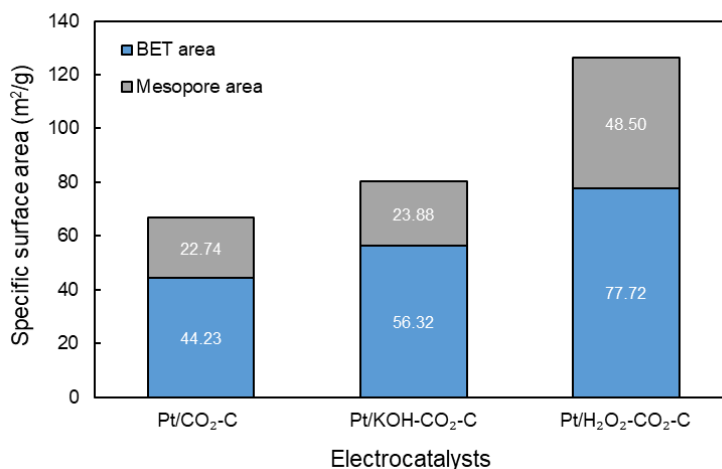


Figure 27. BET and mesopore-specific surface areas of the electrocatalysts synthesized in this study from the N₂ physisorption study.

As illustrated in Figure 28, the examination of X-ray diffraction (XRD) patterns indicates that Pt (111) and Pt (002) reflections at 2-theta angles of 40.2° and 46.8° are the dominant platinum planes for all analyzed samples, with these peaks being more prominent in the samples synthesized in this study. The broader Pt (111) and Pt (311) peaks, along with the lower intensity of the Pt (200) peak in the commercial sample, imply that the CO₂-C supported electrocatalysts possess more crystalline Pt nanoparticles compared to the commercial Pt/C electrocatalyst.

Additionally, the sharp peak at 26.1°, corresponding to the C (002) plane in the commercial Pt/C sample, indicates a graphitic carbon support structure. In contrast, the broader peaks at 25.6° observed in the other samples are indicative of a more disordered carbon structure. This disordered carbon characteristic in CO₂-C supported samples offers potential advantages since the Pt (111) plane has been linked to enhanced oxygen reduction reaction activity in weakly adsorbing electrolytes compared to the Pt (100) plane [106]. Furthermore, defect-rich carbon structures are considered favourable sites for Pt nanoparticle attachment [78]. These observations support the idea that modifying the carbon support structure can indirectly improve ORR performance.

To validate these findings, d-spacing values for all samples were calculated from the Pt (111) XRD peaks and compared with values derived from high-resolution transmission electron microscopy microimages. As shown in Table 9, the d-spacing measurements from the XRD data align with those obtained from the HR-TEM images.

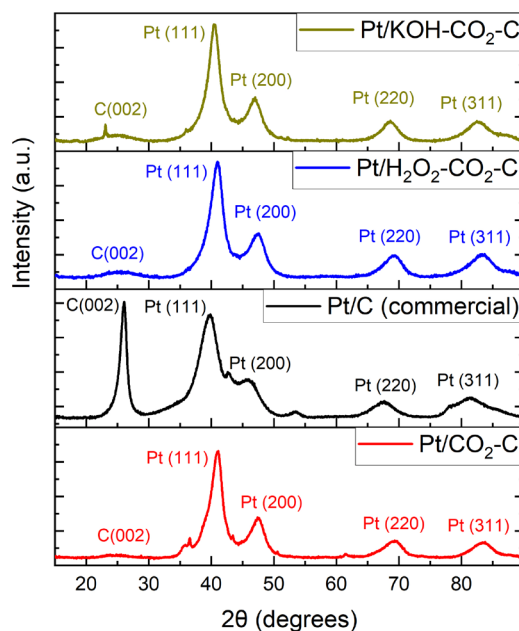


Figure 28. X-ray diffraction patterns of all samples.

Table 9. Comparison of d -spacing values obtained from HR-TEM images and XRD patterns.

Electrocatalyst	d_{111} from HR-TEM (Å)	d_{111} from XRD (Å)
Pt/CO ₂ -C	2.22	2.20
Pt/KOH-CO ₂ -C	2.24	2.23
Pt/H ₂ O ₂ -CO ₂ -C	2.23	2.22
Pt/C	2.20	2.25

Figure 29 illustrates the XPS spectrum focusing on the Pt 4f_{7/2} and Pt 4f_{5/2} regions for the electrocatalysts analyzed in this study. Previous research indicates that an increase in the binding energy of Pt 4f core levels in XPS analysis is associated with electronic interactions between platinum and its carbon support [107]. Depending on the electronic characteristics of the support material, charge transfer occurs between the platinum nanoparticles and the support in order to equalize their respective Fermi levels [107]. For all the electrocatalysts synthesized here, the Pt 4f_{7/2} peak appears at higher binding energies compared to commercial Pt/C, with the most significant positive shift observed in the Pt/KOH-CO₂-C sample, followed by Pt/H₂O₂-CO₂-C and then Pt/CO₂-C. These positive shifts result from the electron-withdrawing nature of the carbon support, which induces electron transfer from platinum to carbon, thereby altering the d-band structure of the electrocatalyst. This process reduces the adsorption energy of oxygen-containing species, enhancing oxygen reduction reaction activity and durability due to improved interactions between the metal and the support [107], [108], [109]. Consequently, from the perspective of metal-support interactions, pretreating CO₂-C with KOH and H₂O₂ solutions offers advantages, suggesting better ORR performance for platinum nanocatalysts supported with these pretreated materials.

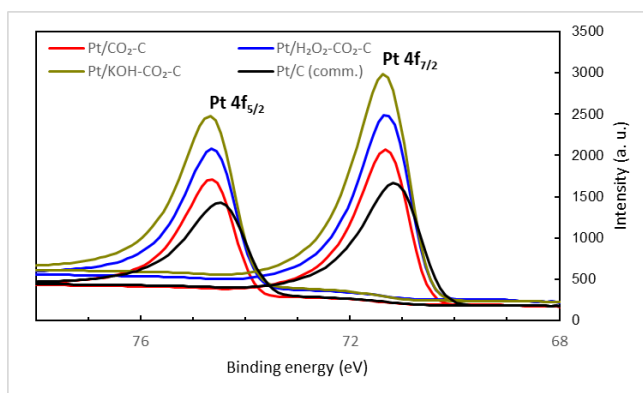


Figure 29. XPS spectrum of Pt 4f_{7/2} and Pt 4f_{5/2} regions for all samples.

In addition to influencing the metal–support interaction, the goal of pretreatment was to add oxygen–containing functional groups to the carbon support’s surface as well. This process can be assessed by analyzing the elemental composition on the carbon surface using XPS data, as detailed in Table 10. The table indicates that the oxygen content on the surface of the CO₂–C–supported electrocatalysts exceeds that of commercial Pt/C, indicating effective functionalization. Regarding oxygen atomic percentages, the data revealed the following trend, indicating that peroxide pretreatment is the most effective method for introducing oxygen groups: Pt/H₂O₂–CO₂–C > Pt/KOH–CO₂–C > Pt/CO₂–C > Pt/C.

Table 10. Surface atomic concentrations of all samples determined from the XPS spectrum.

Sample	C (at.%)	O (at.%)	Pt (at.%)	Cu (at.%)
Pt/CO ₂ –C	84.8	9.9	1.9	3.4
Pt/H ₂ O ₂ –CO ₂ –C	82.5	13.4	1.7	2.4
Pt/KOH–CO ₂ –C	82.5	12.5	2.6	2.4
Pt/C (comm.)	92.4	6.4	1.2	n/a

To determine the types of oxygen–containing groups, the relative areas for each group were obtained by deconvoluting the C 1s peaks from the XPS analysis, as shown in Table 11. The findings indicate that hydroxyl and ether groups predominate in all samples, followed by carbonyl and ester groups in CO₂–C–supported electrocatalysts. Compared to Pt/CO₂–C, the Pt/H₂O₂–CO₂–C and Pt/KOH–CO₂–C samples showed an increased presence of all oxygen–containing groups, confirming the introduction of these groups through functionalization. Peroxide pretreatment generated slightly higher amounts of C–OH, C–O–C, and C=O species compared to KOH pretreatment, whereas KOH treatment resulted in a somewhat greater concentration of O–C=O species. Several studies have shown that oxygen functionalization of carbon supports enhances electrocatalytic activity for the oxygen reduction reaction by disrupting the sp² carbon network and facilitating charge delocalization due to oxygen’s high electronegativity, which improves the adsorption of ORR intermediates [110], [111], [112]. Additionally, certain oxygen functional groups have been associated with increased durability in carbon–supported Pt electrocatalysts [113]. Therefore, the XPS results agree with these previous findings and suggest improved ORR performance for the pretreated samples.

Table 11. Assignments, positions and relative area of C 1s peaks of all samples determined from the XPS spectrum (binding energies at the bottom).

Sample	C-OH, C-O-C (%)	C=O (%)	O-C=O (%)
Pt/CO ₂ -C	10.3	5.4	4
Pt/H ₂ O ₂ -CO ₂ -C	11.6	6.6	5.1
Pt/KOH-CO ₂ -C	11.3	6.2	5.5
Pt/C (comm.)	10.2	1.4	4.3
Binding energy (eV)	286.3	287.7	288.9

To evaluate the electrochemical characteristics of the synthesized samples, ORR polarization curves at various rotation speeds were recorded (see Figure 30). Using the ORR polarization curve measured at 1600 rpm (Figure 31), key parameters for comparing the electrocatalytic performance of the samples were summarized in Table 12.

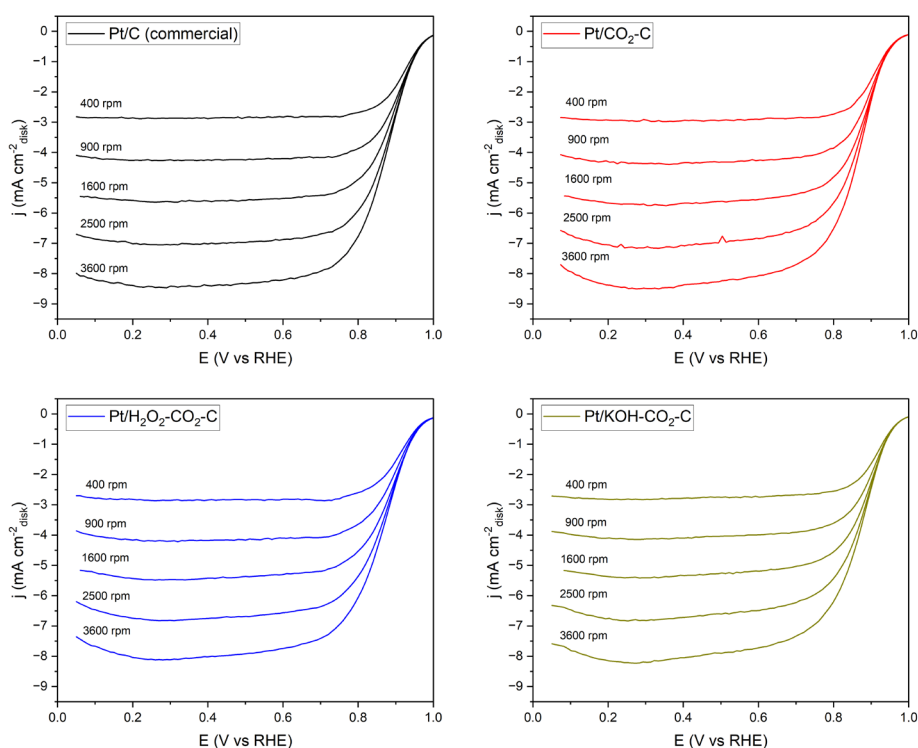


Figure 30. ORR polarization curves (anodic sweep) of all samples in O₂-saturated 0.1 M HClO₄ at 20 mV s⁻¹ with different rotation rates.

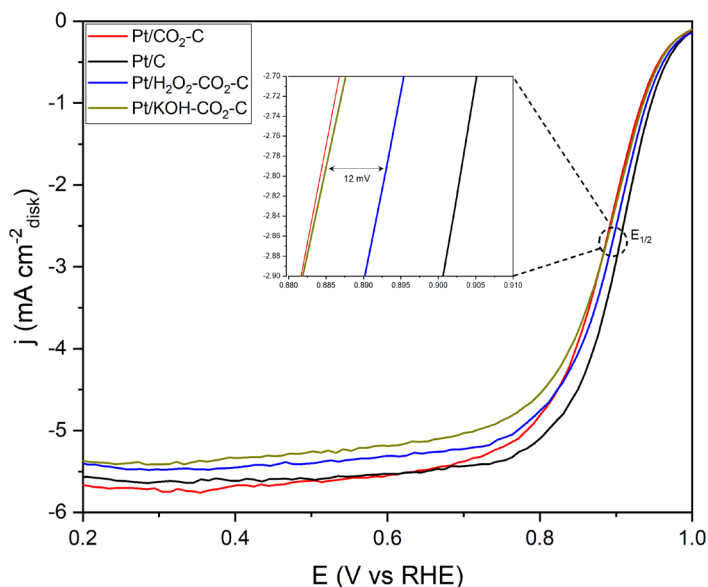


Figure 31. ORR polarization curves (anodic sweep) of all samples in O_2 -saturated 0.1 M $HClO_4$ at 20 mV s^{-1} with a rotation rate of 1600 rpm.

Table 12. Electrocatalytic activity metrics for all samples.

Sample	EASA _{CO-st} ripping ($\text{m}^2 \text{g}_{\text{Pt}}^{-1}$)	MA at 0.9 V vs RHE ($\text{mA mg}_{\text{Pt}}^{-1}$)	SA at 0.9 V vs RHE ($\mu\text{A cm}^{-2}_{\text{Pt}}$)	E_{onset} (V vs RHE)	$E_{1/2}$ (V vs RHE)
Pt/CO ₂ -C	13.4	102.0	759.9	1.0	0.88
Pt/H ₂ O ₂ -CO ₂ -C	13.2	142.8	1076.4	1.01	0.89
Pt/KOH-CO ₂ -C	8.7	131.1	1503.8	0.99	0.88
Pt/C	52.7	287.7	545.8	1.0	0.90

EASA of the samples was determined using CO stripping curves (Figure 32). The current peaks observed in the curves correspond to the oxidation potential of adsorbed CO (CO^{ads}), while the peak areas provide a measure of the density of active sites for CO^{ads} oxidation [114]. Considering that open facets and defect sites in Pt-based nanocatalysts are more reactive toward CO^{ads} oxidation than compact facets, the A peak (indicating higher adsorption energy) and the A* peak (indicating lower adsorption energy) in the CO stripping curves are associated with compact and open facets, respectively, in Pt/C electrocatalysts [115]. Using the same methodology, CO_2 -C supported samples (B peak) demonstrate a lower activation barrier for CO^{ads} oxidation. However, compared to the commercial sample, the CO_2 -C supported samples show significantly smaller peak areas, indicating fewer active sites for CO^{ads} .

Furthermore, the EASA values of all CO_2 -C supported samples (ranging between 8.7 and $13.4 \text{ m}^2 \text{g}_{\text{Pt}}^{-1}$) are considerably lower than that of the commercial Pt/C sample ($52.7 \text{ m}^2 \text{g}_{\text{Pt}}^{-1}$). This reduction is attributed to the agglomeration of Pt nanoparticles, as observed in STEM micrographs. This agglomeration prevents CO from adsorbing onto Pt atoms located within the core of these clusters, reducing the charge related to CO oxidation on the Pt surface.

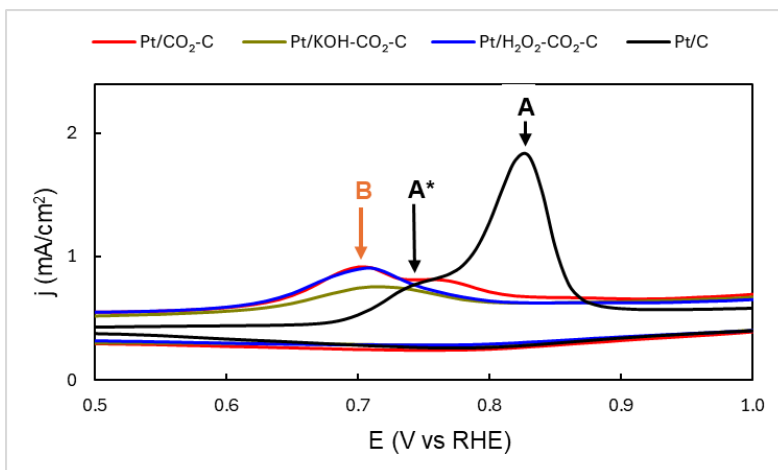


Figure 32. CO stripping curves of all samples in N_2 -saturated 0.1 M $HClO_4$ at 20 mV s^{-1} .

The disparity between the calculated mass activities of commercial Pt/C and CO_2 -C-supported electrocatalysts is relatively minor. When comparing the mass activities and specific activities of samples using pretreated support versus untreated support, a notable enhancement in both metrics is observed for pretreated CO_2 -C. Among the samples, Pt/ H_2O_2 - CO_2 -C demonstrates significantly higher MA than both Pt/ CO_2 -C and Pt/ KOH - CO_2 -C. However, Pt/ KOH - CO_2 -C shows the greatest SA, even surpassing the values calculated for commercial Pt/C. This is an expected outcome as Pt sites with low coordination (such as edge sites, defects, and steps) have a lower specific activity, while high-coordination Pt sites (such as terraces) exhibit higher specific activity. Larger particles expose a greater proportion of terrace sites relative to steps or edges due to their geometric properties, resulting in elevated SA values across all CO_2 -C-supported electrocatalysts [57].

The cyclic voltammograms for all samples are illustrated in Figure 33. A typical CV reveals three distinct regions significant for electrochemical analysis: the hydrogen underpotential deposition (HUPD) region, representing hydrogen adsorption and desorption (highlighted in yellow); the double-layer region (depicted as a clear area); and the oxygen region, reflecting OH^- adsorption and oxide formation/reduction (occurring above 0.6 V vs. RHE). The peaks labelled A1/A1* and A2/A2* on the curves correspond to H^+ desorption and adsorption from the compact (111) and open (200) crystal facets, respectively. Meanwhile, the E_0^{ads} and E_0^{des} peaks indicate the adsorption and desorption of oxygen species on the Pt surface.

Compared to commercial Pt/C, the CO_2 -C-supported samples exhibit broader peaks in the HUPD region, suggesting a stronger affinity for H^+ adsorption and desorption. However, the E_0^{des} peaks for all samples are nearly identical, implying similar energy barriers for oxygen desorption. This observation aligns with previous findings showing that the onset potentials for the oxygen reduction reaction (ORR) across all electrocatalysts are nearly the same. Additionally, the CO_2 -C-supported samples display a thicker double-layer region, indicating greater hydroxide formation compared to the commercial Pt/C electrocatalyst. Another notable feature is the less intense E_0^{ads} peaks of the CO_2 -C-supported samples, occurring at a lower potential. This observation is consistent with XPS characterization results and suggests weakened adsorption energy for oxygen-containing species.

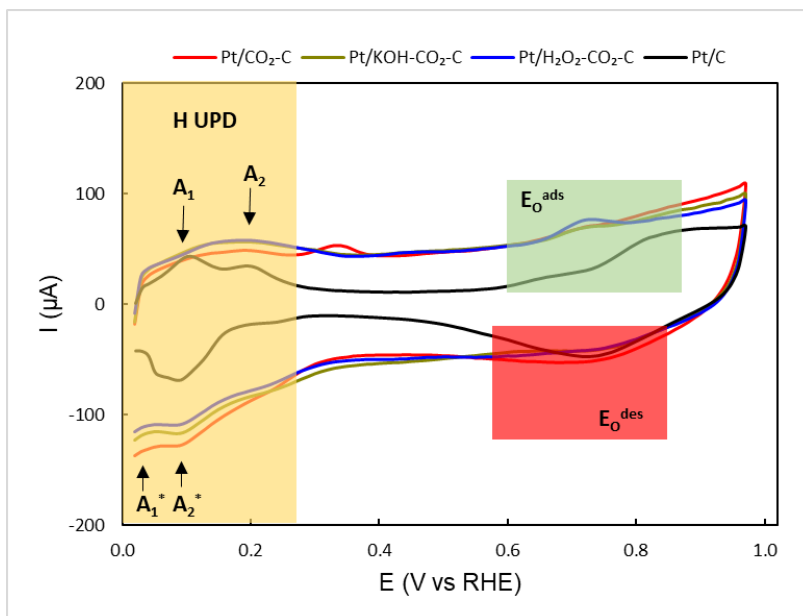


Figure 33. Cyclic voltammetry curves of all samples in N_2 -saturated 0.1 M HClO_4 at 50 mV s^{-1} .

The number of electrons involved in the reaction, can be determined from Koutecký–Levich plots generated from the polarization curves of the oxygen reduction reaction at varying rotation rates. Based on the K–L plots (Figure 34), all electrocatalysts exhibited a four–electron ORR pathway in the diffusion–limited current region. This pathway is preferred for fuel cell applications because it enhances fuel cell efficiency and avoids the formation of harmful hydrogen peroxide, which can deteriorate the electrocatalyst [116].

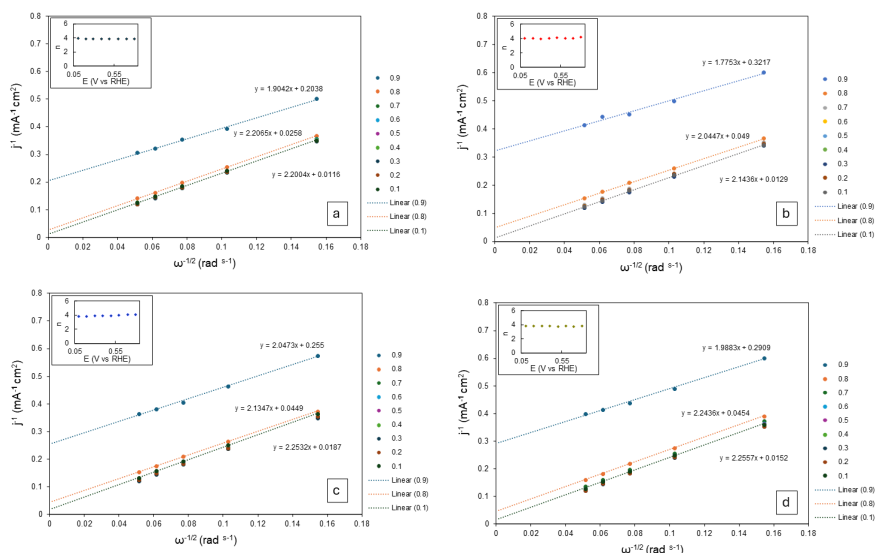


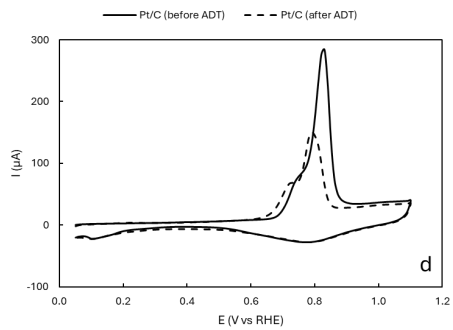
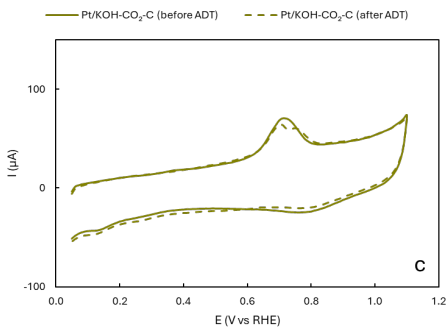
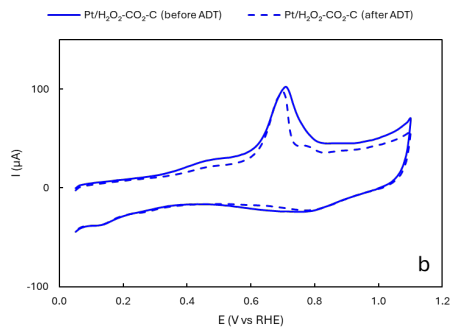
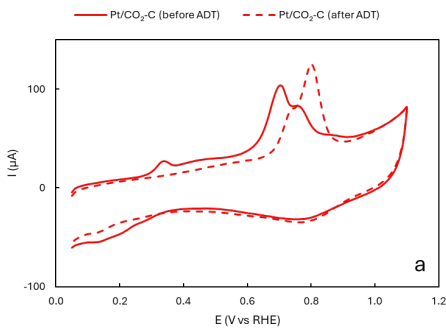
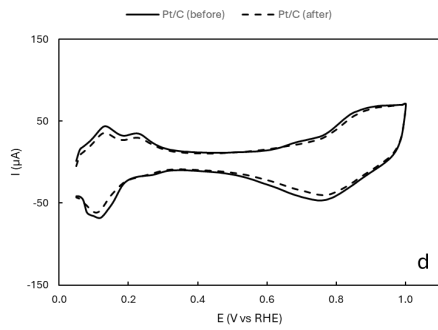
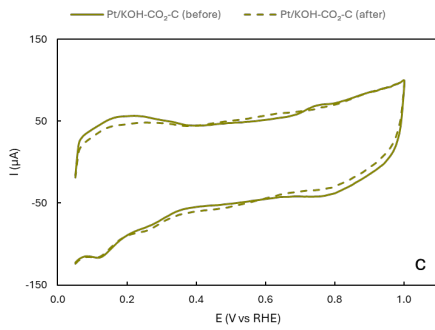
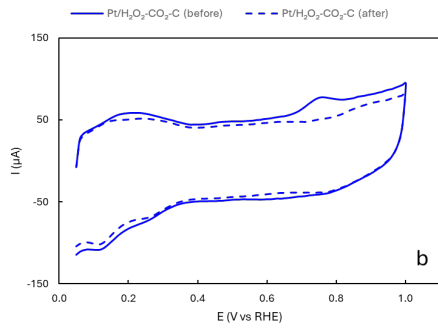
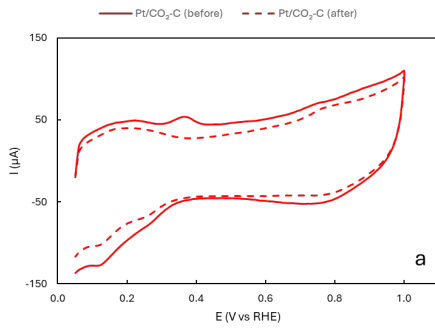
Figure 34. Koutecký–Levich plots for (a) commercial Pt/C, (b) Pt/CO₂-C (c) Pt/H₂O₂-CO₂-C and (d) Pt/KOH-CO₂-C with the number of electrons transferred per O₂ molecule (n) in the insets.

The durability of the catalysts was assessed through an accelerated durability test involving 1000 potential cycles between 0.6 and 1 V versus the reversible hydrogen electrode (RHE). The impact of the ADT was evaluated using CO stripping measurements conducted before and after cycling (Figure 35, top right) to estimate the electrochemically active surface area loss for each catalyst. Among the catalysts, the commercial Pt/C showed the greatest EASA loss (38.8%), followed by Pt/KOH-CO₂-C (20%), Pt/H₂O₂-CO₂-C (19.6%), and Pt/CO₂-C (4.5%).

Pt supported on untreated CO₂-C demonstrated the highest durability under reaction conditions, showing the least loss of EASA. However, electrocatalysts with pretreated supports also exhibited notable durability, surpassing that of the commercial Pt/C. This difference is attributed to the agglomeration of Pt nanoparticles during the pretreatment process, which increases the susceptibility of the EASA to long-term degradation. Nevertheless, the enhanced durability of the H₂O₂-CO₂-C and KOH-CO₂-C supported electrocatalysts compared to the commercial Pt/C can be explained by improved metal-support interactions and the presence of specific oxygen-containing functional groups, as previously discussed in the XPS analysis.

A comparison of CVs and ORR polarization curves (Figure 35, top left and bottom, respectively) before and after accelerated durability testing offers additional understanding of the samples' performance during the test. For the CVs, a decrease in the intensity of the platinum oxidation peak near 0.8V versus the reversible hydrogen electrode, related to the formation and adsorption of OH_{ads}, was observed for the synthesized samples. This reduction is likely due to residual CO on the platinum surface, which remained after the CO stripping process and inhibited OH_{ads} adsorption. Additionally, for all samples, including commercial Pt/C, the hydrogen adsorption and desorption peaks in the hydrogen underpotential deposition region became less distinct after ADT, consistent with a decrease in EASA, as discussed earlier. Regarding the ORR polarization curves, only minor changes were observed for all samples. A slight decrease in diffusion-limited current density was detected for Pt/CO₂-C and Pt/KOH-CO₂-C, while it remained constant for Pt/H₂O₂-CO₂-C and commercial Pt/C. Despite these variations, the ORR performance of all samples remained stable after ADT, demonstrating good durability under laboratory-scale durability testing conditions.

To conclude, the results of this study fulfilled the final objective of the work as the pretreatment of CO₂-derived carbon support resulted in enhanced ORR performance for the Pt electrocatalyst which was found to be superior compared to the sample with untreated CO₂-C support.



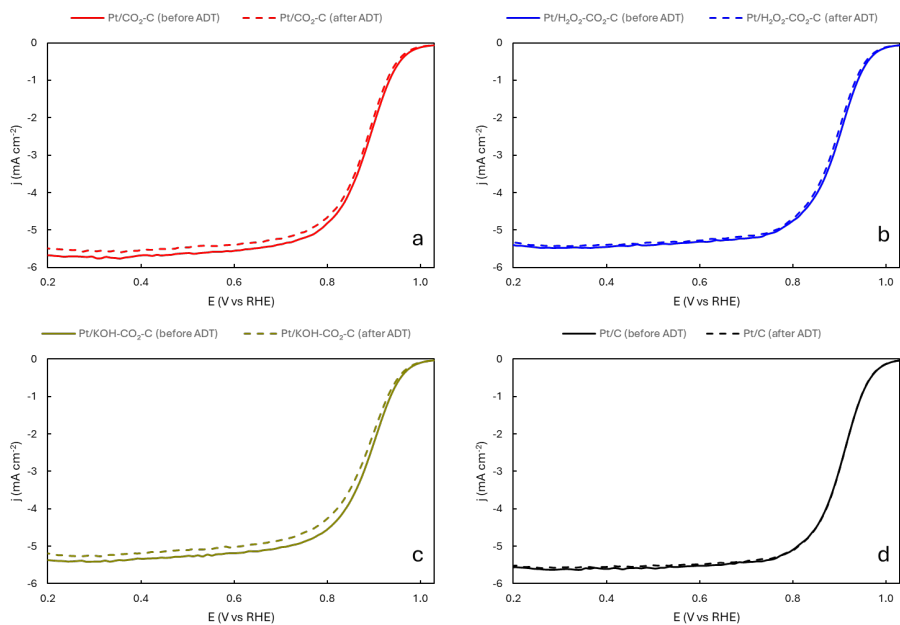


Figure 35. Top: Cyclic voltammety curves (before and after ADT) of (a) Pt/CO₂-C (b) Pt/H₂O₂-CO₂-C, (c) Pt/KOH-CO₂-C and (d) commercial Pt/C in N₂-saturated 0.1 M HClO₄ at 50 mV s⁻¹; Middle: CO stripping curves (before and after ADT) of (a) Pt/CO₂-C (b) Pt/H₂O₂-CO₂-C, (c) Pt/KOH-CO₂-C and (d) commercial Pt/C in N₂-saturated 0.1 M HClO₄ at 20 mV s⁻¹; Bottom: ORR polarization curves (before and after ADT) of (a) Pt/CO₂-C (b) Pt/H₂O₂-CO₂-C, (c) Pt/KOH-CO₂-C and (d) commercial Pt/C in O₂-saturated 0.1 M HClO₄ at 20 mV s⁻¹ with a rotation rate of 1600 rpm.

5 Conclusions

The aim of this work was to develop high-performance Pt electrocatalysts with sustainable carbon nanomaterial (CO₂-derived carbon) for cathodic oxygen reduction reaction in proton exchange membrane fuel cells. For this goal, the influence of different pretreatment methods was studied on commercial Vulcan XC-72 carbon black material in the first part of the work. Next, a Pt electrocatalyst using CO₂-derived carbon nanomaterial as support was synthesized. In the final section of the work, the findings from the previous studies were applied to pretreat CO₂-derived carbon to achieve enhanced ORR performance of the Pt electrocatalyst. Based on these studies, the following conclusions can be drawn:

1. The first study demonstrated that pretreatment of Vulcan XC-72R with H₂O₂ significantly enhanced the ORR performance of the Pt electrocatalyst as its electrochemically active surface area was measured to be around 36 m² g_{Pt}⁻¹ higher than commercial Pt/C. At the same time, compared with the commercial Pt/C, Pt/XC-72R (H₂O₂ treated) exhibited higher onset potential (60 mV higher), mass and specific activities as well as superior durability. SEM and XRD studies confirmed the optimal Pt nanoparticle sizes (2.9–4.4 nm) and favorable structural defects induced by H₂O₂ pre-treatment, enhancing Pt utilization and ORR performance. These findings highlighted the potential of H₂O₂ pre-treatment as an effective method for achieving high ORR performance.
2. In the second study, a novel platinum electrocatalyst supported by CO₂-derived carbon was synthesized. During electrochemical characterization, the Pt/CO₂-C electrocatalyst demonstrated a 33% higher mass activity and a 9% higher specific activity compared to the commercial Pt/C while experiencing only a 5% loss in mass activity after accelerated durability test (which was 12% for commercial Pt/C). Morphological analysis revealed uniformly distributed Pt nanoparticles sized around 3.2 nm. These results confirmed CO₂-C as a promising sustainable alternative for conventional petroleum-sourced carbon supports.
3. Combining the findings from previous studies, in the third study Pt electrocatalyst using H₂O₂ pretreated CO₂-derived carbon support was prepared. It was observed that functionalization of CO₂-C with H₂O₂ resulted in an increase of 33.5 m² g_{Pt}⁻¹ in EASA, 40 mA mg_{Pt}⁻¹ in mass activity and 316 μA cm⁻²_{Pt} in specific activity compared to the Pt electrocatalyst with untreated CO₂-C support. Functionalization with oxygen groups was found to optimize metal-support interactions, reduce overpotential, and significantly enhance ORR activity and durability. The results of this study concluded the possibility of achieving high ORR performance with electrocatalyst using relatively low Pt loading and sustainable support material.

References

- [1] I. P. on C. C. (IPCC), "Framing and Context," *Global Warming of 1.5°C*, pp. 49–92, May 2022, doi: 10.1017/9781009157940.003.
- [2] Ottmar Edenhofer, Ramon Pichs-Madruga, Youba Sokona, and Kristin Seyboth, "IPCC, 2011: Summary for Policymakers. In: IPCC Special Report on Renewable Energy Sources and Climate Change Mitigation," Cambridge, 2011.
- [3] A. B. Stambouli, "Fuel cells: The expectations for an environmental-friendly and sustainable source of energy," *Renewable and Sustainable Energy Reviews*, vol. 15, no. 9, pp. 4507–4520, Dec. 2011, doi: 10.1016/J.RSER.2011.07.100.
- [4] M. Teotia, S. Singh, B. P. Singh, T. Akitsu, and R. K. Soni, "Combating climate change with nanoparticles," *Nanoparticles and Plant-Microbe Interactions: An Environmental Perspective*, pp. 259–292, Jan. 2023, doi: 10.1016/B978-0-323-90619-7.00005-9.
- [5] E. Najafli *et al.*, "Sustainable CO₂-Derived Nanoscale Carbon Support to a Platinum Catalyst for Oxygen Reduction Reaction," *ACS Appl Nano Mater*, vol. 6, no. 7, pp. 5772–5780, Apr. 2023, doi: 10.1021/acsnm.3c00208.
- [6] E. Najafli, S. Ratso, A. Foroozan, N. Noor, D. C. Higgins, and I. Kruusenberg, "Functionalization of CO₂-Derived Carbon Support as a Pathway to Enhancing the Oxygen Reduction Reaction Performance of Pt Electrocatalysts," *Energy and Fuels*, Aug. 2024, doi: 10.1021/ACS.ENERGYFUELS.4C02407/SUPPL_FILE/EF4C02407_SI_001.PDF.
- [7] E. Najafli, M. Grossberg, V. Mikli, P. Walke, S. Ratso, and I. Kruusenberg, "Optimizing Pt catalyst performance for oxygen reduction reaction via surface functionalization of Vulcan XC-72R carbon black support," *J Appl Electrochem*, pp. 1–14, Jan. 2025, doi: 10.1007/S10800-024-02238-1/FIGURES/9.
- [8] W. F. Pickard, A. Q. Shen, and N. J. Hansing, "Parking the power: Strategies and physical limitations for bulk energy storage in supply–demand matching on a grid whose input power is provided by intermittent sources," *Renewable and Sustainable Energy Reviews*, vol. 13, no. 8, pp. 1934–1945, Oct. 2009, doi: 10.1016/J.RSER.2009.03.002.
- [9] E. B. Agyekum, J. D. Ampah, T. Wilberforce, S. Afrane, and C. Nutakor, "Research Progress, Trends, and Current State of Development on PEMFC-New Insights from a Bibliometric Analysis and Characteristics of Two Decades of Research Output," *Membranes (Basel)*, vol. 12, no. 11, Nov. 2022, doi: 10.3390/MEMBRANES12111103.
- [10] S. Mo *et al.*, "Recent Advances on PEM Fuel Cells: From Key Materials to Membrane Electrode Assembly," *Electrochemical Energy Reviews 2023 6:1*, vol. 6, no. 1, pp. 1–37, Aug. 2023, doi: 10.1007/S41918-023-00190-W.
- [11] H. Hwang, T. Kweon, H. Kang, and Y. Hwang, "Resource and Greenhouse Gas Reduction Effects through Recycling of Platinum-Containing Waste," *Sustainability*, vol. 16, no. 1, p. 80, Dec. 2023, doi: 10.3390/su16010080.
- [12] R. Ma *et al.*, "A review of oxygen reduction mechanisms for metal-free carbon-based electrocatalysts," *NPJ Comput Mater*, vol. 5, no. 1, 2019, doi: 10.1038/s41524-019-0210-3.
- [13] L. Yan *et al.*, "Atomically precise electrocatalysts for oxygen reduction reaction," *Chem*, vol. 9, no. 2, pp. 280–342, Feb. 2023, doi: 10.1016/J.CHEMPR.2023.01.003.

- [14] A. M. Gómez-Marín and J. M. Feliu, "Oxygen Reduction on Platinum Single Crystal Electrodes," *Encyclopedia of Interfacial Chemistry: Surface Science and Electrochemistry*, pp. 820–830, Jan. 2018, doi: 10.1016/B978-0-12-409547-2.13333-5.
- [15] C. Maouche, Y. Zhou, Y. Wang, and J. Yang, "Recent advances of the key parameters of 3d block transition metal single and dual atoms catalysts: from their synthesis to their practical applications," *Materials Today Sustainability*, vol. 21, p. 100288, Mar. 2023, doi: 10.1016/J.MTSUST.2022.100288.
- [16] O. E. Herrera, D. P. Wilkinson, and W. Mérida, "Anode and cathode overpotentials and temperature profiles in a PEMFC," *J Power Sources*, vol. 198, pp. 132–142, Jan. 2012, doi: 10.1016/J.JPOWSOUR.2011.09.042.
- [17] W. Wang, X. Wei, D. Choi, X. Lu, G. Yang, and C. Sun, "Electrochemical cells for medium- and large-scale energy storage: fundamentals," *Advances in Batteries for Medium and Large-Scale Energy Storage: Types and Applications*, pp. 3–28, Jan. 2015, doi: 10.1016/B978-1-78242-013-2.00001-7.
- [18] P. K. Das, X. Li, and Z. S. Liu, "Analytical approach to polymer electrolyte membrane fuel cell performance and optimization," *Journal of Electroanalytical Chemistry*, vol. 604, no. 2, pp. 72–90, Jun. 2007, doi: 10.1016/J.JELECHEM.2007.02.028.
- [19] M. Luo and M. T. M. Koper, "A kinetic descriptor for the electrolyte effect on the oxygen reduction kinetics on Pt(111)," *Nature Catalysis* 2022 5:7, vol. 5, no. 7, pp. 615–623, Jul. 2022, doi: 10.1038/s41929-022-00810-6.
- [20] H. Ooka, J. Huang, and K. S. Exner, "The Sabatier Principle in Electrocatalysis: Basics, Limitations, and Extensions," *Front Energy Res*, vol. 9, p. 654460, May 2021, doi: 10.3389/FENRG.2021.654460/BIBTEX.
- [21] J. K. Nørskov *et al.*, "Origin of the overpotential for oxygen reduction at a fuel-cell cathode," *Journal of Physical Chemistry B*, vol. 108, no. 46, pp. 17886–17892, Nov. 2004, doi: 10.1021/JP047349J/ASSET/IMAGES/LARGE/JP047349JF00008.JPEG.
- [22] M. Y. Chen, Y. Li, H. R. Wu, B. A. Lu, and J. N. Zhang, "Highly Stable Pt-Based Oxygen Reduction Electrocatalysts toward Practical Fuel Cells: Progress and Perspectives," *Materials*, vol. 16, no. 7, Apr. 2023, doi: 10.3390/MA16072590.
- [23] T. S. Andrade and T. Thiringer, "Low platinum fuel cell as enabler for the hydrogen fuel cell vehicle," *J Power Sources*, vol. 598, p. 234140, Apr. 2024, doi: 10.1016/J.JPOWSOUR.2024.234140.
- [24] G. Reverdiau, A. Le Duigou, T. Alleau, T. Aribart, C. Dugast, and T. Priem, "Will there be enough platinum for a large deployment of fuel cell electric vehicles?," *Int J Hydrogen Energy*, vol. 46, no. 79, pp. 39195–39207, Nov. 2021, doi: 10.1016/J.IJHYDENE.2021.09.149.
- [25] L. Fan *et al.*, "Towards ultralow platinum loading proton exchange membrane fuel cells," *Energy Environ Sci*, vol. 16, no. 4, pp. 1466–1479, Apr. 2023, doi: 10.1039/D2EE03169H.
- [26] W. Mabhulusa, K. E. Sekhosana, and X. Fuku, "The impact and performance of carbon-supported platinum group metal electrocatalysts for fuel cells," *Int J Electrochem Sci*, vol. 19, no. 4, p. 100524, Apr. 2024, doi: 10.1016/J.IJOES.2024.100524.
- [27] X. Hu *et al.*, "Review and Perspectives of Carbon-Supported Platinum-Based Catalysts for Proton Exchange Membrane Fuel Cells," *Energy and Fuels*, vol. 37, no. 16, pp. 11532–11566, Aug. 2023, doi: 10.1021/ACS.ENERGYFUELS.3C01265/ASSET/IMAGES/LARGE/EF3C01265_0007.JPEG.

- [28] “Nanostructured Carbon Materials as Catalysts,” in *Nanostructured Carbon Materials for Catalysis*, The Royal Society of Chemistry, 2015, pp. 223–267. doi: 10.1039/9781782622567-00223.
- [29] S. Samad *et al.*, “Carbon and non-carbon support materials for platinum-based catalysts in fuel cells,” *Int J Hydrogen Energy*, vol. 43, no. 16, pp. 7823–7854, Apr. 2018, doi: 10.1016/J.IJHYDENE.2018.02.154.
- [30] S. Khodabakhshi, P. F. Fulvio, and E. Andreoli, “Carbon black reborn: Structure and chemistry for renewable energy harnessing,” *Carbon N Y*, vol. 162, pp. 604–649, Jun. 2020, doi: 10.1016/J.CARBON.2020.02.058.
- [31] M. Kim, J. N. Park, H. Kim, S. Song, and W. H. Lee, “The preparation of Pt/C catalysts using various carbon materials for the cathode of PEMFC,” *J Power Sources*, vol. 163, no. 1, pp. 93–97, Dec. 2006, doi: 10.1016/J.JPOWSOUR.2006.05.057.
- [32] Z. W. Seh, J. Kibsgaard, C. F. Dickens, I. Chorkendorff, J. K. Nørskov, and T. F. Jaramillo, “Combining theory and experiment in electrocatalysis: Insights into materials design,” *Science (1979)*, vol. 355, no. 6321, Jan. 2017, doi: 10.1126/science.aad4998.
- [33] B. Ruiz-Camacho, A. Medina-Ramírez, R. Fuentes-Ramírez, R. Navarro, C. Martínez Gómez, and A. Pérez-Larios, “Pt and Pt–Ag nanoparticles supported on carbon nanotubes (CNT) for oxygen reduction reaction in alkaline medium,” *Int J Hydrogen Energy*, vol. 47, no. 70, pp. 30147–30159, Aug. 2022, doi: 10.1016/J.IJHYDENE.2022.03.190.
- [34] L. La-Torre-Riveros, R. Guzman-Blas, A. E. Méndez-Torres, M. Prelas, D. A. Tryk, and C. R. Cabrera, “Diamond nanoparticles as a support for Pt and PtRu catalysts for direct methanol fuel cells,” *ACS Appl Mater Interfaces*, vol. 4, no. 2, pp. 1134–1147, Feb. 2012, doi: 10.1021/AM2018628/SUPPL_FILE/AM2018628_SI_001.PDF.
- [35] M. Chourashiya, S. T. Vindt, A. A. Velázquez Palenzuela, C. M. Pedersen, C. Kallesøe, and S. M. Andersen, “Low-cost graphite as durable support for Pt-based cathode electrocatalysts for proton exchange membrane based fuel cells,” *Int J Hydrogen Energy*, vol. 43, no. 52, pp. 23275–23284, Dec. 2018, doi: 10.1016/J.IJHYDENE.2018.10.187.
- [36] L. G. Verga, J. Aarons, M. Sarwar, D. Thompsett, A. E. Russell, and C. K. Skylaris, “Effect of graphene support on large Pt nanoparticles,” *Physical Chemistry Chemical Physics*, vol. 18, no. 48, pp. 32713–32722, Dec. 2016, doi: 10.1039/C6CP07334D.
- [37] F. B. Baz, R. M. Elzohary, S. Osman, S. A. Marzouk, and M. Ahmed, “A review of water management methods in proton exchange membrane fuel cells,” *Energy Convers Manag*, vol. 302, p. 118150, Feb. 2024, doi: 10.1016/J.ENCONMAN.2024.118150.
- [38] M. Cavo, E. Gadducci, D. Rattazzi, M. Rivarolo, and L. Magistri, “Dynamic analysis of PEM fuel cells and metal hydrides on a zero-emission ship: A model-based approach,” *Int J Hydrogen Energy*, vol. 46, no. 64, pp. 32630–32644, Sep. 2021, doi: 10.1016/J.IJHYDENE.2021.07.104.
- [39] M. M. Bruno and F. A. Viva, “Carbon Materials for Fuel Cells,” in *Direct Alcohol Fuel Cells*, vol. 9789400777, no. September, H. R. Corti and E. R. Gonzalez, Eds., Dordrecht: Springer Netherlands, 2014, pp. 231–270. doi: 10.1007/978-94-007-7708-8_7.

- [40] E. Simon, B. Leandro, M. Kyoko, N. Todd, and T. Kiyoto, "2006 IPCC Guidelines for National Greenhouse Gas Inventories," 2006. Accessed: Sep. 27, 2022. [Online]. Available: <https://www.ipcc-nggip.iges.or.jp/public/2006gl/index.html>
- [41] R. Chauvy, N. Meunier, D. Thomas, and G. De Weireld, "Selecting emerging CO₂ utilization products for short- to mid-term deployment," *Appl Energy*, vol. 236, pp. 662–680, Feb. 2019, doi: 10.1016/J.APENERGY.2018.11.096.
- [42] X. Zhang, H. Lu, Y. Miao, Y. Zhang, and J. Wang, "New trends in the development of CO₂ electrochemical reduction electrolyzer," *J Environ Chem Eng*, vol. 12, no. 2, p. 112369, Apr. 2024, doi: 10.1016/J.JECE.2024.112369.
- [43] S. Malkhandi and B. S. Yeo, "Electrochemical conversion of carbon dioxide to high value chemicals using gas-diffusion electrodes," *Curr Opin Chem Eng*, vol. 26, pp. 112–121, Dec. 2019, doi: 10.1016/J.COACHE.2019.09.008.
- [44] M. Alvarez-Guerra, J. Albo, E. Alvarez-Guerra, and A. Irabien, "Ionic liquids in the electrochemical valorisation of CO₂," *Energy Environ Sci*, vol. 8, no. 9, pp. 2574–2599, Aug. 2015, doi: 10.1039/C5EE01486G.
- [45] J. W. Fergus, "A review of electrolyte and electrode materials for high temperature electrochemical CO₂ and SO₂ gas sensors," *Sens Actuators B Chem*, vol. 134, no. 2, pp. 1034–1041, Sep. 2008, doi: 10.1016/J.SNB.2008.07.005.
- [46] M. Gattrell, N. Gupta, and A. Co, "A review of the aqueous electrochemical reduction of CO₂ to hydrocarbons at copper," *Journal of Electroanalytical Chemistry*, vol. 594, no. 1, pp. 1–19, Aug. 2006, doi: 10.1016/J.JELECHEM.2006.05.013.
- [47] B. Deng *et al.*, "Molten salt CO₂ capture and electro-transformation (MSCC-ET) into capacitive carbon at medium temperature: effect of the electrolyte composition," *Faraday Discuss*, vol. 190, no. 0, pp. 241–258, Aug. 2016, doi: 10.1039/C5FD00234F.
- [48] D. Chery, V. Lair, and M. Cassir, "CO₂ electrochemical reduction into CO or C in molten carbonates: a thermodynamic point of view," *Electrochim Acta*, vol. 160, pp. 74–81, Apr. 2015, doi: 10.1016/J.ELECTACTA.2015.01.216.
- [49] W. Weng, L. Tang, and W. Xiao, "Capture and electro-splitting of CO₂ in molten salts," *Journal of Energy Chemistry*, vol. 28, pp. 128–143, Jan. 2019, doi: 10.1016/J.JECEM.2018.06.012.
- [50] H. V. Ijije, R. C. Lawrence, and G. Z. Chen, "Carbon electrodeposition in molten salts: Electrode reactions and applications," *Volume 4, Issue 67, Pages 35808 - 35817*, vol. 4, no. 67, pp. 35808–35817, 2014, doi: 10.1039/c4ra04629c.
- [51] D. Tang, H. Yin, X. Mao, W. Xiao, and D. H. Wang, "Effects of applied voltage and temperature on the electrochemical production of carbon powders from CO₂ in molten salt with an inert anode," *Electrochim Acta*, vol. 114, pp. 567–573, Dec. 2013, doi: 10.1016/J.ELECTACTA.2013.10.109.
- [52] X. Cai, X. Liu, Z. Hao, and R. Lin, "Improved Pt dispersion and catalytic performance by modified carbon support with low surface oxygen content and more mesopores," *J Power Sources*, vol. 604, p. 234478, Jun. 2024, doi: 10.1016/J.JPOWSOUR.2024.234478.
- [53] Y. Li, Q. Li, H. Wang, L. Zhang, D. P. Wilkinson, and J. Zhang, "Recent Progresses in Oxygen Reduction Reaction Electrocatalysts for Electrochemical Energy Applications," *Electrochemical Energy Reviews 2019 2:4*, vol. 2, no. 4, pp. 518–538, Oct. 2019, doi: 10.1007/S41918-019-00052-4.

- [54] S. Martin, P. L. Garcia-Ybarra, and J. L. Castillo, "High platinum utilization in ultra-low Pt loaded PEM fuel cell cathodes prepared by electrospraying," *Int J Hydrogen Energy*, vol. 35, no. 19, pp. 10446–10451, Oct. 2010, doi: 10.1016/J.IJHYDENE.2010.07.069.
- [55] V. Tripković, I. Cerri, T. Bligaard, and J. Rossmeisl, "The influence of particle shape and size on the activity of platinum nanoparticles for oxygen reduction reaction: A density functional theory study," *Catal Letters*, vol. 144, no. 3, pp. 380–388, Jan. 2014, doi: 10.1007/S10562-013-1188-Y/FIGURES/6.
- [56] M. Peuckert, T. Yoneda, R. A. D. Betta, and M. Boudart, "Oxygen Reduction on Small Supported Platinum Particles," *J Electrochem Soc*, vol. 133, no. 5, pp. 944–947, May 1986, doi: 10.1149/1.2108769/XML.
- [57] K. Kinoshita, "Particle Size Effects for Oxygen Reduction on Highly Dispersed Platinum in Acid Electrolytes," *J Electrochem Soc*, vol. 137, no. 3, pp. 845–848, Mar. 1990, doi: 10.1149/1.2086566/XML.
- [58] K. Wikander, H. Ekström, A. E. C. Palmqvist, and G. Lindbergh, "On the influence of Pt particle size on the PEMFC cathode performance," *Electrochim Acta*, vol. 52, no. 24, pp. 6848–6855, Aug. 2007, doi: 10.1016/J.ELECTACTA.2007.04.106.
- [59] M. L. Sattler and P. N. Ross, "The surface structure of Pt crystallites supported on carbon black," *Ultramicroscopy*, vol. 20, no. 1–2, pp. 21–28, Jan. 1986, doi: 10.1016/0304-3991(86)90163-4.
- [60] Z. Xu, H. Zhang, H. Zhong, Q. Lu, Y. Wang, and D. Su, "Effect of particle size on the activity and durability of the Pt/C electrocatalyst for proton exchange membrane fuel cells," *Applied Catalysis B*, vol. 111–112, pp. 264–270, Jan. 2012, doi: 10.1016/J.APCATB.2011.10.007.
- [61] L. Gan, H. Da Du, B. H. Li, and F. Y. Kang, "The effect of particle size on the interaction of Pt catalyst particles with a carbon black support," *New Carbon Materials*, vol. 25, no. 1, pp. 53–59, Feb. 2010, doi: 10.1016/S1872-5805(09)60015-9.
- [62] J. Quinson *et al.*, "Investigating Particle Size Effects in Catalysis by Applying a Size-Controlled and Surfactant-Free Synthesis of Colloidal Nanoparticles in Alkaline Ethylene Glycol: Case Study of the Oxygen Reduction Reaction on Pt," *ACS Catal*, vol. 8, no. 7, pp. 6627–6635, Jul. 2018, doi: 10.1021/acscatal.8b00694.
- [63] H. S. Oh, J. G. Oh, Y. G. Hong, and H. Kim, "Investigation of carbon-supported Pt nanocatalyst preparation by the polyol process for fuel cell applications," *Electrochim Acta*, vol. 52, no. 25, pp. 7278–7285, Sep. 2007, doi: 10.1016/J.ELECTACTA.2007.05.080.
- [64] A. Serov *et al.*, "Nano-structured platinum group metal-free catalysts and their integration in fuel cell electrode architectures," *Appl Catal B*, vol. 237, pp. 1139–1147, Dec. 2018, doi: 10.1016/J.APCATB.2017.08.067.
- [65] X. Wang *et al.*, "Review of Metal Catalysts for Oxygen Reduction Reaction: From Nanoscale Engineering to Atomic Design," *Chem*, vol. 5, no. 6, pp. 1486–1511, Jun. 2019, doi: 10.1016/J.CHEMPR.2019.03.002.
- [66] C. Lim, A. R. Fairhurst, B. J. Ransom, D. Haering, and V. R. Stamenkovic, "Role of Transition Metals in Pt Alloy Catalysts for the Oxygen Reduction Reaction," *ACS Catal*, vol. 13, no. 22, pp. 14874–14893, Nov. 2023, doi: 10.1021/ACSCATAL.3C03321/ASSET/IMAGES/LARGE/CS3C03321_0019.JPEG.

- [67] A. M. Jauhar *et al.*, "Space-confined catalyst design toward ultrafine Pt nanoparticles with enhanced oxygen reduction activity and durability," *J Power Sources*, vol. 473, p. 228607, Oct. 2020, doi: 10.1016/J.JPOWSOUR.2020.228607.
- [68] S. W. Lee, S. R. Choi, J. Jang, G. G. Park, S. H. Yu, and J. Y. Park, "Tolerance to carbon corrosion of various carbon structures as catalyst supports for polymer electrolyte membrane fuel cells," *J Mater Chem A Mater*, vol. 7, no. 43, pp. 25056–25065, Nov. 2019, doi: 10.1039/C9TA07941F.
- [69] S. Jayabal, G. Saranya, D. Geng, L. Y. Lin, and X. Meng, "Insight into the correlation of Pt–support interactions with electrocatalytic activity and durability in fuel cells," *J Mater Chem A Mater*, vol. 8, no. 19, pp. 9420–9446, May 2020, doi: 10.1039/D0TA01530J.
- [70] N. Macauley *et al.*, "Carbon Corrosion in PEM Fuel Cells and the Development of Accelerated Stress Tests," *J Electrochem Soc*, vol. 165, no. 6, pp. F3148–F3160, Mar. 2018, doi: 10.1149/2.0061806JES/XML.
- [71] G. Xu, L. Yang, J. Li, C. Liu, W. Xing, and J. Zhu, "Strategies for improving stability of Pt-based catalysts for oxygen reduction reaction," *Advanced Sensor and Energy Materials*, vol. 2, no. 2, p. 100058, Jun. 2023, doi: 10.1016/J.ASEMS.2023.100058.
- [72] A. Kumar, E. J. Park, Y. S. Kim, and J. S. Spendelow, "Surface Functionalization of Carbon Black for PEM Fuel Cell Electrodes," *Macromol Chem Phys*, vol. 225, no. 18, p. 2400092, Sep. 2024, doi: 10.1002/MACP.202400092.
- [73] M. X. Wang *et al.*, "Enhancing the catalytic performance of Pt/C catalysts using steam-etched carbon blacks as a catalyst support," *Carbon N Y*, vol. 49, no. 1, pp. 256–265, Jan. 2011, doi: 10.1016/J.CARBON.2010.09.013.
- [74] J. Islam, S. K. Kim, K. H. Kim, E. Lee, and G. G. Park, "Enhanced durability of Pt/C catalyst by coating carbon black with silica for oxygen reduction reaction," *Int J Hydrogen Energy*, vol. 46, no. 1, pp. 1133–1143, Jan. 2021, doi: 10.1016/J.IJHYDENE.2020.09.194.
- [75] K. Loganathan, D. Bose, and D. Weinkauff, "Surface modification of carbon black by nitrogen and allylamine plasma treatment for fuel cell electrocatalyst," *Int J Hydrogen Energy*, vol. 39, no. 28, pp. 15766–15771, Sep. 2014, doi: 10.1016/J.IJHYDENE.2014.07.125.
- [76] L. Nayak, M. Rahaman, and R. Giri, "Surface Modification/Functionalization of Carbon Materials by Different Techniques: An Overview," pp. 65–98, 2019, doi: 10.1007/978-981-13-2688-2_2.
- [77] M. J. Lázaro, L. Calvillo, V. Celorrio, J. I. Pardo, S. Perathoner, and R. Moliner, "Study and application of carbon black vulcan XC-72R in polymeric electrolyte fuel cells," in *Carbon Black: Production, Properties and Uses*, Nova Science Publishers, Inc., 2011, pp. 41–68.
- [78] M. Shao, "Electrocatalysis in Fuel Cells," *Catalysts 2015, Vol. 5, Pages 2115–2121*, vol. 5, no. 4, pp. 2115–2121, Dec. 2015, doi: 10.3390/CATAL5042115.
- [79] S. M. S. Kumar, N. Hidyatai, J. S. Herrero, S. Irusta, and K. Scott, "Efficient tuning of the Pt nano-particle mono-dispersion on Vulcan XC-72R by selective pre-treatment and electrochemical evaluation of hydrogen oxidation and oxygen reduction reactions," *Int J Hydrogen Energy*, vol. 36, no. 9, pp. 5453–5465, May 2011, doi: 10.1016/J.IJHYDENE.2011.01.124.

- [80] X. Cheng, G. Wei, C. Wang, S. Shen, and J. Zhang, "Experimental probing of effects of carbon support on bulk and local oxygen transport resistance in ultra-low Pt PEMFCs," *Int J Heat Mass Transf*, vol. 164, p. 120549, Jan. 2021, doi: 10.1016/J.IJHEATMASSTRANSFER.2020.120549.
- [81] A. Bard and L. Faulkner, *Electrochemical Methods: Fundamentals and Applications*, 2nd ed. John Wiley & Sons, 2001.
- [82] N. M. Marković, H. A. Gasteiger, B. N. Grgur, and P. N. Ross, "Oxygen reduction reaction on Pt(111): effects of bromide," *Journal of Electroanalytical Chemistry*, vol. 467, no. 1–2, pp. 157–163, Jun. 1999, doi: 10.1016/S0022-0728(99)00020-0.
- [83] Y. Garsany, O. A. Baturina, K. E. Swider-Lyons, and S. S. Kocha, "Experimental methods for quantifying the activity of platinum electrocatalysts for the oxygen reduction reaction," *Anal Chem*, vol. 82, no. 15, pp. 6321–6328, 2010, doi: 10.1021/ac100306c.
- [84] M. Lukaszewski, M. Soszko, and A. Czerwiński, "Electrochemical Methods of Real Surface Area Determination of Noble Metal Electrodes – an Overview," *Int J Electrochem Sci*, vol. 11, no. 6, pp. 4442–4469, Jun. 2016, doi: 10.20964/2016.06.71.
- [85] C. A. Schneider, W. S. Rasband, and K. W. Eliceiri, "NIH Image to ImageJ: 25 years of image analysis," *Nature Methods* 2012 9:7, vol. 9, no. 7, pp. 671–675, Jun. 2012, doi: 10.1038/nmeth.2089.
- [86] W. P. Davey, "Precision Measurements of the Lattice Constants of Twelve Common Metals," *Physical Review*, vol. 25, no. 6, p. 753, Jun. 1925, doi: 10.1103/PhysRev.25.753.
- [87] A. Ferrari and J. Robertson, "Interpretation of Raman spectra of disordered and amorphous carbon," *Phys Rev B Condens Matter Mater Phys*, vol. 61, no. 20, 2000, doi: 10.1103/PhysRevB.61.14095.
- [88] L. Peng *et al.*, "Highly mesoporous metal–organic framework assembled in a switchable solvent," *Nat Commun*, vol. 5, no. 1, p. 4465, Jul. 2014, doi: 10.1038/ncomms5465.
- [89] Y. Zhao, Y. Chu, X. Ju, J. Zhao, L. Kong, and Y. Zhang, "Carbon-Supported Copper-Based Nitrogen-Containing Supramolecule as an Efficient Oxygen Reduction Reaction Catalyst in Neutral Medium," *Catalysts* 2018, Vol. 8, Page 53, vol. 8, no. 2, p. 53, Jan. 2018, doi: 10.3390/CATAL8020053.
- [90] W. Zhang, A. U. Shaikh, E. Y. Tsui, and T. M. Swager, "Cobalt porphyrin functionalized carbon nanotubes for oxygen reduction," *Chemistry of Materials*, vol. 21, no. 14, pp. 3234–3241, Jul. 2009, doi: 10.1021/CM900747T/SUPPL_FILE/CM900747T_SI_001.PDF.
- [91] J. H. Kim, Y. T. Kim, and S. H. Joo, "Electrocatalyst design for promoting two-electron oxygen reduction reaction: Isolation of active site atoms," *Curr Opin Electrochem*, vol. 21, pp. 109–116, Jun. 2020, doi: 10.1016/J.COEELEC.2020.01.007.
- [92] Z. Li, L. Deng, I. A. Kinloch, and R. J. Young, "Raman spectroscopy of carbon materials and their composites: Graphene, nanotubes and fibres," *Prog Mater Sci*, vol. 135, p. 101089, Jun. 2023, doi: 10.1016/J.PMATSCI.2023.101089.
- [93] F. T. Wagner, B. Lakshmanan, and M. F. Mathias, "Electrochemistry and the Future of the Automobile," *J. Phys. Chem. Lett*, vol. 1, pp. 2204–2219, 2010, doi: 10.1021/jz100553m.

- [94] S. Guo, S. Zhang, and S. Sun, "Tuning nanoparticle catalysis for the oxygen reduction reaction," *Angewandte Chemie - International Edition*, vol. 52, no. 33, pp. 8526–8544, Aug. 2013, doi: 10.1002/ANIE.201207186.
- [95] N. Hodnik *et al.*, "Assembly of Pt Nanoparticles on Graphitized Carbon Nanofibers as Hierarchically Structured Electrodes," *ACS Appl Nano Mater*, vol. 3, no. 10, pp. 9880–9888, Oct. 2020, doi: 10.1021/acsanm.0c01945.
- [96] M. Shao, *Electrocatalysis in Fuel Cells*. in Lecture Notes in Energy. Springer London, 2013. doi: 10.1007/978-1-4471-4911-8.
- [97] J.-B. Wu, M.-L. Lin, X. Cong, H.-N. Liu, and P.-H. Tan, "Raman spectroscopy of graphene-based materials and its applications in related devices," *Chem Soc Rev*, vol. 47, no. 5, pp. 1822–1873, 2018, doi: 10.1039/C6CS00915H.
- [98] M. Lázaro, L. Calvillo, V. Celorrio, J. I. Pardo, S. Perathoner, and R. Moliner, "Study and application of Vulcan XC-72 in low temperature fuel cells," in *Carbon Black: Production, Properties and Uses*, 2011, pp. 1–28.
- [99] C. Du, Y. Sun, T. Shen, G. Yin, and J. Zhang, "Applications of RDE and RRDE Methods in Oxygen Reduction Reaction," in *Rotating Electrode Methods and Oxygen Reduction Electrocatalysts*, Elsevier, 2014, pp. 231–277. doi: 10.1016/B978-0-444-63278-4.00007-0.
- [100] T. Shinagawa, A. T. Garcia-Esparza, and K. Takanahe, "Insight on Tafel slopes from a microkinetic analysis of aqueous electrocatalysis for energy conversion," *Sci Rep*, vol. 5, no. 1, p. 13801, Nov. 2015, doi: 10.1038/srep13801.
- [101] A. Holewinski and S. Linic, "Elementary Mechanisms in Electrocatalysis: Revisiting the ORR Tafel Slope," *J Electrochem Soc*, vol. 159, no. 11, pp. H864–H870, 2012, doi: 10.1149/2.022211JES.
- [102] N. M. Marković, H. A. Gasteiger, B. N. Grgur, and P. N. Ross, "Oxygen reduction reaction on Pt(111): effects of bromide," *Journal of Electroanalytical Chemistry*, vol. 467, no. 1–2, pp. 157–163, Jun. 1999, doi: 10.1016/S0022-0728(99)00020-0.
- [103] H. A. Hansen, V. Viswanathan, and J. K. Nørskov, "Unifying Kinetic and Thermodynamic Analysis of 2 e⁻ and 4 e⁻ Reduction of Oxygen on Metal Surfaces," *J. Phys. Chem. C*, vol. 118, p. 57, 2014, doi: 10.1021/jp4100608.
- [104] W. Chen *et al.*, "Reconsidering the Benchmarking Evaluation of Catalytic Activity in Oxygen Reduction Reaction," *iScience*, vol. 23, no. 10, p. 101532, Oct. 2020, doi: 10.1016/j.isci.2020.101532.
- [105] J. X. Wang, F. A. Uribe, T. E. Springer, J. Zhang, and R. R. Adzic, "Intrinsic kinetic equation for oxygen reduction reaction in acidic media: the double Tafel slope and fuel cell applications," *Faraday Discuss*, vol. 140, no. 0, pp. 347–362, Oct. 2008, doi: 10.1039/B802218F.
- [106] S. Guo, S. Zhang, and S. Sun, "Tuning nanoparticle catalysis for the oxygen reduction reaction," *Angew Chem Int Ed Engl*, vol. 52, no. 33, pp. 8526–8544, Aug. 2013, doi: 10.1002/ANIE.201207186.
- [107] C. Jackson *et al.*, "Electronic metal-support interaction enhanced oxygen reduction activity and stability of boron carbide supported platinum," *Nature Communications 2017 8:1*, vol. 8, no. 1, pp. 1–11, Jun. 2017, doi: 10.1038/ncomms15802.
- [108] Y. Dong *et al.*, "Enhanced catalytic performance of Pt by coupling with carbon defects," *The Innovation*, vol. 2, p. 100161, 2021, doi: 10.1016/j.xinn.2021.100161.

- [109] Q. Q. Yan *et al.*, “Reversing the charge transfer between platinum and sulfur-doped carbon support for electrocatalytic hydrogen evolution,” *Nature Communications* 2019 10:1, vol. 10, no. 1, pp. 1–9, Oct. 2019, doi: 10.1038/s41467-019-12851-w.
- [110] H. Zhang *et al.*, “Crucial role for oxygen functional groups in the oxygen reduction reaction electrocatalytic activity of nitrogen-doped carbons,” *Electrochim Acta*, vol. 292, pp. 942–950, Dec. 2018, doi: 10.1016/J.ELECTACTA.2018.09.175.
- [111] J. H. Kim, J. Y. Cheon, T. J. Shin, J. Y. Park, and S. H. Joo, “Effect of surface oxygen functionalization of carbon support on the activity and durability of Pt/C catalysts for the oxygen reduction reaction,” *Carbon N Y*, vol. 101, pp. 449–457, May 2016, doi: 10.1016/J.CARBON.2016.02.014.
- [112] M. Jerigová, M. Odziomek, and N. López-Salas, “‘We Are Here!’ Oxygen Functional Groups in Carbons for Electrochemical Applications,” *ACS Omega*, vol. 7, no. 14, pp. 11544–11554, Apr. 2022, doi: 10.1021/acsomega.2c00639.
- [113] L. Pavko *et al.*, “Correlating oxygen functionalities and electrochemical durability of carbon supports for electrocatalysts,” *Carbon N Y*, vol. 215, p. 118458, Nov. 2023, doi: 10.1016/J.CARBON.2023.118458.
- [114] D. Bhalothia, A. Beniwal, C. Yan, K. C. Wang, C. H. Wang, and T. Y. Chen, “Potential synergy between Pt₂Ni₄ Atomic-Clusters, oxygen vacancies and adjacent Pd nanoparticles outperforms commercial Pt nanocatalyst in alkaline fuel cells,” *Chemical Engineering Journal*, vol. 483, p. 149421, Mar. 2024, doi: 10.1016/J.CEJ.2024.149421.
- [115] P. S. Cappellari, G. García, J. Florez-Montaña, C. A. Barbero, E. Pastor, and G. A. Planes, “Enhanced formic acid oxidation on polycrystalline platinum modified by spontaneous deposition of gold. Fourier transform infrared spectroscopy studies,” *J Power Sources*, vol. 296, pp. 290–297, Nov. 2015, doi: 10.1016/J.JPOWSOUR.2015.07.005.
- [116] J. M. Linge, H. Erikson, M. Merisalu, V. Sammelseg, and K. Tammeveski, “Oxygen reduction on silver catalysts electrodeposited on various nanocarbon supports,” *SN Appl Sci*, vol. 3, no. 2, pp. 1–10, Feb. 2021, doi: 10.1007/S42452-021-04289-X/FIGURES/7.

Acknowledgements

I acknowledge my supervisors Dr. Ivar Kruusenberg and Dr. Sander Ratso for their contributions to this work.

I would like to thank my colleagues from KBFI and TalTech for their help with experiments, data analysis, thesis writing and publications. I am especially grateful to Dr. Mehmet Ender Uslu, Ehsan Zarmehri, Maryam Kazemi, Dr. Kerli Liivand, Dr. Ragle Raudsepp, Dr. Kätlin Kaare, Dr. Roberto A. Martínez-Rodríguez, Reio Praats, Martin Jantson, Dr. Mai Uibu and Laura Kiolein. I appreciate the collaboration of the co-authors for our publications and especially thank Prof. Dr. Nejc Hodnik and Dr. Matija Gatalo for hosting me at their institute and for their assistance with my research work during my visit.

This work was supported by the Estonian Research Council grants PSG312, PUTJD1233, EAG271, and under ESA Contract No. 4000134761/21/NL/GLC/my by the European Space Agency and by the National Institute of Chemical Physics and Biophysics and the Natural Sciences and Engineering Research Council of Canada (NSERC) International Collaboration program and ERA.Net RUS Plus grant “HeDoCat.”

I would also like to express my heartfelt appreciation to my wife, my parents and my brother for their endless support during the PhD journey. It would not be possible to complete this work without them.

Abstract

Electrochemical Reduction of Oxygen on Platinum–Modified Carbon Materials

Proton exchange membrane fuel cells (PEMFCs) are among the most promising clean energy technologies due to their many advantages such as low emissions, portability, high power density and fast start-up. However, they require platinum–based electrocatalysts for the sluggish cathodic oxygen reduction reaction (ORR). The high cost and scarcity of platinum, reliance on petroleum–derived carbon supports, and the need for improved performance and durability pose significant challenges to the widespread adoption of PEMFCs. This thesis explores approaches to address these issues by developing a novel CO₂–derived carbon (CO₂–C) support to replace conventional petroleum-derived carbon and finding an effective support pretreatment method to enhance the ORR performance of the Pt electrocatalyst supported with CO₂–C. The aim is to achieve high-performance and cost-effective Pt electrocatalysts using sustainable carbon support.

Based on three peer-reviewed publications, this work investigates the impact of various pretreatment methods on commercial Vulcan XC-72 carbon black, explores the possibility of replacing conventional carbon black support with CO₂–C and studies the pretreatment of CO₂–C as a method to enhance ORR performance of Pt electrocatalyst. In the first study, hydrogen peroxide (H₂O₂) pretreatment of Vulcan XC-72 was found to significantly improve the electrochemically active surface area (EASA) of Pt electrocatalyst by 46.3% compared to commercial Pt/C, achieving superior ORR performance. The second study demonstrated that CO₂–C is a sustainable and efficient alternative to petroleum-sourced carbon black support, as Pt/CO₂–C showed a 33% higher mass activity and 9% higher specific activity compared to commercial Pt/C while retaining 95% of its initial mass activity after accelerated durability test (ADT). In the third study, a Pt electrocatalyst supported on H₂O₂–pretreated CO₂–derived carbon was developed, building on previous findings. Functionalization with H₂O₂ improved the EASA, mass activity, and specific activity compared to the untreated CO₂–C based electrocatalyst. This treatment optimized metal-support interaction, reduced overpotential, and significantly enhanced ORR activity and durability. The study demonstrated the potential of achieving high ORR performance with low Pt loading on a sustainable CO₂–C support. The findings, supported by comprehensive electrochemical and physical characterizations, introduce CO₂–derived carbon as a novel and sustainable carbon support alternative for Pt electrocatalysts and highlight the role of support pretreatment in enhancing ORR performance.

In conclusion, this thesis contributes to the advancement of PEMFC technology by addressing the dual challenges of material cost and sustainability. The adoption of CO₂–derived carbon (CO₂–C) as a sustainable replacement for conventional petroleum–sourced carbon black, combined with effective pretreatment strategies, offers a promising pathway to reduce platinum loading in commercial Pt electrocatalysts while advancing clean energy technologies and supporting global decarbonization efforts.

Lühikokkuvõte

Elektrokeemiline hapniku redutseerumine plaatinaga modifitseeritud süsinikmaterjalidel

Prootonvahetusmembraaniga kütuseelement (PEMFC) on üks lootustandvamaid tehnoloogiaid sisepõlemismootori asendamiseks tänu nende paljudele eelistele nagu heitmevabadus (ainuke produkt lisaks energiale ja soojusele on vesi), füüsiline suurus võrreldes näiteks akudega, suur võimsustihedus ja kiire käivitatavus. Paraku vajavad nad aeglase katoodse hapniku redutseerimise reaktsiooni (ORR) efektiivseks muutmiseks plaatinapõhiseid elektrokatalüsaatoreid. Plaatina kõrge hind ja nappus, sõltuvus naftast saadud süsinikukandjatest ning suur vajalik plaatina kogus efektiivsuse ja vastupidavuse tõstmiseks seavad PEMFC-de laialdasele kasutuselevõtmisele olulisi väljakutseid. See lõputöö uurib lähenemisviise nende probleemide lahendamiseks, töötades välja uude CO₂-st saadud süsiniku (CO₂-C) kandematerjali, mis asendaks tavapärase naftast pärineva süsiniku. Lisaks sellele on töö osa eeltötlusmeetodi väljatöötamine, et parandada CO₂-C-l põhinevate Pt/C katalüsaatorite aktiivsust.

Nende eesmärkide saavutamiseks valiti selles töös kolm lähenemist: eeltötlusmeetodite väljatöötamine katalüsaatori aktiivsuse suurendamiseks Vulcan XC-72 süsiniku näitel, kommertsiaalsete süsinikkandjate asendamine CO₂-l põhineva süsinikuga, ning seejärel nende kombineerimine eeltöödetud CO₂-süsiniku uurimiseks süsinikkandjana Pt-katalüsaatorile.

Esimeses osas leiti, et Vulcan XC-72 eeltötlus vesinikperoksiidiga (H₂O₂) parandas Pt elektrokatalüsaatori elektrokeemiliselt aktiivset eripinda (EASA) 46,3% võrra võrreldes kaubandusliku Pt/C-ga, mis suurendas märkimisväärselt selle materjali aktiivsust hapniku elektrokatalüütilisel redutseerumisel. Teine töö osa tõestas, et CO₂-C on jätkusuutlik ja tõhus alternatiiv fossiilkütustel põhinevale süsinkule, kuna Pt/CO₂-C näitas 33% suuremat massaktiivsust ja 9% kõrgemat eriaktiivsust võrreldes kommertsiaalse Pt/C materjaliga, säilitades samal ajal 95 % selle esialgsest massiaktiivsusest pärast stabiilsustesti. Kolmandas töös osas töötati eelnevale kahele uurimusele tuginedes välja Pt elektrokatalüsaator H₂O₂-ga eeltöödeldud CO₂-st saadud süsinikkandjal. Funktsionaliseerimine H₂O₂-ga parandas EASA-d, massaktiivsust ja eriaktiivsust võrreldes töötlemata CO₂-C-põhise elektrokatalüsaatoriga. See töötlemine suurendas efektiivsust läbi Pt ja süsinikkandja sidemete tuginemise, vähendades seeläbi ülepinget ning suurendades oluliselt ORR-i aktiivsust ja katalüsaatormaterjali vastupidavust. Uuring näitas jätkusuutliku CO₂-C toega ja madala Pt-sisaldusega katalüsaatorite eeliseid praeguste lahenduste ees.

Selle lõputöö põhitulemuseks on PEMFC-tehnoloogia edasiarendused, mis vähendavad materjalikulu ja suurendavad katalüsaatormaterjalide jätkusuutlikkust. CO₂-C kasutuselevõtt tavapärase naftast pärineva süsiniktahma jätkusuutliku asendajana koos tõhusate eeltötlusstrateegiatega pakub paljutöötavat võimalust vähendada plaatina sisaldust kommertsiaalsetes Pt elektrokatalüsaatorites, jäädes samas CO₂ neutraalseks mitte ainult energia, vaid ka energia tootmiseks vajalike materjalide valmistamisel.

Appendix 1

Publication I

Erkin Najafli, Maarja Grossberg, Valdek Mikli, Peter Walke, Sander Ratso, Ivar Kruusenberg, Optimizing Pt Catalyst Performance for Oxygen Reduction Reaction via Surface Functionalization of Vulcan XC-72R Carbon Black Support Journal of Applied Electrochemistry 2025, in press. DOI: 10.1007/s10800-024-02238-1.

Sustainable CO₂-Derived Nanoscale Carbon Support to a Platinum Catalyst for Oxygen Reduction Reaction

Erkin Najafli, Sander Ratso, Yurii P. Ivanov, Matija Gatalo, Luka Pavko, Can Rüstü Yörük, Peter Walke, Giorgio Divitini, Nejc Hodnik, and Ivar Kruusenberg*

Cite This: *ACS Appl. Nano Mater.* 2023, 6, 5772–5780

Read Online

ACCESS |

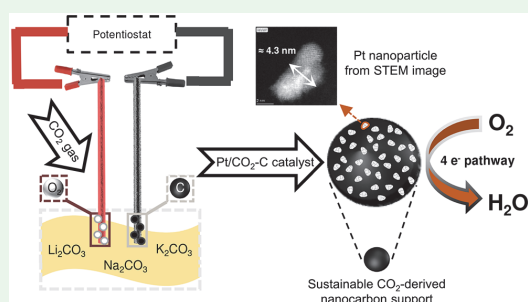
Metrics & More

Article Recommendations

Supporting Information

ABSTRACT: While fuel cells have the potential to be among the key players in clean energy production, they are challenged by the sluggish electrochemical reactions that require an expensive and scarce platinum (Pt) catalyst. Commercial Pt-based catalysts used for facilitating the hydrogen oxidation reaction and oxygen reduction reaction (ORR) in fuel cells are commonly supported by petroleum-sourced carbon materials such as Vulcan XC-72. Thus, the replacement of such support materials with sustainable alternatives while enhancing the catalyst activity is highly desirable. For the first time, a Pt catalyst supported with a sustainably manufactured nanoscale CO₂-derived carbon (Pt/CO₂-C) was synthesized in this work. Physical and electrochemical characterization of the catalyst revealed the superior activity of Pt/CO₂-C toward the ORR in comparison to commercial Pt/C with higher onset potential, mass activity, and specific activity values. Via further improvement, the prepared catalyst material is deemed to be a promising candidate for cheaper and more sustainable fuel cells.

KEYWORDS: fuel cell, oxygen reduction reaction, platinum catalyst, sustainable catalyst support, molten salt electrolysis



1. INTRODUCTION

Fuel cells are among the most promising clean energy technologies that can play a role in the shift to sustainable energy systems, which are urgently needed to withstand the current climate emergency. As the most mature and widely used type of fuel cell,¹ the low-temperature proton-exchange membrane fuel cell (PEMFC) is known for its clean and smooth operation and high energy density output.² By using hydrogen as a fuel and oxygen (or air) as an oxidant to convert chemical energy to electrical energy, PEMFC can reach a competitive energy efficiency of up to 40–50%.³ However, the technology comes with a major limitation originating from the sluggish kinetics⁴ of the oxygen reduction reaction (ORR) occurring on the cathode side of the fuel cell. While various metal-free catalysts such as iron- and nitrogen-doped carbons^{5,6} and metal–organic-framework-derived hollow-structured materials⁷ are being developed, the state-of-the-art catalyst used for this reaction is typically prepared by depositing expensive and scarce Pt on a carbon black support.^{8,9} Employing a support material like carbon considerably influences¹⁰ the performance and durability of the catalyst because it increases the electrical conductivity, and its pore structure brings catalyst particles closer to the reactant. Furthermore, a carbon support provides other advantages like resistance to acidic and basic environments, stability under

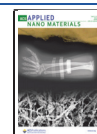
high temperatures, and the possibility of metal recovery by burning away the carbon.¹¹ Thus, the choice of the support material indirectly influences the performance and economic feasibility of fuel cell technology. The most commonly used carbon black types like Vulcan XC-72 and Ketjenblack are, in fact, sourced from petroleum products¹⁰ by pyrolyzing hydrocarbons. It is estimated that the production of carbon black via the conventional “furnace black” process emits around 2.62 t of CO₂ per metric ton of carbon black manufactured.¹² Hence, there is a growing need to replace the conventional carbon support materials used in PEMFC applications with carbon materials that are manufactured sustainably while improving the metal utilization in catalysts to bring the overall cost down.

Molten salt carbon capture and electrochemical transformation (MSCC-ET) is a sustainable and practical method to capture and convert CO₂ to carbon nanomaterials.¹³ In this method, first carbonate salt mixtures are heated to their

Received: January 13, 2023

Accepted: March 3, 2023

Published: March 21, 2023



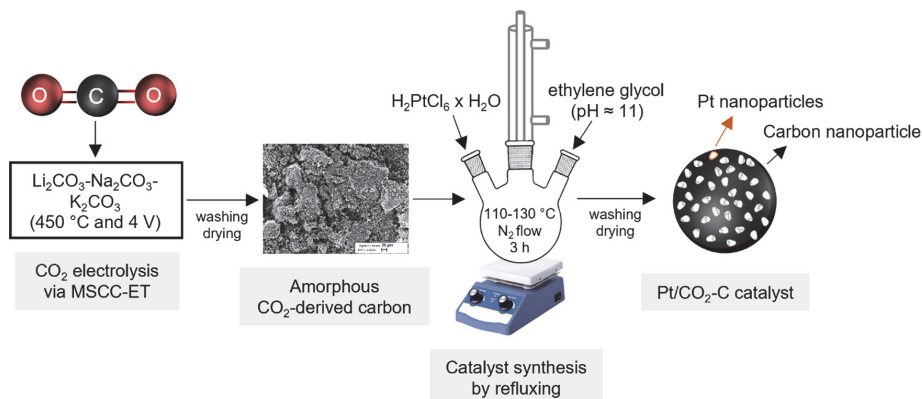


Figure 1. Schematic diagram of the Pt/CO₂-C catalyst synthesis steps.

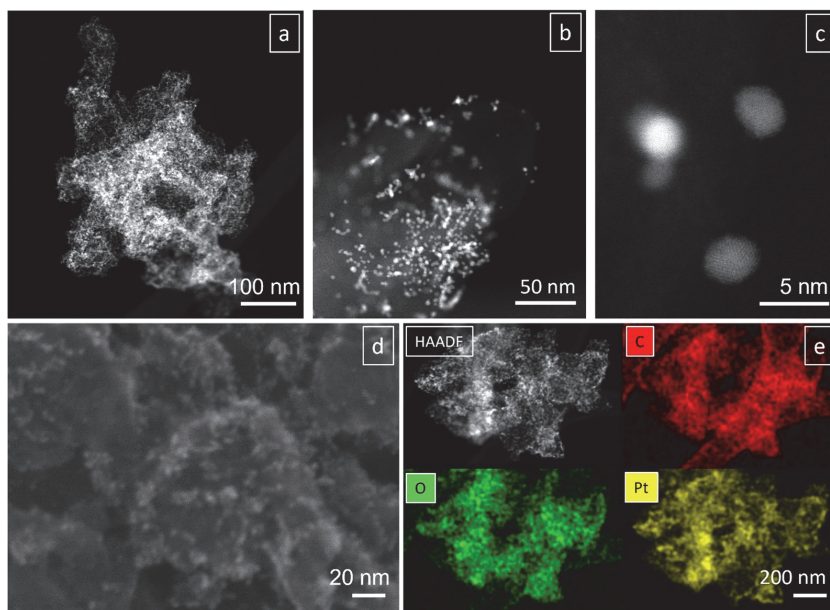


Figure 2. Morphology of Pt/CO₂-C: (a–c) HAADF-STEM images of the composite; (d) SEM image; (e) HAADF-STEM image with elemental maps (white, HAADF; red, C; green, O; yellow, Pt).

melting temperatures in a reactor to capture CO₂; this step is followed by inserting electrodes and applying a voltage to produce porous carbon at the cathode. A four-electron reduction of CO₂ into elemental carbon takes place on the cathode, while oxygen (O₂) gas is produced at the anode from the oxide anions. In addition, the oxide anions react with CO₂ above the melt, regenerating the carbonate salt.¹³ Adjusting the synthesis conditions allows one to tune the morphology and porosity of the resulting carbon, meaning that the method can be used to rationally design carbon support materials, which we previously demonstrated by creating high-performing catalysts, both metal-free and with nonprecious metal, as well as battery electrodes using MSCC-ET.^{14,15} The purpose of this work is to substitute the traditional and environmentally

unfriendly carbon supports with a novel and sustainable carbon nanomaterial (in short CO₂-C) derived from captured CO₂ gas, while not sacrificing the catalyst activity at the expense of sustainability. To the best of our knowledge, this is the first study into the application of this nanomaterial as a support for a Pt catalyst in acidic ORR. By the deposition of Pt nanoparticles onto CO₂-C via polyol synthesis and a thorough physicochemical analysis, the Pt catalyst supported on CO₂-C (abbreviated as Pt/CO₂-C) is demonstrated to exhibit superior catalytic activity in comparison to the commercially available Pt catalyst supported on petroleum-derived carbon black.

2. RESULTS AND DISCUSSION

2.1. Catalyst Preparation and Physical Characterization. The support material (CO₂-C) was obtained from the electrolysis of CO₂ in a molten eutectic mixture of Li₂CO₃–Na₂CO₃–K₂CO₃. The deposition of Pt nanoparticles on CO₂-C was realized by polyol synthesis, in which pH-adjusted ethylene glycol was used as both the solvent and reducing agent. A schematic diagram of the catalyst synthesis steps is provided in Figure 1.

To confirm the Pt loading for a fair comparison with the commercial benchmark, energy-dispersive X-ray spectroscopy (EDS) and thermogravimetric analysis (TGA) were performed, and the results from both elemental analysis tools demonstrated (Figure S1) that Pt/CO₂-C contains around 17 wt % (on average) Pt on the carbon support. The small deviation from the target loading of 20 wt % can be explained by certain impurities in the sample as well as incomplete reduction of the Pt salt during synthesis.

The acquired scanning electron microscopy (SEM) and scanning transmission electron microscopy (STEM) micrographs (Figure 2) of Pt/CO₂-C show that the Pt nanoparticles are uniformly dispersed on the CO₂-C support and the morphology of Pt/CO₂-C is highly comparable to the morphology of the commercial Pt/C catalyst (Figure S2). In the case of the stock CO₂-C, its structure is observed to be amorphous with particles of widely ranging sizes from the SEM image (Figure S3). For Pt/CO₂-C, the mean particle size of Pt nanoparticles on CO₂-C was obtained from the STEM images and found to be, on average, 3.2 nm, which is comparable in size to the nanoparticles of the commercial sample (~3.4 nm). At the same time, both materials have a narrow particle size distribution histogram (Figure S4), indicating a better distribution in terms of uniformity. Because the particle size influences¹⁶ the activity of the supported catalysts, several studies^{17–21} have reported that for Pt nanoparticles the optimal particle size window for achieving the maximum mass activity toward the ORR is between 3 and 5 nm. This partly explains the higher mass activity of Pt/CO₂-C for the ORR, which will be discussed later. It must be noted that, apart from the synthesis parameters,²² the support also affects the Pt nanoparticle size by controlling the extent of agglomeration caused by individual particles.¹⁶ Thus, CO₂-C can be considered as a promising support material for tuning the Pt nanoparticle size.

The X-ray diffraction (XRD) patterns for both samples are given in Figure 3 with their respective reference patterns. The main difference between the observed patterns arises from the kind of support material used for the synthesis. In the case of Pt/CO₂-C, a distinctive peak at around a 2θ value of 29.4° is detected and linked to the XRD pattern of chromite (Cr₂FeO₄) at around 30°, which originates from the stainless-steel electrodes used for the synthesis of CO₂-C. A smaller shoulder peak at around 43° is also attributed to the chromite pattern. While the information about the catalytic activity of chromite is not present in the literature, chromium and iron transition metals were reported²³ to improve the catalytic activity toward the ORR when alloyed with Pt. However, it must be noted that the relative amount of chromite in Pt/CO₂-C was found to be negligible in both the XRD and TGA results; thus, the effect of chromium and iron on the catalytic activity of Pt/CO₂-C is considered to be minimal. For both samples, 2θ angles close to 40° and 46°

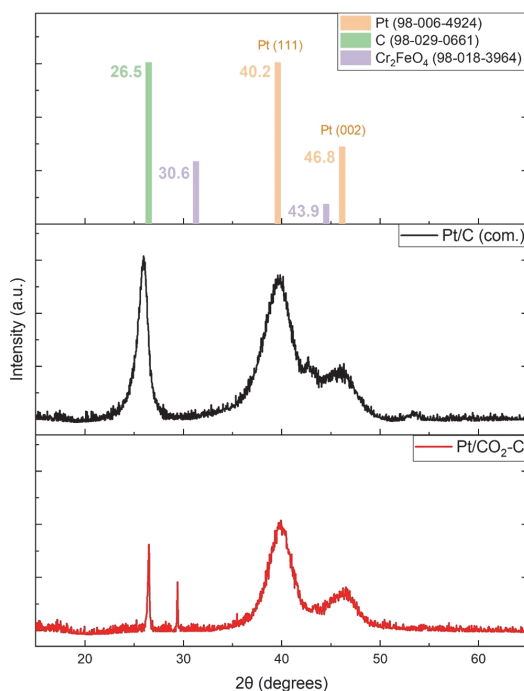


Figure 3. XRD patterns for the Pt/C (commercial) and Pt/CO₂-C samples. The reference patterns are on top.

correspond to the Pt(111) and Pt(002) reflection planes, respectively. It has been shown that, in weakly adsorbed electrolytes (including the HClO₄ solution used in this study), the Pt(111) facet exhibits higher ORR activity than Pt(100).²⁴ Thus, the presence of Pt(111) facets in Pt/CO₂-C is preferred.

For Raman analysis, stock CO₂-C was characterized in addition to Pt/CO₂-C and the commercial benchmark. The most important region of the Raman spectra for carbon ranges from 1000 to 2000 cm⁻¹, where it is possible to detect two distinctive bands at around 1350 and 1600 cm⁻¹, known as the D and G bands, respectively. The D band is linked to the disorder in the carbon structure, while the G band is caused by in-plane vibrations of sp²-bonded carbon atoms.²⁵ Representative raw spectra are shown for each material in Figure S5. These suggest that CO₂-C largely retains its structure following Pt loading. Nonetheless, when stock CO₂-C and Pt/CO₂-C are compared, several key differences can be observed. For instance, the I_D/I_G ratio and full width at half-maximum (fwhm; Table S1) values of the spectra are lower in the case of Pt/CO₂-C. These changes suggest a moderate increase in graphitization of the carbon structure and a decrease in disorder following the Pt deposition. A similar phenomenon was observed by another group working on carbon nanofibers decorated with Pt nanoparticles.²⁶ It has been noted that Pt nanoparticles favor attachment almost exclusively to the defect or edge sites of nonmodified carbons,²⁷ and this could explain how the support's crystal structure gets more ordered after Pt loading (which might be the reason why a sharper and narrower G band is detected in the case of Pt/CO₂-C). Accordingly, the disordered nature of CO₂-C is considered to be an asset for homogeneous Pt dispersion, leading to higher

catalytic activity. Greater differences are seen in the case of the commercial sample. Here, the I_p/I_G ratio is slightly higher than that of Pt/CO₂-C, while the fwhm values for the peaks are considerably smaller, suggesting a narrower structural distribution, and a prominent so-called 2D band is present around 2700 cm⁻¹ such that the spectra resemble that of defected graphene.²⁸

The textural properties of both samples were characterized by N₂ physisorption and are given in Table 1. According to the

Table 1. Textural Properties^a of the Catalysts

catalyst	S_{BET} (m ² g ⁻¹)	S_{DFT} (m ² g ⁻¹)	V_p (cm ³ g ⁻¹)	d_p (nm)
Pt/CO ₂ -C	145.3	118.6	0.5	6.9
Pt/C (com.)	31.9	40.9	0.4	25.5

^aThe BET surface area (S_{BET}), specific surface area (S_{DFT}), total pore volume (V_p), and average pore diameter (d_p) are given.

Brunauer–Emmett–Teller (BET) and quenched solid density functional theory (QSDFT) calculations, the surface area of Pt/CO₂-C is considerably higher than that of the commercial alternative. This is advantageous because this means that the reaction can take place on a larger surface area, increasing the overall activity of the catalyst. At the same time, the total pore volume of Pt/CO₂-C was slightly higher than that of Pt/C, while its average pore size was found to be lower than the benchmark catalyst. Based on the pore-size distribution graphs (Figure S6), Pt/CO₂-C consists mostly of mesopores, while some micropores are also present. In the case of the

commercial sample, mesopores dominate the whole structure, with virtually no micropores detected from the measurement. It has been reported²⁹ that a mesoporous carbon support structure is favored for fuel cell catalysts because mesopores enhance the dispersion and utilization of metal particles, facilitating the reaction, while micropores might trap the nanoparticles and inhibit the reactant accessibility. Therefore, CO₂-C should be pretreated in future works to decrease the amount of micropores and introduce functional groups to improve Pt utilization.³⁰

2.2. Electrochemical Performance. The half-cell tests for the catalysts were performed with the rotating disk electrode (RDE) technique in a 0.1 M HClO₄ solution, and the obtained ORR polarization curves (at 1600 rpm) are shown in Figure 4a. The polarization curves featuring the other rotation speeds can be found in Figure S8.

To compare the activity of the catalysts in-depth, several important electrocatalytic properties are given in Table 2. Considering the half-wave ($E_{1/2}$) and onset (E_{onset}) potentials of the catalysts, it can be stated that the electrocatalytic activity of Pt/CO₂-C is almost the same as that of the benchmark. In the case of the onset potential, its activity even surpasses that of the commercial sample, with a positive potential shift of about 3.5 mV lowering the overpotential for the ORR. Furthermore, the mass and specific activities (MA and SA) for the Pt/CO₂-C catalyst were found to be about 33% and 9% higher (Figure 4b) than those of commercial Pt/C, respectively. This means that, in contrast to the commercial

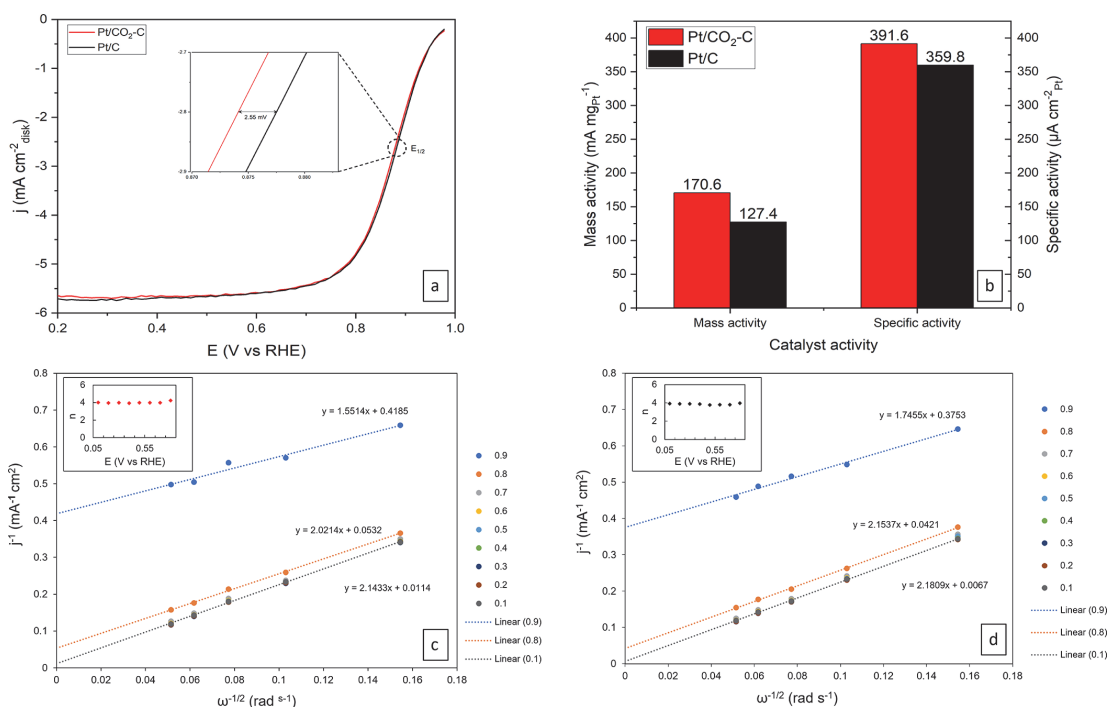


Figure 4. Electrochemical characterization results: (a) ORR polarization curves (anodic sweep) of Pt/CO₂-C and Pt/C (commercial) in O₂-saturated 0.1 M HClO₄ at 20 mV s⁻¹ with a rotation rate of 1600 rpm; (b) comparison of the mass and specific activities for both catalysts; K–L plots for (c) Pt/CO₂-C and (d) commercial Pt/C, with the number of electrons transferred per O₂ molecule (n) in the insets.

Table 2. Electrochemical Properties of the Catalysts

catalyst	E_{onset} (V vs RHE)	$E_{1/2}$ (V vs RHE)	EASA ($\text{m}^2 \text{g}_{\text{Pt}}^{-1}$)	MA at 0.9 V vs RHE ($\text{mA mg}_{\text{Pt}}^{-1}$)	SA at 0.9 V vs RHE ($\mu\text{A cm}^{-2}_{\text{Pt}}$)
Pt/CO ₂ -C	0.990	0.873	43.56	170.6	391.6
Pt/C (com.)	0.987	0.876	35.41	127.4	359.8

catalyst with slightly higher Pt loading, Pt/CO₂-C has a larger electrochemically active surface area (EASA) in which more Pt nanoparticles (per mg and cm² of the catalyst) are taking part in the reaction, thus enhancing Pt utilization and the overall reaction kinetics. This is in good agreement with the established relationship between the nanoparticle size window and the maximum mass activity of the catalyst, which was discussed earlier in the study. For a further comparison, the mass activities reported by other studies are shown in Table 3.

Table 3. Comparison with the Mass Activities of Pt-Based Catalysts from Other Studies

catalyst	Pt loading (in wt %)	MA at 0.9 V vs RHE ($\text{mA mg}_{\text{Pt}}^{-1}$)	reference
Pt/CO ₂ -C	17	170.6	this work
Pt/Vulcan	19.7	180	31
Pt/Vulcan	20	210	32
Pt/N-doped carbon	7.13	108	33
Pt/carbon nanotubes	10	167	34

In addition to the polarization curves, Koutecký–Levich (K–L) and Tafel plots are used to quantify the number of electrons involved in the ORR and to define the rate-determining step for the reaction. Based on the K–L plots (Figure 4c,d), ORR almost exclusively occurs via the four-electron pathway in both catalysts, which is typical for polycrystalline Pt surfaces³⁵ and preferred over the two-electron pathway, in which detrimental H₂O₂ formation is observed.³⁶

In terms of the Tafel slope, a common Pt/C catalyst is known (from the literature) to exhibit slopes at 60 mV dec⁻¹ (at low overpotentials) and 120 mV dec⁻¹ (at high

overpotentials) under acidic conditions, and the deviated slopes (Figure S9) observed in this study can be explained by the fact that the Tafel slopes change based on different factors, such as the exposed facets of Pt crystals,³⁷ the purity of the electrolyte, and the chosen window for linear fitting of the curve.³⁸ At lower overpotentials (>0.88 V vs RHE), both Pt/CO₂-C and commercial Pt/C have slopes at around 70 mV dec⁻¹, which is consistent with the value observed by Marković et al.³⁹ for the Pt(111) facet in 0.1 M HClO₄, and in this case, OH* removal has been suggested as the rate-determining step.^{35,40} However, at higher overpotentials (<0.88 V vs RHE), slope values of about 105 and 130 mV dec⁻¹ are obtained for Pt/CO₂-C and the commercial sample, respectively. These values are more in line with the Pt(110) facet detected in the same study and are close to 120 mV dec⁻¹, which indicates the initial electron transfer to O₂ to be the rate-determining step.⁴¹ The lower slope of Pt/CO₂-C at higher overpotentials denotes a superior catalytic mechanism over the commercial catalyst. However, it must be noted that there is a debate^{37,38,42} on the correct derivation of the rate-determining step for the ORR on Pt and its consistency with the real kinetics of the reaction.

Apart from being active and selective, electrocatalysts must also be stable after long-term exposure to the reactions. To investigate the durability profiles of both catalysts, an accelerated durability test (ADT) of 1000 potential cycles was performed between 0.6 and 1 V versus reversible hydrogen electrode (RHE). After the durability test (Figure 5), it was revealed that the half-wave potential for Pt/CO₂-C experienced a negative shift of around 2.8 mV, while this value was about 3.9 mV for commercial Pt/C. Furthermore, the mass activities (at 0.9 V vs RHE) of Pt/CO₂-C and the benchmark catalyst decreased by 5% and 12%, respectively. The results demonstrate that Pt/CO₂-C is more durable to the reaction conditions. It is important to note that the support material has

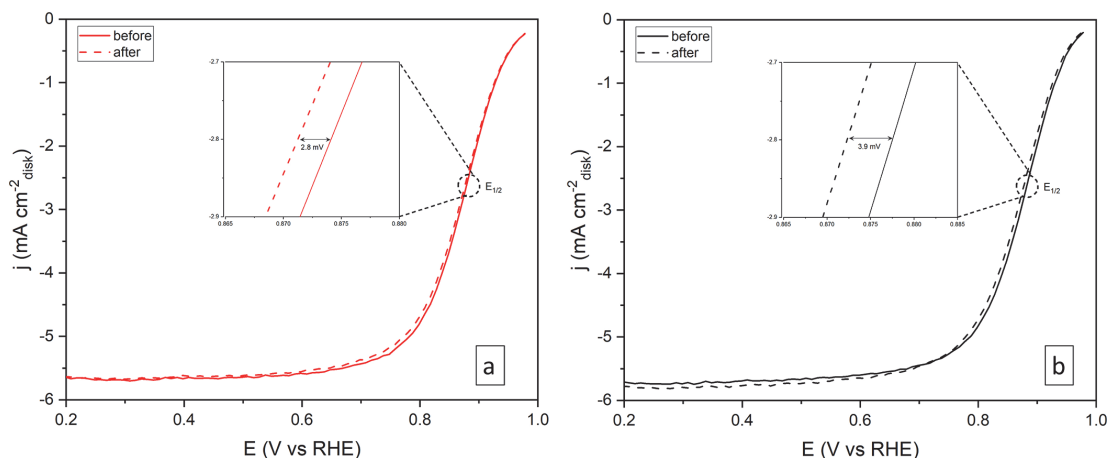


Figure 5. ADT results. ORR polarization curves (anodic sweep) of (a) Pt/CO₂-C and (b) Pt/C (commercial) in O₂-saturated 0.1 M HClO₄ at 20 mV s⁻¹ taken before and after 1000 potential cycles between 0.6 and 1 V versus RHE at 200 mV s⁻¹.

a significant impact on the durability of the final catalyst material.²⁹ Therefore, the outcome confirms the suitability of CO₂-C as a catalyst support in terms of durability.

3. CONCLUSION

A novel platinum catalyst supported with CO₂-derived carbon nanomaterial (in short Pt/CO₂-C) was synthesized with the polyol method. The STEM micrographs of the sample confirmed the uniform distribution of Pt nanoparticles on the carbon support. The size of the metal nanoparticles was found to be around 3.2 nm, which is in the “sweet spot” reported by different research groups in terms of achieving the maximum mass activity for the ORR at a given Pt nanoparticle size. At the same time, N₂ physisorption measurements revealed that the surface area of Pt/CO₂-C is higher than that of commercial Pt/C, which increases the probability of finding active sites for the reaction on the surface. Most importantly, the catalyst exhibited superior electrochemical activity in comparison to the commercial benchmark with its higher onset potential, higher mass and specific activities, larger EASA, lower Tafel slope, and stronger durability while having a very similar half-wave potential and following the advantageous four-electron ORR pathway as the commercial catalyst. The positive findings were linked to the impact of the support nanomaterial on the arrangement of Pt nanoparticles in the catalyst and the overall interaction between the support and catalyst, leading to enhanced catalytic activity. In summary, the sustainable CO₂-derived carbon was shown to be an excellent candidate as a support nanomaterial for Pt-based ORR catalysts used in the cathode of fuel cells. Large-scale production (with up to 0.2 t of CO₂ converted daily⁴³) of carbon nanotubes with a similar process proves that CO₂-C preparation is also scalable. Subsequent research may focus on improvement of the carbon nanomaterial (for instance, pretreating the carbon to increase the number of mesopores and to introduce functional groups as anchoring sites for Pt) as well as fine-tuning of the shape and structure of the Pt nanoparticles for enhanced activity and durability.

4. EXPERIMENTAL SECTION

4.1. Synthesis of CO₂-Derived Carbon. For the synthesis of the CO₂-derived carbon support material, a eutectic mixture of Li₂CO₃–Na₂CO₃–K₂CO₃ was prepared by mixing Li₂CO₃ (99%, from ACU PHARMA and CHEMIE GmbH), K₂CO₃ (99.3% p.a., Lach-Ner), and Na₂CO₃ (99% p.a., Lach-Ner) at a molar ratio of 43.5:31.5:25.0. Next, the carbonate salt mixture was transferred to an alumina crucible, which was placed inside a stainless-steel reactor. After the mixture was melted at 450 °C, capturing of CO₂ was initiated and stainless-steel rods (SS304 from metall24.ee, Estonia) were inserted into the molten salt mixture as the cathode and anode. The electrolysis of CO₂ to produce carbon on the cathode was achieved by applying 4 V to the electrodes and collecting the carbon materials deposited on the cathode. The Faraday efficiency of carbon deposition (calculated by comparing the measured current to the theoretical amount of current required to deposit the resulting carbon) is around 85%. As the final step, the cathode was washed with 5 M HCl (Merck) to remove the solidified salt attached to the deposit, and the produced carbon was dried.

4.2. Synthesis of the Pt/CO₂-C Catalyst. Chloroplatinic acid hydrate (99.9% H₂PtCl₆·H₂O, Aldrich) was used as the Pt source for the catalyst synthesis. First, 0.2 mL of a 1 M NaOH (98%, Aldrich) solution was dropped into 30 mL of ethylene glycol (99%, Lach-Ner) in a small beaker to achieve a pH value of around 11 while mixing with a magnetic stirrer. Then the pH-adjusted ethylene glycol was transferred to a three-neck round-bottomed flask, and 0.2 g of CO₂-C

was added and mixed thoroughly by using a magnetic stirrer for 90 min under a N₂ flow. After 0.105 g (to obtain 20% Pt loading in the final catalyst) of the Pt precursor was diluted with 15 mL of deionized water (Milli-Q) in a measuring cylinder and the resulting solution was poured into the carbon–polyol mix, a reflux apparatus with an oil bath was installed to reflux the mixture for 3 h at a temperature range of 110–130 °C under a N₂ flow. Subsequently, the mixture was cooled and stirred overnight under a N₂ flow. In the end, the catalyst was washed several times with deionized water and dried in an oven at 70 °C for more than 19 h. The commercial Pt/C catalyst (19.8 wt %, TKK) was used as a benchmark and for comparative purposes.

4.3. Electrochemical Characterization. The conventional RDE method with a three-electrode system was used for evaluation of the catalyst activity in the ORR. First, 0.2 cm² glassy carbon electrodes (Goodfellow Cambridge Ltd.) were polished with 1 and 0.3 μm alumina slurries (Buehler) and sonicated for 5 min with isopropyl alcohol (Lachner) followed by sonication with deionized water for 5 min. To prepare the catalyst ink, 4 mg of Pt/CO₂-C, 4 mL of deionized water, 50 μL of isopropyl alcohol (Lachner), and 2 μL of a 5 wt % Nafion (Aldrich) solution were added to a vial and placed in an ultrasonic bath (640 W, Bandelin Sonorex Digiplus DL 510 H) containing cold water to be sonicated for about 40 min. Next, the ink was further sonicated by an ultrasonic homogenizer (Hielscher UP200 St) for around 35 s. Finally, 20 μL of the ink was pipetted onto the glassy carbon electrodes to obtain 0.1 mg cm^{−2} catalyst loading and left to dry at room temperature. For comparison with Pt/CO₂-C, the ink for the commercial Pt/C sample (19.8%, TKK) was prepared and cast onto the electrode with the same recipe.

To attain sufficient cleanliness of the electrochemical cell and its parts, they were soaked in a concentrated HNO₃/H₂SO₄ mix, washed with deionized water and again soaked in a KOH/isopropyl mix followed by further washing and boiling with deionized water. Silver/silver chloride (Ag/AgCl, SI analytics) separated with a Luggin capillary was used as the reference electrode, while a graphite rod in a glass frit was used as the counter electrode for the test. To convert the potentials measured versus Ag/AgCl to potentials versus RHE, calibration was performed in H₂-saturated 0.1 M HClO₄ with a Pt wire as the working electrode, and the following equation was defined: $E_{\text{RHE}} = E_{\text{Ag/AgCl}} + 0.2379 \text{ V}$. All of the potential values shown in the text are given versus RHE and not compensated for *iR* unless stated otherwise.

After the cell was filled with an 0.1 M HClO₄ (Aldrich) electrolyte solution and the working electrode was inserted, the solution was saturated with N₂ and electrochemical cleaning was performed with 200 potential cycles in the ranges of 0.05 V–0.1 V–0.05 V versus RHE at 300 mV s^{−1}. Next, a cyclic voltammogram was taken in the same potential range at a scan rate of 50 mV s^{−1} to estimate the EASA from the H-adsorption region followed by background current measurement again in the same potential range (at a scan rate of 20 mV s^{−1} without rotation) for both catalysts by using a potentiostat (model 1010E, Gamry Instruments) at room temperature. Then the electrolyte was saturated with O₂ (99.999%, Elme Messer AS) and ORR polarization curves were recorded in the same potential range of 0.05 V–0.1 V–0.05 V versus RHE (at a scan rate of 20 mV s^{−1}) at different rotation speeds (400, 900, 1600, 2500, and 3600 rpm) controlled by an OrigaTrod apparatus (OrigaLys ElectroChem SAS). The polarization curves were background-corrected to minimize the capacitive current contribution.

The K–L equation⁴⁴ was utilized to obtain the overall number of electrons transferred per O₂ molecule from the polarization curves of different rotation speeds:

$$\frac{1}{j} = \frac{1}{j_k} + \frac{1}{j_d} = -\frac{1}{nFkc_{\text{O}_2}^b} - \frac{1}{0.62nFD_{\text{O}_2}^{2/3}\nu^{-1/6}\omega^{1/2}c_{\text{O}_2}^b} \quad (1)$$

Here *j* is the measured current density, *j_k* is the kinetic current density, *j_d* is the diffusion-limited current density, *n* is the overall number of electrons transferred per O₂ molecule, *k* is the electron-transfer rate constant, *F* is the Faraday constant (*F* = 96485 C mol^{−1}), *D_{O₂}* is the diffusion coefficient of oxygen (1.93 × 10^{−5} cm² s^{−1} in 0.1 M

HClO_4),³⁹ ν is the kinematic viscosity of the electrolyte ($1.009 \times 10^{-2} \text{ cm}^2 \text{ s}^{-1}$ in 0.1 M HClO_4),³⁹ ω is the angular velocity of the rotating disk ($\omega = 2\pi N$, where N is the linear rotating speed in rpm), and $c_{\text{O}_2}^b$ is the bulk concentration of oxygen ($1.26 \times 10^{-3} \text{ mol L}^{-1}$ in 0.1 M HClO_4).³⁹

The Tafel slope (b) was determined by plotting the overpotential (η) against the logarithm of the current density ($\log j$) for the polarization curve at 1600 rpm and fitting the linear portion of the curve with the Tafel equation:⁴⁴

$$\eta = a + b \log j \quad (2)$$

To calculate the EASA, the hydrogen adsorption charge ($Q_{\text{H-adsorption}}$) was estimated by integrating the H-adsorption area of the cyclic voltammogram, and the following equation was used:

$$\text{EASA}_{\text{Pt,cat}} (\text{m}^2 \text{ g}_{\text{Pt}}^{-1}) = \left[\frac{Q_{\text{H-adsorption}} (\text{C})}{210 \mu\text{C cm}_{\text{Pt}}^{-2} \times L_{\text{Pt}} (\text{m g}_{\text{Pt}} \text{ cm}^{-2}) \times A_{\text{g}} (\text{cm}^2)} \right] \times 10^5 \quad (3)$$

Here, L_{Pt} is the working electrode of the Pt loading and A_{g} is the geometric surface area of the glass carbon electrode. The charge associated with full coverage of clean polycrystalline Pt with a hydrogen monolayer was assumed⁵² to be $210 \mu\text{C cm}^{-2}$ in this equation.

4.4. Physical Characterization. To analyze the surface morphology of the samples, micrographs were obtained by SEM and STEM. The samples were dispersed on copper transmission electron microscopy (TEM) grids with a lacey carbon film. A Spectra 300 (ThermoFisher) S/TEM operated at an acceleration voltage of 300 kV was used to acquire STEM images using the high-angle annular dark field (HAADF) signal, while a JEOL JSM-7500FA microscope, equipped with a cold field-emission gun, was employed for SEM imaging with an acceleration voltage of 15 kV. EDS analysis was performed with a SDD Ultim max 100 (Oxford) detector for SEM and on a Bruker Dual-X setup on the ThermoFisher Spectra 300 microscope.

XRD measurement was performed with a Malvern PANalytical Xpert3 diffractometer by using a Cu K α X-ray source ($\lambda = 0.154 \text{ nm}$) and operating at beam voltage and current values of 45 kV and 40 mA, respectively.

N_2 adsorption–desorption isotherms for both materials were studied by a NOVA 1200e instrument (Quantachrome). The specific surface areas were calculated by the BET method, and the porosity was calculated by QSDFT.

TGA was carried out to obtain thermal characterization of Pt/ CO_2 -C and to confirm the Pt loading of the catalyst by heating the sample in an alumina crucible with a Labsys 2000 (Setaram) thermoanalyzer at a heating rate of 10 K min^{-1} under an air atmosphere.

Raman analysis was performed on a Renishaw Invia microscope using a 514.5 nm excitation source. The spectra were collected with a 20 \times objective (NA = 0.4) and an approximate optical density at the sample surface of several hundreds of kilowatts per square centimeter. The acquisition time was 30 s. Following the treatment of Ferrari et al.,²⁵ the D band was fit with a Lorentzian line shape, while a Breit–Wigner–Fano line shape was used for the G band. The peak height was used to determine the intensities in both cases. Backgrounds were subtracted using a cubic polynomial. The presented results are an average of seven spectra.

■ ASSOCIATED CONTENT

Data Availability Statement

The data generated during this study are available from the corresponding author upon reasonable request.

Supporting Information

The Supporting Information is available free of charge at <https://pubs.acs.org/doi/10.1021/acsnm.3c00208>.

EDS and TGA results, SEM and STEM images of commercial Pt/C, SEM image of stock CO_2 -C, particle size distribution histograms, Raman spectroscopy results, N_2 physisorption study results, ORR polarization curves with different rotation rates, Tafel plots, and a table of Raman characteristics (PDF)

■ AUTHOR INFORMATION

Corresponding Author

Ivar Kruusenberg – National Institute of Chemical Physics and Biophysics, Tallinn 12618, Estonia; orcid.org/0000-0002-8199-9324; Email: ivar.kruusenberg@kbfi.ee

Authors

Erkin Najafli – National Institute of Chemical Physics and Biophysics, Tallinn 12618, Estonia

Sander Ratso – National Institute of Chemical Physics and Biophysics, Tallinn 12618, Estonia

Yurii P. Ivanov – Electron Spectroscopy and Nanoscopy, Italian Institute of Technology, Genova 16163, Italy

Matija Gatalo – Department of Materials Chemistry, National Institute of Chemistry, Ljubljana 1000, Slovenia;

orcid.org/0000-0002-5041-7280

Luka Pavko – Department of Materials Chemistry, National Institute of Chemistry, Ljubljana 1000, Slovenia

Can Rüstü Yörük – Department of Materials and Environmental Technology, Tallinn University of Technology, Tallinn 19086, Estonia

Peter Walke – Department of Materials and Environmental Technology, Tallinn University of Technology, Tallinn 19086, Estonia

Giorgio Divitini – Electron Spectroscopy and Nanoscopy, Italian Institute of Technology, Genova 16163, Italy;

orcid.org/0000-0003-2775-610X

Nejc Hodnik – Department of Materials Chemistry, National Institute of Chemistry, Ljubljana 1000, Slovenia;

orcid.org/0000-0002-7113-9769

Complete contact information is available at: <https://pubs.acs.org/doi/10.1021/acsnm.3c00208>

Notes

The authors declare no competing financial interest.

■ ACKNOWLEDGMENTS

This work was financially supported via Grant PSG312 (“Metal Oxide-based Catalyst Materials from Recycled Li-ion Batteries for Metal-air Battery and Fuel Cell Applications”) by the Estonian Research Council and under ESA Contract 4000134761/21/NL/GLC/my by the European Space Agency and by the National Institute of Chemical Physics and Biophysics. The authors also acknowledge the Electron Microscopy Facility at Istituto Italiano di Tecnologia and Dr. S. Laucello for acquiring SEM images.

■ REFERENCES

- (1) Jiao, K.; Wang, B.; Du, Q.; Wang, Y.; Zhang, G.; Yang, Z.; Deng, H.; Xie, X. Introduction. *Water and Thermal Management of Proton Exchange Membrane Fuel Cells*; Elsevier, 2021; pp 1–23. DOI: 10.1016/B978-0-323-91116-0.00001-8.
- (2) Wang, H.; Li, H.; Yuan, X.-Z. In *PEM Fuel Cell Durability Handbook, Two-Volume Set*; Wang, H., Li, H., Yuan, X.-Z., Eds.; CRC Press, 2019. DOI: 10.1201/9780429108921.

- (3) Bizon, N.; Stan, V. A.; Cormos, A. C. Optimization of the Fuel Cell Renewable Hybrid Power System Using the Control Mode of the Required Load Power on the DC Bus. *Energies (Basel)* **2019**, *12* (10), 1889.
- (4) Wang, X.; Li, Z.; Qu, Y.; Yuan, T.; Wang, W.; Wu, Y.; Li, Y. Review of Metal Catalysts for Oxygen Reduction Reaction: From Nanoscale Engineering to Atomic Design. *Chem.* **2019**, *5* (6), 1486–1511.
- (5) Tan, H.; Li, Y.; Kim, J.; Takeji, T.; Wang, Z.; Xu, X.; Wang, J.; Bando, Y.; Kang, Y. M.; Tang, J.; Yamauchi, Y. Sub-50 Nm Iron-Nitrogen-Doped Hollow Carbon Sphere-Encapsulated Iron Carbide Nanoparticles as Efficient Oxygen Reduction Catalysts. *Advanced Science* **2018**, *5* (7), 1800120.
- (6) Tan, H.; Tang, J.; Kim, J.; Kaneti, Y. V.; Kang, Y. M.; Sugahara, Y.; Yamauchi, Y. Rational Design and Construction of Nanoporous Iron- and Nitrogen-Doped Carbon Electrocatalysts for Oxygen Reduction Reaction. *J. Mater. Chem. A Mater.* **2019**, *7* (4), 1380–1393.
- (7) Cai, Z.; Wang, Z.; Kim, J.; Yamauchi, Y. Hollow Functional Materials Derived from Metal-Organic Frameworks: Synthetic Strategies, Conversion Mechanisms, and Electrochemical Applications. *Adv. Mater.* **2019**, *31* (11), 1804903.
- (8) Suib, S. L. *New and Future Developments in Catalysis*; Elsevier, 2013. DOI: 10.1016/C2010-0-68687-1.
- (9) Li, C.; Tan, H.; Lin, J.; Luo, X.; Wang, S.; You, J.; Kang, Y. M.; Bando, Y.; Yamauchi, Y.; Kim, J. Emerging Pt-Based Electrocatalysts with Highly Open Nanoarchitectures for Boosting Oxygen Reduction Reaction. *Nano Today* **2018**, *21*, 91–105.
- (10) Serp, P.; Machado, B. *Nanostructured Carbon Materials for Catalysis*; Catalysis Series; Royal Society of Chemistry: Cambridge, U.K., 2015. DOI: 10.1039/9781782622567.
- (11) Serp, P.; Figueiredo, J. L. In *Carbon Materials for Catalysis*; Serp, P., Figueiredo, J. L., Eds.; John Wiley & Sons, Inc.: Hoboken, NJ, 2008. DOI: 10.1002/9780470403709.
- (12) Simon, E.; Leandro, B.; Kyoko, M.; Todd, N.; Kiyoto, T. 2006 IPCC Guidelines for National Greenhouse Gas Inventories; IPCC, 2006; Vol. 3. <https://www.ipcc-nggip.iges.or.jp/public/2006gl/index.html> (accessed 2022–09–27).
- (13) Weng, W.; Tang, L.; Xiao, W. Capture and Electro-Splitting of CO₂ in Molten Salts. *Journal of Energy Chemistry* **2019**, *28*, 128–143.
- (14) Lacarbonara, G.; Chini, S.; Ratso, S.; Kruusenberg, I.; Arbizzani, C. A MnOx-Graphitic Carbon Composite from CO₂ for Sustainable Li-Ion Battery Anodes. *Mater. Adv.* **2022**, *3* (18), 7087–7097.
- (15) Rimmel, A. L.; Ratso, S.; Divitini, G.; Danilson, M.; Mikli, V.; Uibu, M.; Aruvali, J.; Kruusenberg, I. Nickel and Nitrogen-Doped Bifunctional ORR and HER Electrocatalysts Derived from CO₂. *ACS Sustainable Chem. Eng.* **2022**, *10* (1), 134–145.
- (16) Nørskov, J. K.; Studt, F.; Abild-Pedersen, F.; Bligaard, T. *Fundamental Concepts in Heterogeneous Catalysis*; John Wiley & Sons, 2014; pp 19–21. DOI: 10.1002/9781118892114.
- (17) Peuckert, M.; Yoneda, T.; Betta, R. A. D.; Boudart, M. Oxygen Reduction on Small Supported Platinum Particles. *J. Electrochem. Soc.* **1986**, *133* (5), 944–947.
- (18) Kinoshita, K. Particle Size Effects for Oxygen Reduction on Highly Dispersed Platinum in Acid Electrolytes. *J. Electrochem. Soc.* **1990**, *137* (3), 845–848.
- (19) Wikander, K.; Ekström, H.; Palmqvist, A. E. C.; Lindbergh, G. On the Influence of Pt Particle Size on the PEMFC Cathode Performance. *Electrochim. Acta* **2007**, *52* (24), 6848–6855.
- (20) Sattler, M. L.; Ross, P. N. The Surface Structure of Pt Crystallites Supported on Carbon Black. *Ultramicroscopy* **1986**, *20* (1–2), 21–28.
- (21) Xu, Z.; Zhang, H.; Zhong, H.; Lu, Q.; Wang, Y.; Su, D. Effect of Particle Size on the Activity and Durability of the Pt/C Electrocatalyst for Proton Exchange Membrane Fuel Cells. *Appl. Catal., B* **2012**, *111–112*, 264–270.
- (22) Sharma, R.; Wang, Y.; Li, F.; Chamier, J.; Andersen, S. M. Particle Size-Controlled Growth of Carbon-Supported Platinum Nanoparticles (Pt/C) through Water-Assisted Polyol Synthesis. *ACS Omega* **2019**, *4* (13), 15711–15720.
- (23) Wagner, F. T.; Lakshmanan, B.; Mathias, M. F. Electrochemistry and the Future of the Automobile. *J. Phys. Chem. Lett.* **2010**, *1*, 2204–2219.
- (24) Guo, S.; Zhang, S.; Sun, S. Tuning Nanoparticle Catalysis for the Oxygen Reduction Reaction. *Angewandte Chemie - International Edition* **2013**, *52* (33), 8526–8544.
- (25) Ferrari, A.; Robertson, J. Interpretation of Raman Spectra of Disordered and Amorphous Carbon. *Phys. Rev. B: Condens Matter Mater. Phys.* **2000**, *61* (20), 14095.
- (26) Hodnik, N.; Romano, L.; Jovanović, P.; Ruiz-Zepeda, F.; Bele, M.; Fabbri, F.; Persano, L.; Camposeo, A.; Pisignano, D. Assembly of Pt Nanoparticles on Graphitized Carbon Nanofibers as Hierarchically Structured Electrodes. *ACS Appl. Nano Mater.* **2020**, *3* (10), 9880–9888.
- (27) Shao, M. In *Electrocatalysis in Fuel Cells*; Shao, M., Ed.; Lecture Notes in Energy; Springer: London, 2013. DOI: 10.1007/978-1-4471-4911-8.
- (28) Wu, J.-B.; Lin, M.-L.; Cong, X.; Liu, H.-N.; Tan, P.-H. Raman Spectroscopy of Graphene-Based Materials and Its Applications in Related Devices. *Chem. Soc. Rev.* **2018**, *47* (5), 1822–1873.
- (29) Lázaro, M.; Calvillo, L.; Celorrio, V.; Pardo, J. I.; Perathoner, S.; Moliner, R. Study and Application of Vulcan XC-72 in Low Temperature Fuel Cells. *Carbon Black: Production, Properties and Uses* **2011**, 1–28.
- (30) Kumar, S. M. S.; Hidayat, N.; Herrero, J. S.; Irusta, S.; Scott, K. Efficient Tuning of the Pt Nano-Particle Mono-Dispersion on Vulcan XC-72R by Selective Pre-Treatment and Electrochemical Evaluation of Hydrogen Oxidation and Oxygen Reduction Reactions. *Int. J. Hydrogen Energy* **2011**, *36* (9), 5453–5465.
- (31) Garsany, Y.; Singer, I. L.; Swider-Lyons, K. E. Impact of Film Drying Procedures on RDE Characterization of Pt/VC Electrocatalysts. *J. Electroanal. Chem.* **2011**, *662* (2), 396–406.
- (32) Garsany, Y.; Baturina, O. A.; Swider-Lyons, K. E.; Kocha, S. S. Experimental Methods for Quantifying the Activity of Platinum Electrocatalysts for the Oxygen Reduction Reaction. *Anal. Chem.* **2010**, *82* (15), 6321–6328.
- (33) Xiang, Z.; Li, W.; Liu, F.; Tan, F.; Han, F.; Wang, X.; Shao, C.; Xu, M.; Liu, W.; Yang, X. Catalyst with a Low Load of Platinum and High Activity for Oxygen Reduction Derived from Strong Adsorption of Pt-N4Moieties on a Carbon Surface. *Electrochem Commun* **2021**, *127*, 107039.
- (34) Liu, J.; Yin, J.; Feng, B.; Xu, T.; Wang, F. Enhanced Electrocatalytic Activity and Stability toward the Oxygen Reduction Reaction with Unprotected Pt Nanoclusters. *Nanomaterials* **2018**, *8* (11), 955.
- (35) Du, C.; Sun, Y.; Shen, T.; Yin, G.; Zhang, J. Applications of RDE and RRDE Methods in Oxygen Reduction Reaction. *Rotating Electrode Methods and Oxygen Reduction Electrocatalysts*; Elsevier, 2014; pp 231–277. DOI: 10.1016/B978-0-444-63278-4.00007-0.
- (36) Mahata, A.; Nair, A. S.; Pathak, B. Recent Advancements in Pt-Nanostructure-Based Electrocatalysts for the Oxygen Reduction Reaction. *Catal. Sci. Technol.* **2019**, *9* (18), 4835–4863.
- (37) Shinagawa, T.; Garcia-Esparza, A. T.; Takanabe, K. Insight on Tafel Slopes from a Microkinetic Analysis of Aqueous Electrocatalysis for Energy Conversion. *Sci. Rep* **2015**, *5* (1), 13801.
- (38) Holewinski, A.; Linic, S. Elementary Mechanisms in Electrocatalysis: Revisiting the ORR Tafel Slope. *J. Electrochem. Soc.* **2012**, *159* (11), H864–H870.
- (39) Marković, N. M.; Gasteiger, H. A.; Grgur, B. N.; Ross, P. N. Oxygen Reduction Reaction on Pt(111): Effects of Bromide. *J. Electroanal. Chem.* **1999**, *467* (1–2), 157–163.
- (40) Hansen, H. A.; Viswanathan, V.; Nørskov, J. K. Unifying Kinetic and Thermodynamic Analysis of 2 e⁻ and 4 e⁻ Reduction of Oxygen on Metal Surfaces. *J. Phys. Chem. C* **2014**, *118*, 6706–6718.
- (41) Chen, W.; Xiang, Q.; Peng, T.; Song, C.; Shang, W.; Deng, T.; Wu, J. Reconsidering the Benchmarking Evaluation of Catalytic

Activity in Oxygen Reduction Reaction. *iScience* **2020**, *23* (10), 101532.

(42) Wang, J. X.; Uribe, F. A.; Springer, T. E.; Zhang, J.; Adzic, R. R. Intrinsic Kinetic Equation for Oxygen Reduction Reaction in Acidic Media: The Double Tafel Slope and Fuel Cell Applications. *Faraday Discuss.* **2009**, *140* (0), 347–362.

(43) Licht, S.; Liu, X.; Licht, G.; Wang, X.; Swesi, A.; Chan, Y. Amplified CO₂ Reduction of Greenhouse Gas Emissions with C₂CNT Carbon Nanotube Composites. *Materials Today Sustainability* **2019**, *6*, 100023.

(44) Bard, A.; Faulkner, L. *Electrochemical Methods: Fundamentals and Applications*, 2nd ed.; John Wiley & Sons, 2001; pp 92–93.

Recommended by ACS

Highly Active Porous Carbon-Supported CoNi Bimetallic Catalysts for Four-Electron Reduction of Oxygen

Changke Shao, Zitian Huang, *et al.*

FEBRUARY 02, 2023

ENERGY & FUELS

READ 

Synthesis of a Hexagonal-Phase Platinum–Lanthanide Alloy as a Durable Fuel-Cell-Cathode Catalyst

Shi-Long Xu, Hai-Wei Liang, *et al.*

NOVEMBER 16, 2022

CHEMISTRY OF MATERIALS

READ 

Two-Dimensional Bimetallic Carbide Boosts Pt toward Oxygen Reduction Reaction

Chunyang He, Juzhou Tao, *et al.*

APRIL 07, 2022

ACS APPLIED ENERGY MATERIALS

READ 

Boosting the Activity of Single-Atom Pt₁/CeO₂ via Co Doping for Low-Temperature Catalytic Oxidation of CO

Qingmei Tao, Long Kuai, *et al.*

JULY 17, 2022

INORGANIC CHEMISTRY

READ 

Get More Suggestions >

Appendix 2

Publication II

Erkin Najafli, Sander Ratso, Yurii P. Ivanov, Matija Gatalo, Luka Pavko, Can Rüstü Yörük, Peter Walke, Giorgio Divitini, Nejc Hodnik, and Ivar Kruusenberg, Sustainable CO₂-Derived Nanoscale Carbon Support to a Platinum Catalyst for Oxygen Reduction Reaction ACS Applied Nano Materials 2023 6 (7), 5772–5780 DOI: 10.1021/acsnm.3c00208.

Functionalization of CO₂-Derived Carbon Support as a Pathway to Enhancing the Oxygen Reduction Reaction Performance of Pt Electrocatalysts

Erkin Najafli, Sander Ratso, Amir Foroozan, Navid Noor, Drew C. Higgins, and Ivar Kruusenberg*



Cite This: *Energy Fuels* 2024, 38, 15601–15610



Read Online

ACCESS |



Metrics & More



Article Recommendations



Supporting Information



ABSTRACT: Proton-exchange membrane fuel cells (PEMFCs) hold promise for clean energy generation, but their commercialization is partially hindered by the sluggish oxygen reduction reaction (ORR) at the cathode, which relies on costly Pt electrocatalysts supported by petroleum-derived carbon. This study investigates a CO₂-derived carbon (CO₂-C) material as a sustainable alternative to petroleum-derived carbon and attempts to enhance the ORR performance of Pt electrocatalyst with the CO₂-C support by pretreatment with hydrogen peroxide (H₂O₂) and potassium hydroxide (KOH) solutions. Based on physical characterization results, both KOH and H₂O₂ pretreatments of CO₂-C increased the Brunauer–Emmett–Teller (BET) surface area and improved the metal–support interaction compared to untreated CO₂-C. Electrochemical characterization revealed superior ORR performance of Pt/H₂O₂-CO₂-C, exhibiting higher mass activity (142.8 mA mg_{Pt}⁻¹) compared to Pt/CO₂-C (102 mA mg_{Pt}⁻¹), while Pt/KOH-CO₂-C showed the highest specific activity (1503.8 μA cm_{Pt}⁻²) among the studied samples. Thus, Pt electrocatalysts with pretreated CO₂-C support are presented as an alternative to conventional Pt/C catalysts toward sustainable and high-performance PEMFCs.

INTRODUCTION

The projections show that climate change can increase the world's total final energy demand in the midcentury by up to 58% (in addition to socioeconomic developments) compared to the present day caused by factors such as an increase in hot season cooling demand due to global warming.¹ Because of major concerns arising from reliance on fossil fuels for global energy demand and its impact on climate change,² clean energy technologies receive considerable interest from the public to fill the growing energy demand gap. In the case of electrochemical devices, fuel cells and batteries have been intensively researched as part of clean energy solutions. Proton-exchange membrane fuel cell (PEMFC) is one of the most technologically mature fuel cell types, and it has several key advantages as it operates in low temperatures with high efficiency and minimal maintenance required while being suitable for portable applications as well.³ Commercialization of PEMFC technologies is hindered due to challenges associated with the sluggish oxygen reduction reaction (ORR) that reduces oxygen to water on the cathode.⁴ The

commercial electrocatalysts for this reaction are commonly prepared by depositing costly and scarce Pt metal nanoparticles on a support material such as carbon black (shortly named Pt/C), which is conventionally produced from petroleum products.^{5,6} Considering the significant cost and CO₂ footprint associated with the production of Pt/C electrocatalysts, the development of sustainably produced electrocatalyst materials with high Pt metal utilization is among the emerging research trends in the field of electrocatalysis.

In previous work, we prepared an electrocatalyst supported by sustainable CO₂-derived carbon (shortly CO₂-C) nano-

Received: May 21, 2024

Revised: July 17, 2024

Accepted: July 31, 2024

Published: August 6, 2024



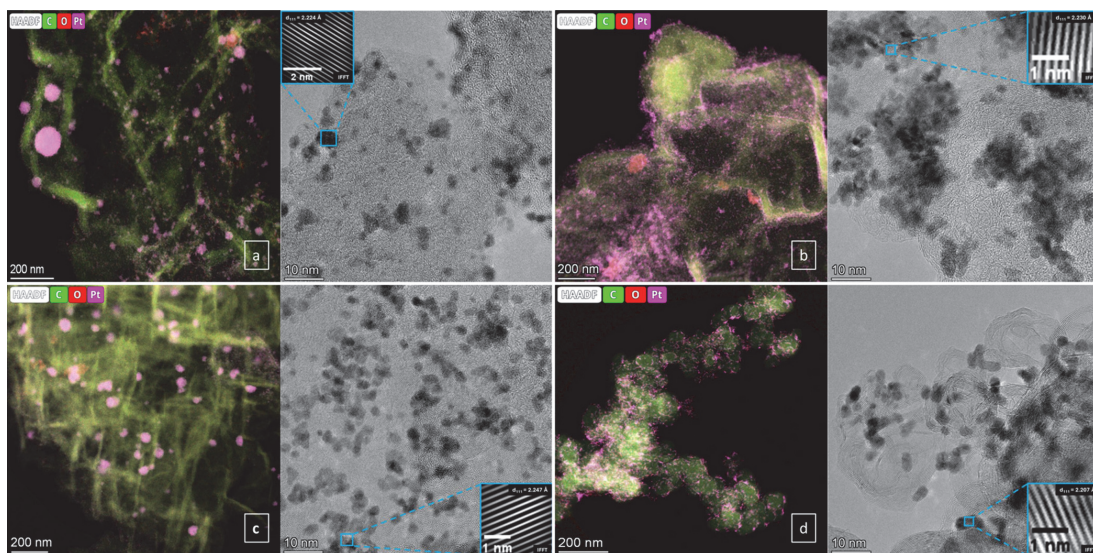


Figure 1. High-angle annular dark-field scanning transmission electron microscopy (HAADF)-STEM (with elemental mapping) and TEM images of (a) Pt/CO₂-C, (b) Pt/H₂O₂-CO₂-C, (c) Pt/KOH-CO₂-C, and (d) commercial Pt/C samples. The insets with HR-TEM images show the inverse fast Fourier transform (IFFT) of the region designated with a blue box.

materials and presented these materials as a promising candidate to replace the conventional petroleum-sourced carbon black.⁷ However, further improvement of this carbon support material is necessary to increase the Pt utilization and overall catalytic performance of the final electrocatalyst, as it has been widely established that the choice of electrocatalyst support materials is crucial to electrocatalyst performance and durability.^{6,8} For instance, the microporous structure of carbon is often associated with lower metal utilization due to poor mass transport, while the macroporous structure decreases the surface area, which can hinder electrical conductivity with increasing resistance.⁹ Apart from the pore size, the surface characteristic of the carbon is another important feature, which determines its suitability as a support for metal nanoparticle catalysts. Liquid-phase functionalization with oxidizing or alkaline solutions is one of the common techniques for nanoengineering the surface chemistry and pore texture of carbon materials.¹⁰ The aim of such pretreatments is to introduce oxygen functional groups to the carbon surface as anchoring points for Pt nanoparticles and to optimize the metal–support interaction (MSI) by increasing the hydrophilicity of the carbon as these functional groups influence the acid–base and redox properties of the carbon material.⁹ Such functional groups include carboxyl (COOH), hydroxyl (COH), and carbonyl (C=O) that interfere with the sp² hybridization in order to increase the number of free electrons to interact with incoming Pt cations.¹¹ Furthermore, while enhanced hydrophilicity makes the carbon structure more accessible to aqueous metal precursors, less acidic groups improve the metal–support interaction, which can lead to higher dispersion and lower sintering of metal nanoparticles.¹²

While we are able to prepare and use CO₂-derived carbon as a Pt electrocatalyst support for ORR, the indirect impact of CO₂-C surface functionalization on the electrocatalytic performance of CO₂-C-supported Pt has not been explored

so far. Thus, it is of great interest to investigate if surface modifications of the CO₂-C support can be used to manipulate the electrocatalyst's activity and durability toward the oxygen reduction reaction.

The purpose of this work is to pretreat CO₂-C with two different solutions (containing hydrogen peroxide and potassium hydroxide) to achieve surface functionalization and to evaluate the impact of both pretreatment methods on the electrocatalytic and physical properties of Pt electrocatalysts supported by functionalized CO₂-C. Although the effect of these solutions on commercially available Vulcan XC-72R was studied before,¹² pretreatment of CO₂-C is conducted for the first time in this study. Based on the evaluations, we find that surface functionalization of the CO₂-C support opens up a new avenue to enhance the ORR performance of Pt electrocatalysts, leading to sustainable and cost-efficient ORR electrocatalyst materials.

RESULTS AND DISCUSSION

Catalyst Preparation and Physical Characterization. A molten eutectic mixture consisting of Li₂CO₃–Na₂CO₃–K₂CO₃ was used as the electrolyte for CO₂ electrolysis to produce amorphous carbon based on a method previously developed by us.^{7,13–15} Next, the carbon was pretreated with two different solutions (containing H₂O₂ and KOH), and Pt was deposited by using the polyol synthesis method to form the electrocatalyst samples. The nomenclature for Pt electrocatalysts prepared in this work is based on abbreviations showing the type of support pretreatment method: Pt/CO₂-C (untreated support), Pt/H₂O₂-CO₂-C (support treated with H₂O₂ solution), and Pt/KOH-CO₂-C (support treated with KOH solution).

Pt loading of each sample was calculated by performing thermogravimetric analysis (TGA). From the TGA result (Figure S1 of the Supporting Information), it was found that

the commercial Pt/C sample contains 20 wt % Pt while the Pt loadings for Pt/CO₂-C, Pt/H₂O₂-CO₂-C, and Pt/KOH-CO₂-C are 35, 31, and 30 wt %, respectively.

Scanning transmission electron microscopy (STEM) and transmission electron micrographs (TEM; Figure 1) were analyzed to compare the physical properties of the catalyst samples. In terms of homogeneous Pt distribution over the carbon support, Pt/KOH-CO₂-C is observed to be the sample with the most homogeneous nanoparticle distribution, followed in order by Pt/H₂O₂-CO₂-C, commercial Pt/C, and Pt/CO₂-C. While the distribution of Pt nanoparticles was homogeneous for CO₂-C-supported samples, STEM micrographs show that the nanoparticle distribution is less uniform compared to that of commercial Pt/C. Thus, upon further observation, certain sites of agglomeration within these samples can be detected, and it is argued that the relative agglomeration was mainly caused by the higher Pt loading of electrocatalysts synthesized in this work in contrast to commercial Pt/C.

To compare the particle size distributions of the electrocatalysts, particle size distribution histograms were plotted (Figure S2 of the Supporting Information). Based on the histograms, the size of the Pt nanoparticles on H₂O₂-CO₂-C support ranges from 2 to 10 nm, while the mean particle size is around 5.7 nm. Compared to the other samples, this is a broader particle size distribution, which is also evident from STEM micrographs. While the mean particle sizes of Pt/KOH-CO₂-C and commercial Pt/C are comparable, the smallest Pt nanoparticles were observed in Pt/CO₂-C electrocatalyst. In our previous work,⁷ the mean Pt nanoparticle size of Pt/CO₂-C (prepared in ethylene glycol solvent with a pH of about 11) was around 3.18 nm, while it was hypothesized that in this work, further increase in the pH of ethylene glycol solution would result in even smaller Pt nanoparticles. The calculated mean particle size of roughly 2.96 nm is in agreement with this hypothesis. The high-resolution transmission electron microscopy (HR-TEM) images of all four samples contained several regions in which lattice fringes were visible (Figure 1, the insets). These regions were chosen to estimate the *d*-spacing values. All regions analyzed showed a *d*-spacing value of around 2.2 Å, which was attributed to (111) plain of Pt ($d_{111} = 2.263 \text{ \AA}$).¹⁶

The Brunauer–Emmett–Teller (BET) and mesopore-specific surface areas of the electrocatalysts (Figure 2) were determined with a N₂ physisorption study. The results indicate

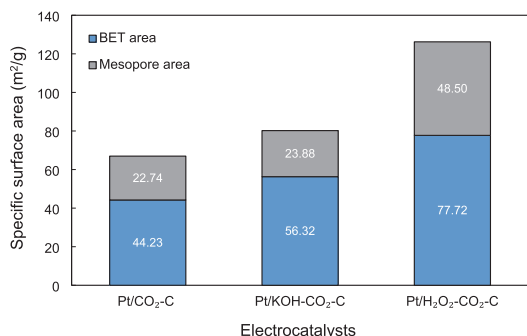


Figure 2. BET and mesopore-specific surface areas of the electrocatalysts synthesized in this work from the N₂ physisorption study.

the changes in the porous structure of the samples caused by different pretreatment methods. When Pt/CO₂ is considered as the baseline, it is observed that both KOH and H₂O₂ pretreatments of the carbon support introduced mesopores to the structure while increasing the BET area. This can be explained by the corrosive influence of KOH and the oxidative influence of H₂O₂ that merges the adjacent micropores, leading to more mesopores as suggested by Kumar et al.¹⁵ While KOH pretreatment of the support caused moderate (from 22.74 to 23.88 m² g⁻¹) enhancement of mesopore-specific area for the electrocatalyst compared to Pt/CO₂-C, H₂O₂ pretreatment was associated with a significant increase of 25.76 m² g⁻¹ from 22.74 to 48.5 m² g⁻¹ in mesopore-specific area of Pt/H₂O₂-CO₂-C which also contributed to a BET-specific area enhancement of 33.49 m² g⁻¹ in contrast to Pt/CO₂-C. However, the merging of micropores was found to be disadvantageous, as they can also enable Pt nanoparticle agglomeration in this space, which was observed from STEM micrographs of CO₂-C-supported samples and specifically for Pt/H₂O₂-CO₂-C (Figure 1b).

As shown in Figure 3, analysis of X-ray diffraction (XRD) patterns reveals that Pt(111) and Pt(002) at 2θ degrees of 40.2

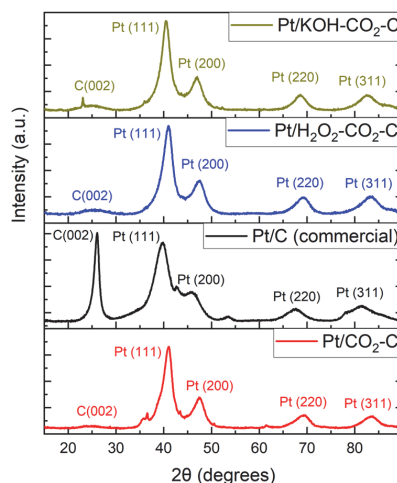


Figure 3. X-ray diffraction patterns of all samples.

and 46.8° are the main Pt reflection planes for all studied samples, while these peaks are more pronounced in the case of samples synthesized in this work. Relatively broader Pt(111) and Pt(311) and less intense Pt(200) peaks of the commercial sample suggest that compared to the commercial Pt/C, CO₂-C-supported electrocatalysts contain Pt nanoparticles with a more crystalline structure. It is also apparent that the sharp peak at 26.1° attributed to the C(002) plane of commercial Pt/C refers to the graphitic nature of the carbon support, whereas the much broader peaks at 25.6° for the other samples are characteristic of the disordered carbon structure. Such characteristics of the CO₂-C supported samples can be considered advantageous, as in weakly adsorbed electrolytes, the Pt(111) plane has been associated¹⁷ with relatively enhanced ORR activity compared to the Pt(100) plane, and defected carbon structure was argued¹¹ to be the preferred attachment points for Pt nanoparticles. These findings further

strengthen the proposition that tuning the structure of the carbon support can indirectly contribute to better ORR performance.

d-spacing values for all samples were also calculated from XRD peaks of Pt(111) to crosscheck with the values obtained from HR-TEM images. As shown in Table 1, *d*-spacing values calculated from XRD patterns agree with the values observed from HR-TEM images.

Table 1. Comparison of D-Spacing Values Obtained from HR-TEM Images and XRD Patterns

catalyst	<i>d</i> ₁₁₁ from HR-TEM (Å)	<i>d</i> ₁₁₁ from XRD (Å)
Pt/CO ₂ -C	2.22	2.20
Pt/KOH-CO ₂ -C	2.24	2.23
Pt/H ₂ O ₂ -CO ₂ -C	2.23	2.22
Pt/C	2.20	2.25

Figure 4 depicts the X-ray photoelectron spectroscopy (XPS) spectrum of Pt 4f_{7/2} and Pt 4f_{5/2} regions (the full spectrum is shown in Figure S5 of the Supporting Information) obtained for the electrocatalysts studied in this work. It has been reported that a positive shift in the binding energy of Pt 4f core levels from the XPS study is linked to electronic effects between Pt and the carbon support.¹⁸ Depending on the electronic properties of the support material, charge transfer occurs between the Pt nanoparticle and the support to reach the equilibrium of corresponding Fermi levels.¹⁸ While the Pt 4f_{7/2} peak for all electrocatalysts synthesized in this work is located at higher binding energies in contrast to commercial Pt/C, the largest positive shift is observed for the Pt/KOH-CO₂-C sample, followed by Pt/H₂O₂-CO₂-C and Pt/CO₂-C, respectively (Figure 4). Such positive shifts originate from the electron-withdrawing effect of carbon support, which causes electron transfer from Pt to carbon that in turn modifies the d-band structure of the electrocatalyst, weakens the adsorption energy of O-containing species, and improves ORR activity and durability due to optimized metal-support interaction.^{18–20} Thus, from a metal-support interaction point of view, pretreatment of the CO₂-C with KOH and H₂O₂ solutions was found to be advantageous, as this implies improved ORR performance for Pt nanocatalysts with these support materials.

Apart from the metal-support interaction, the aim of the pretreatment was also to introduce oxygen functional groups to the surface of the carbon support. This can be evaluated by extracting the atomic concentration of elements on the carbon surface from the XPS survey, as shown in Table 2. According

Table 2. Surface Atomic Concentrations of all Samples Determined from the XPS Spectrum

sample	C (atom %)	O (atom %)	Pt (atom %)	Cu (atom %)
Pt/CO ₂ -C	84.8	9.9	1.9	3.4
Pt/H ₂ O ₂ -CO ₂ -C	82.5	13.4	1.7	2.4
Pt/KOH-CO ₂ -C	82.5	12.5	2.6	2.4
Pt/C (comm.)	92.4	6.4	1.2	n/a

to the table, the concentration of oxygen components on the surface of the CO₂-C-supported electrocatalysts is higher than that of commercial Pt/C, implying successful functionalization. In terms of the atomic percentage of oxygen, the following relationship was revealed, suggesting peroxide pretreatment as the most efficient route to introduce oxygen functional groups: Pt/H₂O₂-CO₂-C > Pt/KOH-CO₂-C > Pt/CO₂-C → Pt/C.

To identify the type of oxygen groups, the relative area for each group was deconvoluted C 1s peaks from the XPS study, which is given in Table 3. The results demonstrate that

Table 3. Assignments, Positions, and Relative Area of C 1s Peaks of all Samples Determined from the XPS Spectrum (Binding Energies at the Bottom)

sample	C-OH, C-O-C (%)	C=O (%)	O-C=O (%)
Pt/CO ₂ -C	10.3	5.4	4
Pt/H ₂ O ₂ -CO ₂ -C	11.6	6.6	5.1
Pt/KOH-CO ₂ -C	11.3	6.2	5.5
Pt/C (comm.)	10.2	1.4	4.3
binding energy (eV)	286.3	287.7	288.9

hydroxyl and ether groups are dominant for all samples, followed by carbonyl and ester groups for CO₂-C-supported electrocatalysts. Compared to Pt/CO₂-C, an increase in the amount of all oxygen-containing groups was observed for both

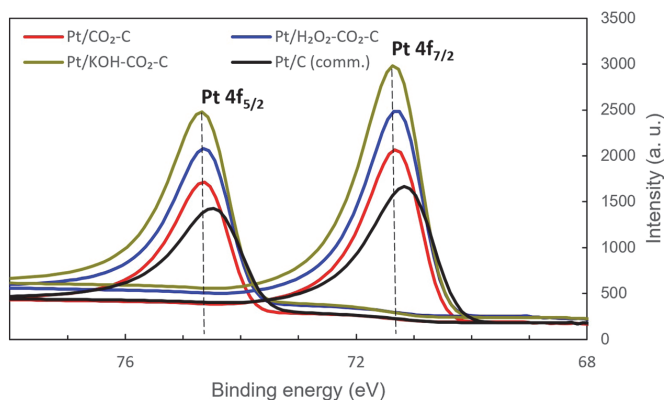


Figure 4. XPS spectrum of Pt 4f_{7/2} and Pt 4f_{5/2} regions for all samples.

Pt/H₂O₂-CO₂-C and Pt/KOH-CO₂-C samples, further confirming the introduction of oxygen groups via functionalization. While peroxide pretreatment was associated with providing slightly more C-OH, C-O-C, and C=O species than KOH pretreatment, the amount of O-C=O species was somewhat higher in the case of KOH pretreatment. As reported in several studies,^{21–23} oxygen functionalization of carbon-based supports was found to improve the electrocatalytic activity toward ORR via disruption of the carbon sp² network and charge delocalization due to high electronegativity of oxygen that leads to enhanced adsorption of ORR intermediates. It must also be noted that the presence of certain oxygen functional groups was linked to enhanced durability for carbon-supported Pt electrocatalysts.²⁴ Hence, the XPS results are consistent with these findings and hint at an improved ORR performance for pretreated samples.

Electrochemical Performance. In order to assess the electrochemical performance of the synthesized samples, the rotating disk electrode (RDE) technique was used to extract the ORR polarization curves at different rotation rates (Figure S3 of the Supporting Information). Based on the ORR polarization curve recorded at 1600 rpm and in 0.1 M HClO₄ (Figure 5), certain metrics that are useful to compare the electrocatalytic activity of the samples are tabulated in Table 4.

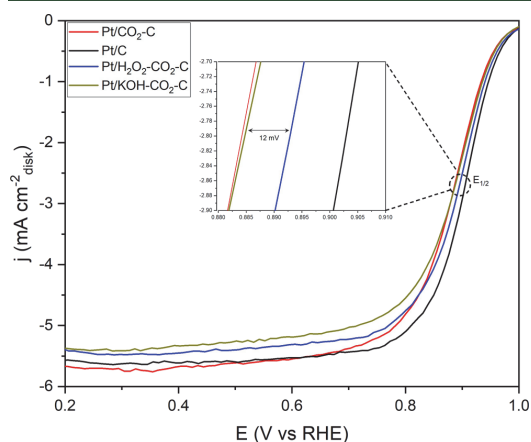


Figure 5. ORR polarization curves (anodic sweep) of all samples in an anodic sweep of 1 M HClO₄ in O₂-saturated 0.1 M HClO₄ at 20 mV s⁻¹ with a rotation rate of 1600 rpm.

The electrochemically active surface area (EASA) of the samples was calculated by using CO stripping curves (Figure 6). The current peaks in the curve indicate CO^{ads} oxidation potential, while the area of the peaks can be used to quantify the density of active sites for CO^{ads}.²⁵ Considering that open facet and defect sites of Pt-based nanocatalysts are more chemically active for CO^{ads} oxidation compared to compact

facets, A (higher E^{ads}) and A* (lower E^{ads}) peaks shown in CO stripping curves can be linked to compact and open facets of Pt/C electrocatalyst.²⁶ With the same approach, the CO₂-C supported samples (B peak) have a lower barrier for CO^{ads} oxidation. However, compared with the commercial sample, the areas below the peak for CO₂-C-supported samples are much smaller than the commercial sample, suggesting a limited number of active sites for CO^{ads}. It is noted that all of the CO₂-C-supported samples had a much smaller EASA (ranging from 8.7 to 13.4 m² g_{Pt}⁻¹) compared to the commercial Pt/C (52.7 m² g_{Pt}⁻¹). This can be explained by the agglomeration of Pt nanoparticles that were detected in STEM micrographs for these samples, which inhibit the CO adsorption to the Pt atoms situated in the core of agglomeration sites and thus diminish the charge associated with CO oxidation from the Pt surface.

At the same time, the gap between the commercial Pt/C and CO₂-C-supported electrocatalysts is less striking, in terms of the calculated mass activities. When considering the mass and specific activities (shortly MA and SA) of samples with pretreated support, in contrast to samples with untreated support, it is found that there is a significant increase in both MA and SA when CO₂-C has been pretreated. While Pt/H₂O₂-CO₂-C exhibits much higher MA than both Pt/CO₂-C and Pt/KOH-CO₂-C, in terms of SA, Pt/KOH-CO₂-C was found to be the most active electrocatalyst, even exceeding the values calculated for commercial Pt/C. This is an expected trend as low-coordination Pt sites (i.e., edge sites, defects, steps) have lower specific activity, and higher-coordination Pt sites (i.e., terraces) have higher specific activity. Larger particles have a higher proportion of terrace (high-coordination Pt) sites exposed versus steps/edges due to their geometry, leading to higher SA values for all CO₂-C-supported electrocatalysts.²⁷ In Table 5, the specific activity of the samples synthesized in this work is compared with the results obtained in other studies.

Cyclic voltammograms (CV) of all samples are shown in Figure 7. In a typical CV, three distinctive regions are of interest for electrochemical characterization: hydrogen underpotential deposition region (hydrogen adsorption and desorption, yellow region), double-layer region (clear region), and oxygen region (OH⁻ ion adsorption and oxide formation/reduction, region higher than 0.6 V vs RHE).²⁸ The peaks A1/A1* and A2/A2* shown on the curves are due to H⁺ desorption/adsorption from compact (111) and open (200) facets, respectively.²⁵ At the same time, the adsorption and desorption of oxygen species on the Pt surface are represented by the E_O^{ads} and E_O^{des} peaks, respectively. Compared to commercial Pt/C, CO₂-C-supported samples have smeared peaks in the HUPD region, indicating higher affinity for H⁺ adsorption and desorption. However, all samples have very similar E_O^{des} peaks, which suggests a similar energy barrier for oxygen desorption. This agrees well with the previous finding that the onset potentials of all electrocatalysts for ORR were

Table 4. Electrocatalytic Activity Metrics for all Samples

sample	EASA _{CO-stripping} (m ² g _{Pt} ⁻¹)	MA at 0.9 V vs RHE (mA mg _{Pt} ⁻¹)	SA at 0.9 V vs RHE (μA cm _{Pt} ⁻²)	E _{onset} (V vs RHE)	E _{1/2} (V vs RHE)
Pt/CO ₂ -C	13.4	102.0	759.9	1.0	0.88
Pt/H ₂ O ₂ -CO ₂ -C	13.2	142.8	1076.4	1.01	0.89
Pt/KOH-CO ₂ -C	8.7	131.1	1503.8	0.99	0.88
Pt/C	52.7	287.7	545.8	1.0	0.90

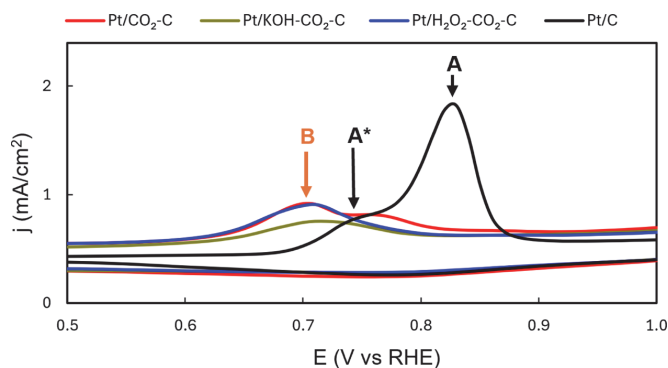


Figure 6. CO stripping curves of all samples in N_2 -saturated 0.1 M $HClO_4$ at 20 mV s^{-1} .

Table 5. Comparison with Specific Activities of Pt-Based Catalysts from Other Studies

catalyst	SA at 0.9 V vs RHE ($\mu\text{A cm}_{Pt}^{-2}$)	refs
Pt/ CO_2 -C	759.9	this work
Pt/ KOH - CO_2 -C	1503.8	this work
Pt/ H_2O_2 - CO_2 -C	1076.4	this work
Pt/Vulcan	511	29
Pt/Vulcan	347	30
Pt/C	400	31
PtNi ₃ /C	1400	32

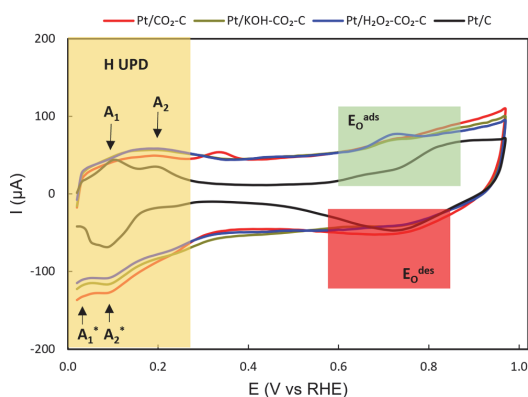


Figure 7. Cyclic voltammetry curves of all samples in N_2 -saturated 0.1 M $HClO_4$ at 50 mV s^{-1} .

almost identical. Furthermore, a thicker double layer of CO_2 -C-supported samples denotes more hydroxide formation compared with the commercial Pt/C electrocatalyst. Less intense $E_{O_{ads}}$ peaks of CO_2 -C-supported samples at a lower potential are another important point that correlates with the results of XPS characterization and shows weakened adsorption energy for O-containing species.

Another important metric of electrocatalytic activity, the number of electrons transferred during the reaction, can be elucidated from Koutecký–Levich (K–L) plots prepared from ORR polarization curves of different rotation rates. According to the K–L plots (Figure S4 of the Supporting Information), the four-electron pathway for ORR is observed in the diffusion-limited current region for all electrocatalysts, which is favored

over the two-electron pathway for fuel cell application due to higher fuel cell efficiency and the absence of detrimental H_2O_2 formation that can degrade the electrocatalyst.³³

The durability of the catalysts was investigated by performing an accelerated durability test (ADT) of 1000 potential cycles between 0.6 and 1 V vs RHE in O_2 -saturated 0.1 M $HClO_4$ at 100 mV s^{-1} . The influence of ADT was quantified by CO stripping measurements before and after the potential cycles (Figure 8, top right) to calculate the loss of EASA after ADT for each electrocatalyst. The highest EASA loss percentage (38.8%) was observed in commercial Pt/C, followed by Pt/ KOH - CO_2 -C (20%), Pt/ H_2O_2 - CO_2 -C (19.6%), and Pt/ CO_2 -C (4.5%), respectively. While Pt supported with untreated CO_2 -C was found to be the most durable to reaction conditions in terms of minimal loss of electrochemically active surface area, the durability of electrocatalysts with pretreated supports was comparable and superior compared to the commercial Pt/C. This is expected as both pretreatment methods were associated with an agglomeration of Pt nanoparticles, which makes the EASA more prone to degradation over longer periods. At the same time, the superior durability of both H_2O_2 - CO_2 - and KOH - CO_2 -C-supported electrocatalysts compared to the commercial Pt/C can be explained by the optimized metal–support interaction and the presence of certain oxygen functional groups, as proposed earlier in the discussion of XPS results.

Furthermore, a comparison of CVs and ORR polarization curves (Figure 8, top left and bottom, respectively) before and after ADT provides additional insights into the performance of samples during the durability test. In the case of the CVs, a reduction in the intensity of the Pt oxidation peak (at around 0.8 V vs RHE) associated with the formation and adsorption of OH_{ads} is observed for samples synthesized in this work.³⁴ This can be attributed to the fact that CV was recorded after performing CO stripping, and a trace amount of CO was left on the Pt surface inhibiting OH_{ads} adsorption. Besides that for all samples including the commercial Pt/C, H^+ adsorption and desorption in the HUPD region peaks became less pronounced after ADT, as there was a drop in EASA values, which was discussed earlier. Although the difference in ORR polarization curves is minor for all samples, a slight fall in diffusion-limited current density is visible for Pt/ CO_2 -C and Pt/ KOH - CO_2 -C, while it stayed the same for both Pt/ H_2O_2 - CO_2 -C and commercial Pt/C. Nevertheless, the ORR performance of all samples can be considered unchanged after ADT, indicating

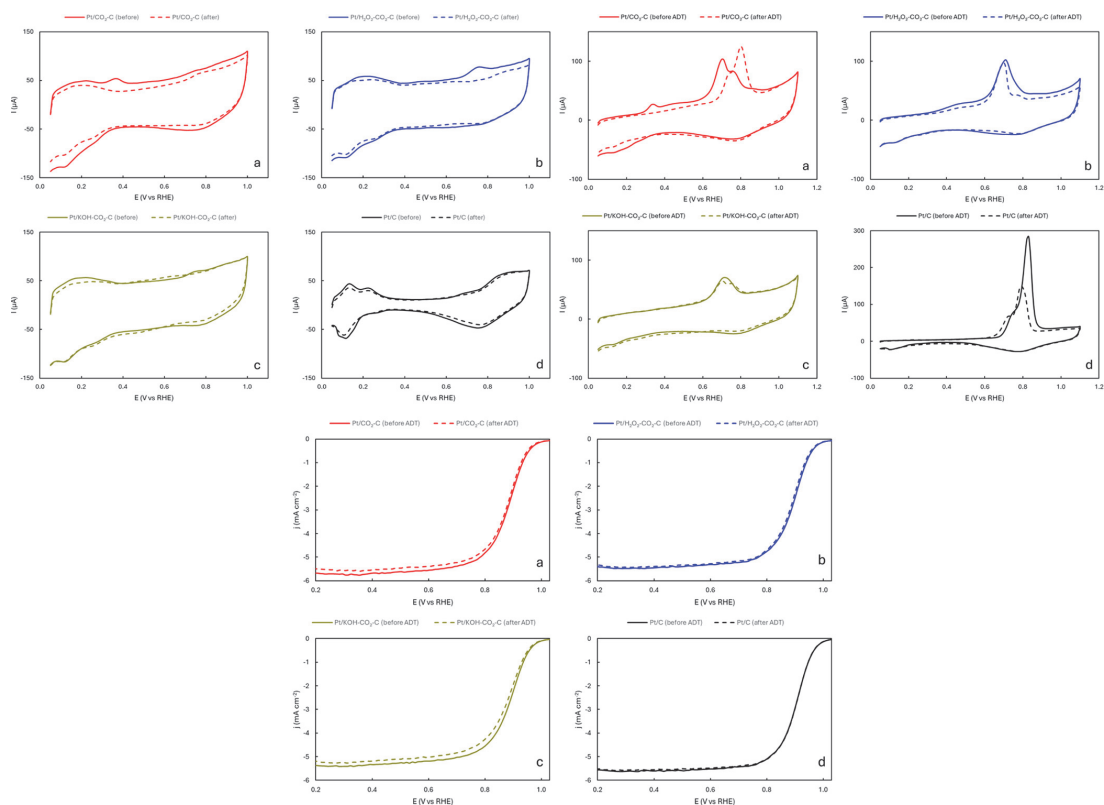


Figure 8. Top left: Cyclic voltammetry curves (before and after ADT) of (a) Pt/CO₂-C, (b) Pt/H₂O₂-CO₂-C, (c) Pt/KOH-CO₂-C, and (d) commercial Pt/C in N₂-saturated 0.1 M HClO₄ at 50 mV s⁻¹; top right: CO stripping curves (before and after ADT) of (a) Pt/CO₂-C, (b) Pt/H₂O₂-CO₂-C, (c) Pt/KOH-CO₂-C, and (d) commercial Pt/C in N₂-saturated 0.1 M HClO₄ at 20 mV s⁻¹; bottom: ORR polarization curves (before and after ADT) of (a) Pt/CO₂-C, (b) Pt/H₂O₂-CO₂-C, (c) Pt/KOH-CO₂-C, and (d) commercial Pt/C in O₂-saturated 0.1 M HClO₄ at 20 mV s⁻¹ with a rotation rate of 1600 rpm.

optimal durability in laboratory-scale durability testing conditions.

EXPERIMENTAL SECTION

Synthesis of CO₂-Derived Carbon. In order to synthesize a carbon support material from CO₂ reduction, an eutectic mixture of Li₂CO₃-Na₂CO₃-K₂CO₃ was prepared by mixing Li₂CO₃, Na₂CO₃, and K₂CO₃ (the molar ratio was 43.5:31.5:25.0). The lithium carbonate was obtained from ACU PHARMA and CHEMIE and had a purity of 99%, while the potassium carbonate and sodium carbonate were acquired from Lach-Ner and had purities of 99.3 and 99% respectively. Subsequently, the carbonate salt mixture was transferred to an alumina crucible, which was then placed inside a stainless steel reactor. Upon heating the mixture to 450 °C, the capture of CO₂ was started. Next, stainless steel rods (SS304 from metall24.ee in Estonia) were placed into the molten salt mixture, serving as the cathode and anode. By application of a voltage of 4 V to the electrodes, electrolysis of CO₂ was initiated, resulting in the deposition of carbon on the cathode with a Faraday efficiency of around 85%. Finally, the cathode was subjected to a washing step using 5 M HCl (Merck) to eliminate any solidified salt residues attached to the carbon deposit and to collect the prepared carbon material after drying.

Pretreatment of CO₂-Derived Carbon. Prior to pretreatment, the synthesis flask was soaked overnight in a concentrated HNO₃/H₂SO₄ (65% from Honeywell and 96% from Lach-Ner, respectively)

mix and washed with deionized water (Milli-Q) to avoid impurities. The pretreatment was performed in aqueous solutions of 10% H₂O₂ prepared from 30% H₂O₂ (Lach-Ner) and 0.2 M KOH prepared from KOH flakes (92%, Lach-Ner). In the case of hydrogen peroxide treatment, 0.4 g of CO₂-C was dispersed in 400 mL of 10% H₂O₂ solution, while for potassium hydroxide treatment, 0.3 g of CO₂-C was dispersed in 300 mL of 0.2 M KOH solution. Both mixtures were refluxed at 110 °C for 16 h and washed by a continuous flow of deionized water on a nylon membrane filter (with a pore size of 0.22 μm from Foxx Life Sciences). Pretreated carbon materials were dried in an oven at 70 °C for 17 h.

Synthesis of Electrocatalysts. The flask for electrocatalyst synthesis was also cleaned with a concentrated acid mix, as mentioned above. First, the pH level of 30 mL of ethylene glycol (99%, Lach-Ner) was adjusted to 12 in a small beaker by adding 0.5 mL of 1 M NaOH solution prepared from NaOH pellets (98%, Aldrich) and mixing with a magnetic stirrer. Next, 0.2 g of pretreated carbon was dispersed in pH-adjusted ethylene glycol in a three-neck round-bottom flask and mixed with a magnetic stirrer for 90 min under N₂ flow. To prepare an aqueous solution of Pt precursor (H₂PtCl₆·xH₂O, 99.9% from Aldrich), 0.105 g of chloroplatinic acid hydrate was diluted with 15 mL of deionized water in a measuring cylinder and added into the carbon-ethylene glycol mix. Then, the synthesis was carried out by refluxing the mixture in an oil bath for 3 h at 110 °C with N₂ flow. After cooling down, the flask was covered with aluminum foil, and the catalyst solution was stirred overnight under

N₂ flow. Finally, the material was washed with a continuous flow of deionized water and then with acetone (99.5% from Aldrich) on a nylon membrane filter (with a pore size of 0.22 μm from Foxx Life Sciences), followed by a drying step in an oven at 70 °C for 17 h.

Electrochemical Characterization. The electrocatalytic activity of the electrocatalysts was screened with a rotating disk electrode (RDE) method. A glassy carbon electrode (Goodfellow Cambridge Ltd.) with a geometric surface area of 0.2 cm² was used as the working electrode. Prior to use, glassy carbon electrodes were polished with alumina slurries of 1 and 0.3 μm (from Buehler), sonicated in ethanol (Bernier) for 5 min, and then further sonicated in deionized water for 5 min. The catalyst ink for all samples was prepared by dispersing 4 mg of catalyst material in 4 mL of deionized water, followed by adding 50 μL of isopropyl alcohol (99.99% from Lach-Ner) and 2 μL of Nafion solution (5 wt % in lower aliphatic alcohols and water (15–20%) from Aldrich). The ink was sonicated in an ultrasonic bath (640W, Bandelin Sonorex Digipuls DL 510 H) containing cold water for 30 min. As the final step, 20 μL (to obtain 0.1 mg cm⁻² catalyst loading) of the ink was drop-cast onto the glassy carbon electrode by pipet and dried in an incubator (IL10 from VWR) at 50 °C. As a benchmark, a commercial Pt/C (19.8%) catalyst was purchased from Tanaka Kikinzo Kogyo K.K. (TKK) and used for comparison using the same ink recipe.

To avoid contamination and impurities, the electrochemical cell and its parts were soaked overnight in a concentrated HNO₃/H₂SO₄ mix, rinsed with deionized water, boiled in deionized water for 1 h, and rinsed again. For the three-electrode setup, a HydroFlex (Gaskatel) reversible hydrogen electrode (RHE) in a Lugin capillary was used as the reference electrode, while a graphite rod in a glass frit was used to complete the circuit as a counter electrode. Thus, the reported potential values in this study are against reversible hydrogen electrodes in all cases.

First, the electrodes were inserted into 0.1 M HClO₄ (Aldrich) electrolyte solution in the cell, and the solution was purged with N₂ (99.999%, Elme Messer) flow. This was followed by electrochemical cleaning of the electrocatalyst surface with 50 potential cycles between 0.05 and 1.1 V vs RHE at 200 mV s⁻¹ by using a potentiostat (Model 1010E, Gamry Instruments). Next, CO stripping measurement was performed to calculate the EASA by saturating the solution with CO flow for 1 min (98%, Elme Messer) while holding the potential at 0.05 V vs RHE, then purging with N₂ flow for 10 min to remove excess CO from the solution and last recording the CO oxidation curve by scanning from 0.05 to 1.1 V vs RHE at 20 mV s⁻¹. To quantify the contribution of capacitive currents, a background current profile was taken between 0.05 and 1.03 V vs RHE at 20 mV s⁻¹ in the N₂ atmosphere while rotating the working electrode at 1600 rpm with OrigaTrod apparatus (OrigaLys ElectroChem SAS). Prior to the measurement of ORR polarization curves, the solution was purged with O₂ (99.999%, Elme Messer), and the uncompensated resistance value was determined by performing electrochemical impedance spectroscopy (EIS) at open circuit voltage (OCV) in the 10,000–10 Hz range (10 points per decade) with a potential amplitude of 10 mV. Next, ORR polarization curves were recorded between 0.05 and 1.03 V vs RHE at 20 mV s⁻¹ with different rotation speeds (400, 900, 1600, 2500, and 3600 rpm). In order to understand the degradation profile of the electrocatalysts, an accelerated durability test (ADT) with 1000 potential cycles between 0.6 and 1 V versus RHE was carried out at 100 mV s⁻¹. As the final step, the CO stripping curve and ORR polarization curve (at 1600 rpm) were recorded after ADT in the same conditions as before for comparison. The polarization curves were background- and *iR*-corrected postcyclic voltammetry to minimize the effect of capacitive currents and ohmic losses of the system.³⁵

The number of transferred electrons per O₂ molecule and the kinetic current (to determine the mass and specific activities) was calculated using the Koutecký–Levich equation:³⁶

$$\frac{1}{j} = \frac{1}{j_k} + \frac{1}{j_d} = -\frac{1}{nFk_c^b} - \frac{1}{0.62nFD_{O_2}^{2/3}\nu^{-1/6}\omega^{1/2}c_{O_2}^b}$$

Here *j* is the measured current density, *j_k* is the kinetic current density, *j_d* is the diffusion-limited current density (calculated at 0.3 V vs RHE in this study), *n* is the overall number of electrons transferred per O₂ molecule, *k* is the electron transfer rate constant, *F* is the Faraday constant (*F* = 96,485 C mol⁻¹), *D_{O₂}* is the diffusion coefficient of oxygen (1.93 × 10⁻⁵ cm² s⁻¹ in 0.1 M HClO₄³⁷), *ν* is the kinematic viscosity of the electrolyte (1.009 × 10⁻² cm² s⁻¹ in 0.1 M HClO₄), *ω* is the angular velocity of the rotating disk (*ω* = 2π*N*, *N* is the linear rotating speed in rpm), and *C_{O₂}* is the bulk concentration of oxygen (1.26 × 10⁻³ mol L⁻¹ in 0.1 M HClO₄).

The mass and specific activities were found by normalizing the kinetic current at 0.9 V vs RHE by the Pt loading on the electrode (mg_{Pt-disk}⁻¹) and Pt active surface area values (cm_{Pt-active}⁻²), respectively.

ORR polarization curves at 1600 rpm were used to estimate the onset and half-wave potentials. Onset potential (*E_{onset}*) was defined as the potential recorded at a current density of -0.1 mA cm⁻². The half-wave potential (*E_{1/2}*) was estimated as the potential recorded at half of the diffusion-limited current density.

To calculate the electrochemically active surface area (EASA), the CO oxidation charge (*Q_{CO-oxidation}*) was estimated by integrating the CO oxidation area of the cyclic voltammogram, and the following equation was used:

$$\begin{aligned} \text{EASA}_{\text{Pt,cat}} (\text{m}^2 \text{g}_{\text{Pt}}^{-1}) \\ = \left[\frac{Q_{\text{H-adsorption}}(\text{C})}{420 \mu\text{C cm}_{\text{Pt}}^{-2} L_{\text{Pt}}(\text{mg}_{\text{Pt}} \text{cm}^{-2}) A_g(\text{cm}^2)} \right] 10^5 \end{aligned}$$

Here *L_{Pt}* is the working electrode Pt loading, and *A_g* is the geometric surface area of the glass carbon electrode. The charge associated with the coverage of the Pt surface with the CO monolayer was assumed to be 420 μC cm⁻² in this equation.³⁸

Physical Characterization. Scanning electron microscopy (SEM) and scanning transmission electron microscopy (STEM) techniques were used to acquire micrographs of the samples for morphology analysis. High-resolution transmission electron microscopy (HR-TEM), high-angle annular dark-field scanning transmission electron microscopy (HAADF-STEM) imaging, and energy dispersive spectroscopy (EDS) mapping were performed using a Thermo Scientific Talos 200X operated at 200 kV while scanning electron microscopy imaging was performed using a Thermo Scientific Quattro ESEM. Image analysis and processing were done via ImageJ software (version 1.54g). Fast Fourier transform (FFT) was used to extract the spatial frequencies of the lattice fringes. After noise reduction was performed on the FFT image and followed by inverse FFT (IFFT), the *d*-spacings were calculated via line profile analysis. The *d*-spacing values were then compared to reference values associated with the corresponding plains of platinum from the Crystallography Open Database (COD: 1011113).¹⁶

X-ray diffraction (XRD) measurement was performed with a Malvern PANalytical Xpert3 by using a Cu Kα X-ray source (*λ* = 0.154 nm) and operating at the beam voltage and current values of 45 kV and 40 mA, respectively. *d*-spacing was calculated by using the Bragg's law:

$$\lambda = 2d \sin(\theta)$$

where *λ* is the wavelength of the X-ray beam (0.154 nm), *d* is the interplanar spacing or *d*-spacing, and *θ* is the diffraction angle.

The XPS analyses were carried out with a Kratos AXIS Supra X-ray photoelectron spectrometer using a monochromatic Al Kα source (15 mA, 15 kV) to probe the surface chemistry of the samples. X-ray photoelectron spectroscopy (XPS) can detect all elements except hydrogen and helium, probes the surface of the sample to a depth of 7–10 nm, and has detection limits ranging from 0.1 to 0.5 atom % depending on the element. The instrument work function was calibrated to give a binding energy (BE) of 83.96 eV for the Au 4f_{7/2} line for metallic gold, and the spectrometer dispersion was adjusted to give a BE of 932.62 eV for the Cu 2p_{3/2} line of metallic copper. The

Kratos charge neutralizer system was used on all specimens. Survey scan analyses were carried out with an analysis area of $300\ \mu\text{m} \times 700\ \mu\text{m}$ and a pass energy of 160 eV. High-resolution analyses were carried out with an analysis area of $300\ \mu\text{m} \times 700\ \mu\text{m}$ and a pass energy of 20 eV. Spectra have been charge-corrected to the main line of the carbon 1s spectrum (adventitious carbon) set to 284.8 eV. Spectra were analyzed using CasaXPS software (version 2.3.23).

N_2 adsorption–desorption isotherms for both materials were studied by a NOVA 1200e instrument (Quantachrome). Specific surface areas were calculated by the Brunauer–Emmett–Teller (BET) method and porosity by quenched solid density functional theory (QSDFT). Mesopore-specific surface areas were found by subtracting t-plot-specific micropore surface area from total BET surface area as reported in another study.³⁹

Thermogravimetric analysis (TGA/DSC3+, Switzerland) was conducted in an air atmosphere, with a temperature range from 40 to 100 °C at a rate of 10 °C min^{-1} .

CONCLUSIONS

CO_2 -derived carbon ($\text{CO}_2\text{-C}$) support was pretreated with H_2O_2 and KOH solutions prior to Pt deposition in order to enhance the ORR performance of the synthesized electrocatalysts indirectly by introducing oxygen groups to the carbon surface for improved Pt deposition and optimizing the metal–support interaction (MSI). Results of the N_2 -physisorption study showed that both pretreatments led to a higher BET surface area, which was 33.49 $\text{m}^2\ \text{g}^{-1}$ higher than Pt with untreated $\text{CO}_2\text{-C}$ support (Pt/ $\text{CO}_2\text{-C}$) in the case of Pt/ $\text{H}_2\text{O}_2\text{-CO}_2\text{-C}$. At the same time, the XPS study indicated improved metal–support interaction for Pt/KOH- $\text{CO}_2\text{-C}$ and Pt/ $\text{H}_2\text{O}_2\text{-CO}_2\text{-C}$ and revealed that functionalization of $\text{CO}_2\text{-C}$ with oxygen-containing groups was successfully performed in both pretreatment solutions. Positive implications of the physical characterization results were verified with electrochemical characterization. It was found that Pt/ $\text{H}_2\text{O}_2\text{-CO}_2\text{-C}$ had the lowest overpotential toward ORR among all samples including the commercial Pt/C and higher mass activity than Pt/ $\text{CO}_2\text{-C}$ and Pt/KOH- $\text{CO}_2\text{-C}$ while specific activity was the highest for Pt/KOH- $\text{CO}_2\text{-C}$. Furthermore, with much lower loss in EASA after ADT, Pt/ $\text{H}_2\text{O}_2\text{-CO}_2\text{-C}$ and Pt/KOH- $\text{CO}_2\text{-C}$ were observed to be more durable to the reaction conditions than the commercial Pt/C. Overall, the study highlighted the advantageous influence of pretreatment on CO_2 -derived carbon supports for Pt electrocatalysts, as pretreatment with KOH and H_2O_2 solutions was associated with enhanced ORR performance.

ASSOCIATED CONTENT

Data Availability Statement

The data generated during this study are available from the corresponding author upon reasonable request.

Supporting Information

The Supporting Information is available free of charge at <https://pubs.acs.org/doi/10.1021/acs.energyfuels.4c02407>.

TGA results for all samples; PDS histograms of all samples; ORR polarization curves of all samples with different rotation rates; Koutecký–Levich plots of all samples; XPS analysis of all samples (PDF)

AUTHOR INFORMATION

Corresponding Author

Ivar Kruusenberg – National Institute of Chemical Physics and Biophysics, Tallinn 12618, Estonia; orcid.org/0000-0002-8199-9324; Email: ivar.kruusenberg@kbfi.ee

Authors

Erkin Najafli – National Institute of Chemical Physics and Biophysics, Tallinn 12618, Estonia; orcid.org/0000-0001-9873-3795

Sander Ratso – National Institute of Chemical Physics and Biophysics, Tallinn 12618, Estonia; Nuclear Engineering Department, University of California, Berkeley, California 94709, United States

Amir Foroozan – Department of Chemical Engineering, McMaster University, Hamilton, Ontario L8S 4L7, Canada

Navid Noor – Department of Chemical Engineering, McMaster University, Hamilton, Ontario L8S 4L7, Canada

Drew C. Higgins – Department of Chemical Engineering, McMaster University, Hamilton, Ontario L8S 4L7, Canada; orcid.org/0000-0002-0585-2670

Complete contact information is available at:

<https://pubs.acs.org/doi/10.1021/acs.energyfuels.4c02407>

Notes

The authors declare no competing financial interest.

ACKNOWLEDGMENTS

This work was supported by the Estonian Research Council grants PSG312, PUTJD1233, EAG271, and under ESA Contract No. 4000134761/21/NL/GLC/my by the European Space Agency and by the National Institute of Chemical Physics and Biophysics and the Natural Sciences and Engineering Research Council of Canada (NSERC) International Collaboration program. Electron microscopy was performed at the Canadian Centre for Electron Microscopy (CCEM) at McMaster University. X-ray photoelectron spectroscopy was performed at the Surface Science Western at Western University.

REFERENCES

- (1) van Ruijven, B. J.; De Cian, E.; Sue Wing, I. Amplification of Future Energy Demand Growth Due to Climate Change. *Nat. Commun.* **2019**, *10* (1), No. 2762.
- (2) Welsby, D.; Price, J.; Pye, S.; Ekins, P. Unextractable Fossil Fuels in a 1.5 °C World. *Nature* **2021**, *597* (7875), 230–234.
- (3) Tellez-Cruz, M. M.; Escorihuela, J.; Solorza-Feria, O.; Compañ, V. Proton Exchange Membrane Fuel Cells (PEMFCs): Advances and Challenges. *Polymers* **2021**, *13* (18), No. 3064.
- (4) Gómez-Marín, A.; Feliu, J. M. Oxygen Reduction on Platinum Single Crystal Electrodes. *Encycl. Interfacial Chem.* **2018**, 820–830.
- (5) Suib, S. L. New and Future Developments in Catalysis: Batteries, Hydrogen Storage and Fuel Cells. *New Future Dev. Catal.* **2013**, 1–535.
- (6) Serp, P.; Machado, B. *Nanostructured Carbon Materials for Catalysis*; Royal Society of Chemistry, 2015.
- (7) Najafli, E.; Ratso, S.; Ivanov, Y. P.; Gatalo, M.; Pavko, L.; Yörük, C. R.; Walke, P.; Divitini, G.; Hodnik, N.; Kruusenberg, I. Sustainable CO_2 -Derived Nanoscale Carbon Support to a Platinum Catalyst for Oxygen Reduction Reaction. *ACS Appl. Nano Mater.* **2023**, *6* (7), 5772–5780.
- (8) Du, L.; Shao, Y.; Sun, J.; Yin, G.; Liu, J.; Wang, Y. Advanced Catalyst Supports for PEM Fuel Cell Cathodes. *Nano Energy* **2016**, *29*, 314–322.

- (9) Lázaro, M. J.; Calvillo, L.; Celorrio, V.; Pardo, J. I.; Perathoner, S.; Moliner, R. Study and Application of Carbon Black Vulcan XC-72R in Polymeric Electrolyte Fuel Cells. In *Carbon Black: Production, Properties and Uses*; Nova Science Publishers, Inc., 2011; pp 41–68.
- (10) Moreno-Castilla, C.; Ferro-García, M. A.; Joly, J. P.; Bautista-Toledo, I.; Carrasco-Marín, F.; Rivera-Utrilla, J. Activated Carbon Surface Modifications by Nitric Acid, Hydrogen Peroxide, and Ammonium Peroxydisulfate Treatments. *Langmuir* **1995**, *11* (11), 4386–4392.
- (11) Shao, M. Electrocatalysis in Fuel Cells. *Catalysts* **2015**, *5* (4), 2115–2121.
- (12) Kumar, S. M. S.; Hidyatai, N.; Herrero, J. S.; Irusta, S.; Scott, K. Efficient Tuning of the Pt Nano-Particle Mono-Dispersion on Vulcan XC-72R by Selective Pre-Treatment and Electrochemical Evaluation of Hydrogen Oxidation and Oxygen Reduction Reactions. *Int. J. Hydrogen Energy* **2011**, *36* (9), 5453–5465.
- (13) Ratso, S.; Walke, P. R.; Mikli, V.; Ločs, J.; Šmits, K.; Vitola, V.; Šutka, A.; Kruusenberg, I. CO₂ Turned into a Nitrogen Doped Carbon Catalyst for Fuel Cells and Metal–Air Battery Applications. *Green Chem.* **2021**, *23* (12), 4435–4445.
- (14) Rimmel, A. L.; Ratso, S.; Divitini, G.; Danilson, M.; Mikli, V.; Uibu, M.; Aruväli, J.; Kruusenberg, I. Nickel and Nitrogen-Doped Bifunctional ORR and HER Electrocatalysts Derived from CO₂. *ACS Sustainable Chem. Eng.* **2022**, *10* (1), 134–145.
- (15) Lacarbonara, G.; Chini, S.; Ratso, S.; Kruusenberg, I.; Arbizzani, C. A MnOx–Graphitic Carbon Composite for CO₂ for Sustainable Li-Ion Battery Anodes. *Mater. Adv.* **2022**, *3* (18), 7087–7097.
- (16) Davey, W. P. Precision Measurements of the Lattice Constants of Twelve Common Metals. *Phys. Rev.* **1925**, *25* (6), No. 753.
- (17) Guo, S.; Zhang, S.; Sun, S. Tuning Nanoparticle Catalysis for the Oxygen Reduction Reaction. *Angew. Chem., Int. Ed.* **2013**, *52* (33), 8526–8544.
- (18) Jackson, C.; Smith, G. T.; Inwood, D. W.; Leach, A. S.; Whalley, P. S.; Callisti, M.; Polcar, T.; Russell, A. E.; Leveque, P.; Kramer, D. Electronic Metal-Support Interaction Enhanced Oxygen Reduction Activity and Stability of Boron Carbide Supported Platinum. *Nat. Commun.* **2017**, *8* (1), No. 15802.
- (19) Dong, Y.; Wang, Y.; Tian, Z.; Jiang, K.; Li, Y.; Lin, Y.; Oloman, C. W.; Gyenge, E. L.; Su, J.; Chen, L. Enhanced Catalytic Performance of Pt by Coupling with Carbon Defects. *Innovation* **2021**, *2*, No. 100161.
- (20) Yan, Q. Q.; Wu, D. X.; Chu, S. Q.; Chen, Z. Q.; Lin, Y.; Chen, M. X.; Zhang, J.; Wu, X. J.; Liang, H. W. Reversing the Charge Transfer between Platinum and Sulfur-Doped Carbon Support for Electrocatalytic Hydrogen Evolution. *Nat. Commun.* **2019**, *10* (1), No. 4977.
- (21) Zhang, H.; Lv, K.; Fang, B.; Forster, M. C.; Dervişoğlu, R.; Andreas, L. B.; Zhang, K.; Chen, S. Crucial Role for Oxygen Functional Groups in the Oxygen Reduction Reaction Electrocatalytic Activity of Nitrogen-Doped Carbons. *Electrochim. Acta* **2018**, *292*, 942–950.
- (22) Kim, J. H.; Cheon, J. Y.; Shin, T. J.; Park, J. Y.; Joo, S. H. Effect of Surface Oxygen Functionalization of Carbon Support on the Activity and Durability of Pt/C Catalysts for the Oxygen Reduction Reaction. *Carbon* **2016**, *101*, 449–457.
- (23) Jerigová, M.; Odziomek, M.; López-Salas, N. We Are Here! Oxygen Functional Groups in Carbons for Electrochemical Applications. *ACS Omega* **2022**, *7* (14), 11544–11554.
- (24) Pavko, L.; Gatalo, M.; Đukić, T.; Ruiz-Zepeda, F.; Surca, A. K.; Šala, M.; Maselj, N.; Jovanović, P.; Bele, M.; Finšgar, M.; Genorio, B.; Hodnik, N.; Gabersček, M. Correlating Oxygen Functionalities and Electrochemical Durability of Carbon Supports for Electrocatalysts. *Carbon* **2023**, *215*, No. 118458.
- (25) Bhalothia, D.; Beniwal, A.; Yan, C.; Wang, K. C.; Wang, C. H.; Chen, T. Y. Potential Synergy between Pt₂Ni₄ Atomic-Clusters, Oxygen Vacancies and Adjacent Pd Nanoparticles Outperforms Commercial Pt Nanocatalyst in Alkaline Fuel Cells. *Chem. Eng. J.* **2024**, *483*, No. 149421.
- (26) Cappellari, P. S.; García, G.; Florez-Montaño, J.; Barbero, C. A.; Pastor, E.; Planes, G. A. Enhanced Formic Acid Oxidation on Polycrystalline Platinum Modified by Spontaneous Deposition of Gold. Fourier Transform Infrared Spectroscopy Studies. *J. Power Sources* **2015**, *296*, 290–297.
- (27) Kinoshita, K. Particle Size Effects for Oxygen Reduction on Highly Dispersed Platinum in Acid Electrolytes. *J. Electrochem. Soc.* **1990**, *137* (3), 845–848.
- (28) Bhalothia, D.; Yan, C.; Hiraoka, N.; Ishii, H.; Liao, Y.-F.; Chen, P.-C.; Wang, K.-W.; Chou, J.-P.; Dai, S.; Chen, T.-Y. Pt-Mediated Interface Engineering Boosts the Oxygen Reduction Reaction Performance of Ni Hydroxide-Supported Pd Nanoparticles. *ACS Appl. Mater. Interfaces* **2023**, *15*, 16177–16188.
- (29) Garsany, Y.; Singer, I. L.; Swider-Lyons, K. E. Impact of Film Drying Procedures on RDE Characterization of Pt/VC Electrocatalysts. *J. Electroanal. Chem.* **2011**, *662* (2), 396–406.
- (30) Garsany, Y.; Baturina, O. A.; Swider-Lyons, K. E.; Kocha, S. S. Experimental Methods for Quantifying the Activity of Platinum Electrocatalysts for the Oxygen Reduction Reaction. *Anal. Chem.* **2010**, *82* (15), 6321–6328.
- (31) Xu, Z.; Zhang, H.; Zhong, H.; Lu, Q.; Wang, Y.; Su, D. Effect of Particle Size on the Activity and Durability of the Pt/C Electrocatalyst for Proton Exchange Membrane Fuel Cells. *Appl. Catal., B* **2012**, *111–112*, 264–270.
- (32) Jia, Q.; Li, J.; Caldwell, K.; Ramaker, D. E.; Ziegelbauer, J. M.; Kukreja, R. S.; Kongkanand, A.; Mukerjee, S. Circumventing Metal Dissolution Induced Degradation of Pt-Alloy Catalysts in Proton Exchange Membrane Fuel Cells: Revealing the Asymmetric Volcano Nature of Redox Catalysis. *ACS Catal.* **2016**, *6* (2), 928–938.
- (33) Linge, J. M.; Erikson, H.; Merisalu, M.; Sammelselg, V.; Tammeveski, K. Oxygen Reduction on Silver Catalysts Electrodeposited on Various Nanocarbon Supports. *SN Appl. Sci.* **2021**, *3* (2), 1–10.
- (34) You, X.; Han, J.; Del Colle, V.; Xu, Y.; Chang, Y.; Sun, X.; Wang, G.; Ji, C.; Pan, C.; Zhang, J.; Gao, Q. Relationship between Oxide Identity and Electrocatalytic Activity of Platinum for Ethanol Electrooxidation in Perchlorate Acidic Solution. *Commun. Chem.* **2023**, *6* (1), 1–9.
- (35) Wei, C.; Rao, R. R.; Peng, J.; Huang, B.; Stephens, I. E. L.; Risch, M.; Xu, Z. J.; Shao-Horn, Y. Recommended Practices and Benchmark Activity for Hydrogen and Oxygen Electrocatalysis in Water Splitting and Fuel Cells. *Adv. Mater.* **2019**, *31* (31), No. 1806296.
- (36) Bard, A. J.; Faulkner, L. R. *Electrochemical Methods: Fundamentals and Applications*, 2nd ed.; Wiley, 2000.
- (37) Marković, N.; Gasteiger, H. A.; Grgur, B. N.; Ross, P. N. Oxygen Reduction Reaction on Pt(111): Effects of Bromide. *J. Electroanal. Chem.* **1999**, *467* (1–2), 157–163.
- (38) Łukaszewski, M.; Soszko, M.; Czerwiński, A. Electrochemical Methods of Real Surface Area Determination of Noble Metal Electrodes – an Overview. *Int. J. Electrochem. Sci.* **2016**, *11* (6), 4442–4469.
- (39) Peng, L.; Zhang, J.; Xue, Z.; Han, B.; Sang, X.; Liu, C.; Yang, G. Highly Mesoporous Metal–Organic Framework Assembled in a Switchable Solvent. *Nat. Commun.* **2014**, *5* (1), No. 4465.

Appendix 3

Publication III

Erkin Najafli, Sander Ratso, Amir Foroozan, Navid Noor, Drew C. Higgins, and Ivar Kruusenberg, Functionalization of CO₂-Derived Carbon Support as a Pathway to Enhancing the Oxygen Reduction Reaction Performance of Pt Electrocatalysts *Energy & Fuels* 2024 38 (16), 15601–15610 DOI: 10.1021/acs.energyfuels.4c02407.



Optimizing Pt catalyst performance for oxygen reduction reaction via surface functionalization of Vulcan XC-72R carbon black support

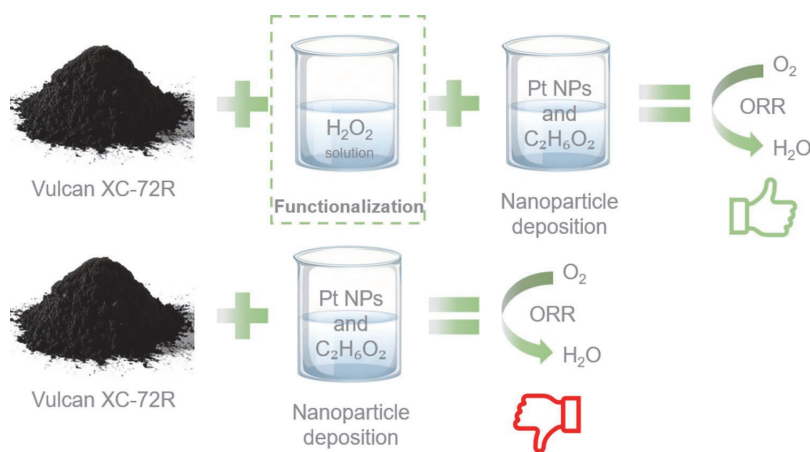
Erkin Najafli¹ · Maarja Grossberg² · Valdek Mikli² · Peter Walke² · Sander Ratso¹ · Ivar Kruusenberg¹

Received: 12 September 2024 / Accepted: 12 December 2024
© The Author(s), under exclusive licence to Springer Nature B.V. 2025

Abstract

In this study, the impact of Vulcan XC-72R carbon black support pre-treatment on the oxygen reduction reaction performance of the Pt catalyst was investigated. Catalysts were synthesized via the polyol method using ethylene glycol, with different pre-treatment pathways (with H₂O₂ and HNO₃ solutions) applied to the carbon black for surface functionalization. Additional samples using non-treated XC-72R and N-doped XC-72R were prepared for comparison, alongside a commercial Pt/C catalyst. Electrochemical characterization revealed that H₂O₂ pre-treatment resulted in the largest electrochemically active surface area and enhanced oxygen reduction reaction activity, surpassing both non-treated and commercial catalysts. The H₂O₂-treated catalyst exhibited superior stability during accelerated stress testing. SEM and XRD analyses confirmed the presence of Pt nanoparticles with sizes between 2.93 and 4.46 nm (that are considered optimal) for the H₂O₂-treated sample. Raman spectroscopy indicated that H₂O₂ pre-treatment led to a less ordered carbon structure with more defects, which is favorable for improved Pt utilization. It was concluded that H₂O₂ pre-treatment of XC-72R significantly improves the catalytic activity of the Pt catalyst, demonstrating the potential for optimizing Pt loading while maintaining desired ORR kinetics in fuel cell applications.

Graphical Abstract



Keywords Fuel cell · Platinum catalyst · Vulcan carbon · Chemical pre-treatment · Oxygen reduction reaction

Extended author information available on the last page of the article

Published online: 28 January 2025

Springer

1 Introduction

The stabilization of greenhouse gas concentrations to prevent “dangerous anthropogenic interference with the climate system” has been stated as the ultimate objective of the United Nations Framework Convention on Climate Change (UNFCCC) [1]. Fuel cells are among the proposed clean energy technologies to cut CO₂ emissions in various fields [2]. Nevertheless, the fuel cell industry is still challenged with a major bottleneck of the expensive Pt-based catalysts used to accelerate the core oxygen reduction reaction [3]. However, there are several promising solutions that may bring improved economic and technological viability for the fuel cell systems. One of these solutions is to cut the cost by reducing the amount of platinum used in these catalysts without compromising the electrochemical activity of the material and even increasing it in some cases [4]. This is accomplished using support materials such as carbon black to increase the utilization of Pt by increasing the available Pt surface area while decreasing the mass of Pt needed [5]. Moreover, it is also possible to take an extra step and apply pre-treatment to the carbon black material in order to further increase the activity of the catalyst material toward the oxygen reduction reaction (ORR) and improve its electrochemically active surface area (EASA) by controlling the nanoparticle size of the final sample [6, 7]. The polyol synthesis method is suitable for reaching Pt nanoparticle size within a 1.8 to 4.7 nm window and agglomeration of the particles is avoided with this process [7]. Among pre-treatment methods for carbon black, functionalization via hydrogen peroxide and nitric acid solutions is a common and effective way to form oxygen groups on the surface leading to improved Pt utilization as these groups act as anchoring points for Pt nanoparticles during synthesis [8, 9]. Thus, it is assumed that the synergy of the chosen carbon black pre-treatment and polyol synthesis method may result in higher mass and specific activities for ORR as it has been shown that heat-treated and size-controlled samples surpass the commercial Pt/C in terms of electrochemical activity [10].

This work aims to study the effect of H₂O₂ and HNO₃ pre-treatment methods on commercial Vulcan carbon black which is used as support material for Pt nanocatalyst for oxygen reduction reaction. The prepared catalyst samples are contrasted with Pt catalyst supported with N-doped carbon black and commercial Pt/C by physical and electrochemical characterization.

2 Experimental

2.1 Materials

Vulcan XC-72R (shortly XC) from The Fuel Cell Store (USA) with an average particle size of 50 nm, nitric acid (65% from Sigma-Aldrich, Germany), hydrogen peroxide (30% from Lach-Ner, s.r.o., the Czech Republic), ethylene glycol (99.5%, Lach-Ner), NaOH (98%, from Sigma-Aldrich, Germany), dihydrogen hexachloroplatinate (IV) hydrate (99.9% metal basis, from Alfa Aesar, USA), acetone (99.5% from Aldrich), polyvinylpyrrolidone (PVP) Mv-40,000, dicyandiamide (DCDA), ethanol (100%, from Chem-Lab, Belgium), platinum on graphitized carbon (commercial Pt/C, 20-wt. % Pt loading from Sigma-Aldrich, USA), and deionized water (from Merck Millipore, USA).

2.2 Pre-treatment of carbon black

Two chemical pre-treatment pathways (with 65% nitric acid and 30% hydrogen peroxide that were not processed further) were used in this work. Before the pre-treatment, a three-neck round bottom flask was washed with the so-called Piranha solution to ensure clean glassware. Then 0.5 g of the XC were dispersed in 500 ml of 5% HNO₃ and 10% H₂O₂ and refluxed with a temperature ranging from 80 to 110 °C for 18 h. Next, the mixture was cooled at room temperature, washed with a continuous flow of deionized water for 20 min and filtered with a PTFE membrane. As the last step of the pre-treatment, the XC was dried in an oven (PEAKS PCD-C6(5)000/China) at 105 °C for 12 h.

2.3 Synthesis of the catalyst samples

2.3.1 Pt/XC polyol synthesis protocol

First, 40 ml of ethylene glycol (EG) was taken and measured (CyberScan PC 510 pH meter) to find the initial pH. Then, to achieve a pH level of 11, 0.4 ml of 1-M NaOH was added to the EG. Next, 0.25 g of the pre-treated XC was mixed with 15 ml of the pH-adjusted EG and stirred with magnetic bar under N₂ flow for 1 h. To get a 20% loading of Pt on XC (1:4 Pt to XC ratio), 131.25 mg of H₂PtCl₆ in crystalline form was measured and diluted to 17 ml of deionized water. After adding the diluted platinum precursor solution to the EG-XC mixture, it was refluxed for 3 h at 115 °C under N₂ flow. As the last step

of the synthesis, the refluxed mixture was stirred overnight under N₂ flow and washed with a continuous flow of deionized water and with acetone for a very short period after which the sample was dried in an oven for 3 h at 110 °C.

2.3.2 Pt/N-doped XC polyol synthesis protocol

For doping, 0.4 g of XC was mixed with 0.04 g of PVP powder and 8 g (20 times more than XC) of DCDA. After adding ethanol to the mixture in an Erlenmeyer flask, it was sonicated in an ultrasonic bath for 1.5 h. Then, the mixture was dried at 75 °C for about 1 h and 20 min. Next, a quartz boat was used to put it in an oven and purged with N₂ flow for 15 min prior to activation at 800 °C (heating rate of 10 °C/min) for 2 h under N₂. After cooling down the oven to room temperature, the sample was taken and measured. The polyol synthesis process for N-doped XC was the same as the other Pt/XC samples reported in the previous part.

2.4 Characterization of the catalysts

2.4.1 Electrochemical characterization

To prepare the catalyst ink for RDE (rotating disk electrode) measurement, 1 mg of the catalyst sample powder was mixed with 0.405 μl of Nafion (5%), 250 μl of isopropanol (from Stanchem Sp. z o.o, Poland), and 750 μl of deionized water (1:3 alcohol to water ratio) water. Then, the mixture was sonicated for 1 h at a temperature of <40 °C. Before ink deposition, the electrodes were polished with 1.0- and 0.30-μm alumina paste slurry (from Buehler, USA) in a figure-eight motion to ensure a uniform surface to a mirror finish. The polished electrodes were first sonicated in isopropanol (5 min) and then in deionized water (5 min) to remove alumina residues. The prepared ink was deposited to the electrode surface in three steps of 10 μl (30 μl in total to achieve Pt loading of 30 μgcm⁻² on the glassy carbon surface) via drop-casting method with a pipette. Between the steps, the electrode was dried in an oven and the ink was sonicated.

Cyclic voltammetry (CV) measurements were conducted in a conventional three-electrode system at room temperature and 0.5-M H₂SO₄ (98%, from VWR Chemicals) solution was used as the electrolyte. The potentiostat (Interface 1010E or Reference 600+ of Gamry instruments from USA) was controlled by Gamry software with Saturated Calomel Electrode (SCE) and platinum wire as reference and counter electrodes, respectively. It must be noted that all of the following potential values in this work were converted to Reversible Hydrogen Electrode (RHE). The working electrode was composed of a glassy carbon with a surface area of 0.2 cm² modified with the selected catalyst. The first part of the CV was carried out in order to investigate the

electrochemically active surface area of the samples. However, prior to this experiment, the cell was purged with N₂ for 25 min and later the sample was activated by applying 100 potential cycles in the voltage range of -0.2 V to 1.2 V vs SCE at the scan rate of 500 mVs⁻¹ under N₂ flow. After the activation, the voltage range was kept the same and the CV was performed in two different scan rates of 100 mVs⁻¹ and 10 mVs⁻¹ with N₂-saturated electrolyte. With the second part of the measurement, the goal was to analyze the degradation and ORR properties of the samples. The cell was purged with O₂ for 25 min before starting the experiment. To research the aging profile of the samples, first, they were cycled 500 times with the voltage range of -0.2 V to 1.2 V vs SCE at 500 mVs⁻¹ under the O₂ atmosphere. In this case, the first and final CV curves were obtained to compare the characteristics of the samples after being exposed to 500 potential cycles. Next, the voltage range was adjusted to -0.2 V to 0.8 V in order to conduct the ORR kinetics experiment at 10 mVs⁻¹ with O₂ flow. For this part of the measurement, electrode rotation was applied with changing RPM (Revolutions Per Minute) levels between 400 and 4400.

The number of transferred electrons per O₂ molecule and the kinetic current was calculated using the Koutecký-Levich equation [11]:

$$\frac{1}{i} = \frac{1}{i_k} + \frac{1}{i} = -\frac{1}{nFkc_{O_2}^b} - \frac{1}{0.62nFD_{O_2}^{\frac{2}{3}} \nu^{-\frac{1}{6}} \omega^{\frac{1}{2}} c_{O_2}^b}$$

Here, i is the measured current density, i_k is the kinetic current density, i_d is the diffusion-limited current density, n is the overall number of electrons transferred per O₂ molecule, k is the electron transfer rate constant, F is the Faraday constant ($F=96,485 \text{ C mol}^{-1}$), D_{O_2} is the diffusion coefficient of oxygen ($1.93 \times 10^{-5} \text{ cm}^2 \text{ s}^{-1}$ in 0.1 M HClO₄ [12]), ν is the kinematic viscosity of the electrolyte ($1.009 \times 10^{-2} \text{ cm}^2 \text{ s}^{-1}$ in 0.1 M HClO₄), ω is the angular velocity of the rotating disk ($\omega=2\pi N$, N is the linear rotating speed in rpm), and C_{O_2} is the bulk concentration of oxygen ($1.26 \times 10^{-3} \text{ mol L}^{-1}$ in 0.1 M HClO₄).

2.4.2 Physical characterization

The physical properties of the prepared catalysts were analyzed by various characterization methods. X-ray diffraction (XRD) measurement was performed with the X'Pert3 Powder system by Malvern Panalytical at 40 mA and 45 kV. To obtain the microimages of Pt/XC-72R (H₂O₂ treated), FEG (field emission gun)-SEM was employed operated by Zeiss Ultra 55. Additionally, an Energy-dispersive X-ray spectroscopy (EDX) spectrum was also acquired to study the composition of the sample in more detail. The microstructure of carbon black for each sample was studied using the micro-Raman spectrometer Horiba LabRam HR800 with

a 532-nm laser line for investigating the defective nature of the carbon molecules in detail.

3 Results and discussion

3.1 Electrochemical performance

Electrochemically active surface area (EASA) for all catalysts was calculated based on the cyclic voltammogram shown in Fig. 1 and tabulated in Table 1. It was found that the electrochemically active surface area of the catalyst with H_2O_2 -treated XC was the largest among all the samples and compared to commercial Pt/C it was 46.3% larger. While H_2O_2 treatment resulted in significant increase in EASA, both HNO_3 treatment and N-doping were found to decrease the EASA of Vulcan carbon. Increased EASA of H_2O_2 -treated Pt/XC-72R indicates improved Pt nanoparticle utilization owing to the oxygen groups that aid with retaining nanoparticles on the surface during polyol synthesis. At the same time, the relatively low slope of the hydrogen desorption peak for Pt/XC-72 (H_2O_2 treated) may be attributed to the chemical modification of the carbon support surface by H_2O_2 treatment, which affects the Pt–H bond strength and electronic properties. This pre-treatment introduces oxygen-containing groups that alter the adsorption–desorption kinetics of hydrogen on the Pt surface leading to the observed behavior.

To characterize ORR activity, a linear sweep voltammogram (LSV) comparing all the samples at 1600 rpm is given below in Fig. 2. Determining the onset potential for each sample is important to evaluate at which potential the reduction starts to occur. It was found that both

Table 1 EASA values for the samples

	Commercial Pt/C	Pt/XC (HNO_3 treated)	Pt/XC (H_2O_2 treated)	Pt/XC (non-treated)	Pt/N-XC (non-treated)
EASA	77.83 (m^2/g)	13.16	113.88	83.65	65.70

hydrogen peroxide- and nitric acid-treated samples exhibited superior onset potential of 0.95 V and 0.93 V, respectively, in comparison to the commercial Pt/C (0.89 V) and other catalysts (N-doped XC – 0.90 V and non-treated XC – 0.86 V). This indicates that Pt/XC-72R (H_2O_2 treated) material has the highest catalytic activity toward the ORR and this agrees well with the high EASA value of the same sample. At the same time, diffusion-limited current density (j_{lim} between 0.2 V and 0.7 V, from Levich equation) of this catalyst is around $-5.3 \text{ mA}\cdot\text{cm}^{-2}$ and higher than any other sample again meaning a higher electrocatalytic activity. The steep reduction wave of the hydrogen peroxide-treated material in the mixed kinetic diffusion control region ($0.2 \text{ V} < 0.7 \text{ V}$) and its flatter diffusion-limited current density plateau are also associated with favorable ORR properties for the catalyst. Meanwhile, the polarization curve of the HNO_3 -treated material was inferior in terms of the gradual reduction wave and smaller diffusion-limited current density.

On the other hand, there was a minor difference between the onset potentials of Pt/N-XC-72R and commercial Pt/C translating to similar, thus a reasonable catalytic activity for the material. The limiting current density for the N-doped XC sample is slightly higher than the commercial Pt/C which is an advantage. However, in case of the sample with XC that was not exposed to pre-treatment, the

Fig. 1 Comparison of cyclic voltammograms for all five samples recorded at 10 mVs^{-1} under N_2 saturation (0.5-M H_2SO_4) at room temperature. A Hydrogen desorption region and B oxide reduction peaks

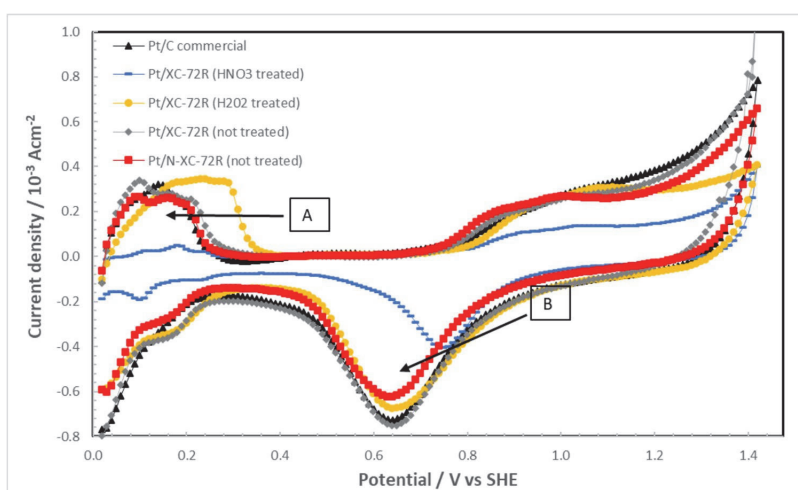
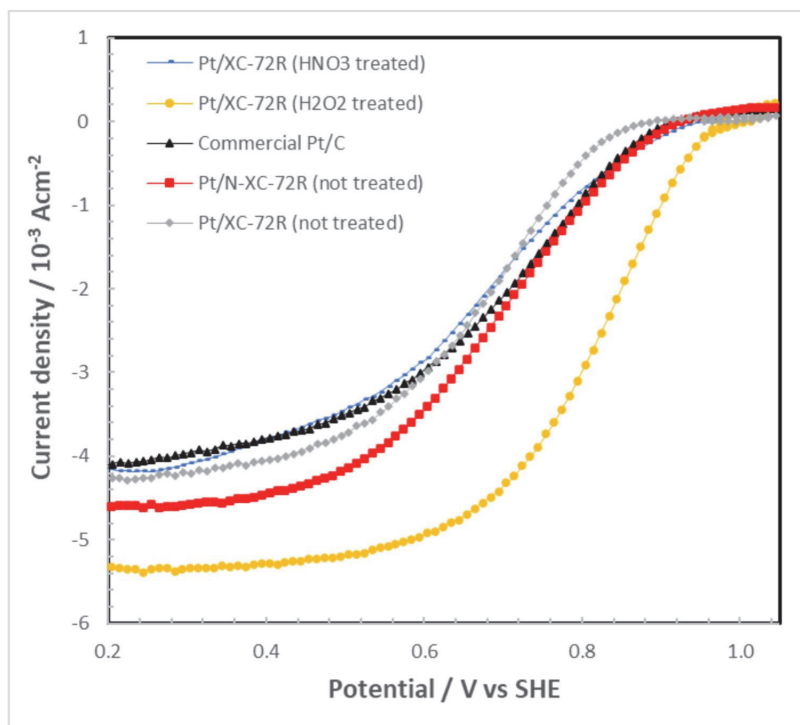


Fig. 2 LSVs for all samples (1600 rpm) at 10 mVs^{-1} under O_2 saturation ($0.5\text{-M H}_2\text{SO}_4$)



onset potential was minimum and there was a shoulder in the mixed kinetic diffusion-controlled region indicating to poorer ORR activity.

The superior tendency of the H_2O_2 -treated sample can also be observed in the oxide reduction peaks (Fig. 1) of CV recorded at 10 mVs^{-1} (double-layer charging corrected) in which its current density peak value is almost as high as the commercial Pt/C. The well-defined reduction peaks for all materials occur around 0.65 V except for the nitric acid-treated sample which has a shifted and smaller peak at 0.76 V presumably due to slower oxide reduction kinetics. The activity of Pt/N-XC-72R (non-treated) material was also consistent in comparison to the commercial Pt/C in both CV and LSV curves.

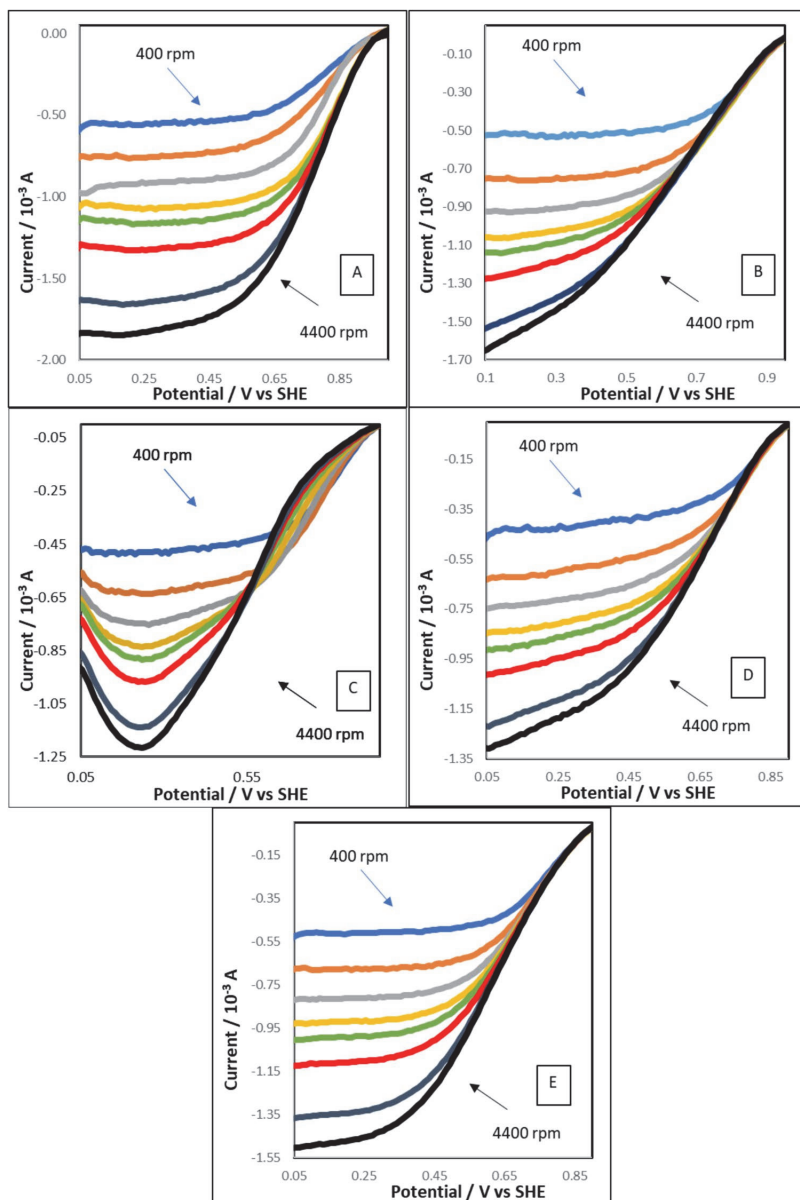
Overall, it is assumed that the type of performed pre-treatment might lead to improved activity in different magnitudes as seen from LSV plots of nitric acid (adequate)- and hydrogen peroxide (superior)-treated samples. However, it is counter-intuitive to observe that Pt/XC-72R (non-treated) also had similar peak values (current density) to the commercial sample and even slightly surpassing it in case of the oxide reduction peak as shown in Fig. 1. For a more detailed comparison of the H_2O_2 -treated sample with the non-treated material, ORR polarization curves

at different rotation rates for both materials are illustrated (see Fig. 3) next to each other along with the polarization curves of the other studied catalysts.

Both curves demonstrate a linear relationship between the diffusion-limited current and the rotation rate. However, this is more clearly observed in case of the treated material in which the flatter diffusion-controlled region is observed in every rotation level with a stable current value indicating better activity. At the same time, the non-treated sample has overlapping curves extending to the diffusion-controlled zone, especially at higher rotations and the limiting current stability is almost non-existent in the case of the 4400 rpm rotation speed. Slightly higher limiting current values and well-defined plateau of the Pt/XC-72R (H_2O_2 treated) catalyst material can be attributed to a high quantity of oxygen molecule diffusion to the catalyst surface and thus better oxygen reduction characteristics [13]. These results support that hydrogen peroxide pre-treatment of Vulcan carbon leads to enhanced catalytic activity toward ORR for the final catalyst material.

Koutecky–Levich (shortly KL) plots (Fig. 4) were used to characterize the electron transfer mechanism employed by the catalysts. It was found that number of electrons transferred during ORR was around 4.4 for H_2O_2 -treated sample

Fig. 3 ORR polarization curves of **A** Pt/XC-72R (H_2O_2 treated); **B** Pt/XC-72R (non-treated); **C** Pt/XC-72R (HNO_3 treated); **D** commercial Pt/C; and **E** Pt/N-XC-72R (not treated) samples under O_2 saturation obtained at different rotation speeds ($0.5\text{-M H}_2\text{SO}_4$ 10 mVs.^{-1})



at 0.6 V. This is within the commonly referred 10% deviation rate for four-electron transfer pathway and the excess value (~ 0.4) has been reported in other studies as well [14]. Although the transferred electron values were slightly higher (around 5) in the case of the non-treated sample, the reduction can still be attributed to the analogical (4-electron) pathway. For HNO_3 -treated, commercial Pt/C, and N-doped samples, the values were 3.8, 4.5, and 4.3, respectively. This

suggests that all samples were involved in the four-electron pathway for ORR which is advantageous to the two-electron pathway as the latter results in H_2O_2 formation which is corrosive for the catalyst environment and the oxygen molecule utilization level is higher in case of the direct reduction [15].

Additionally, KL plots for all materials demonstrate a linear relationship meaning first-order ORR kinetics with respect to the oxygen concentration; however, Pt/

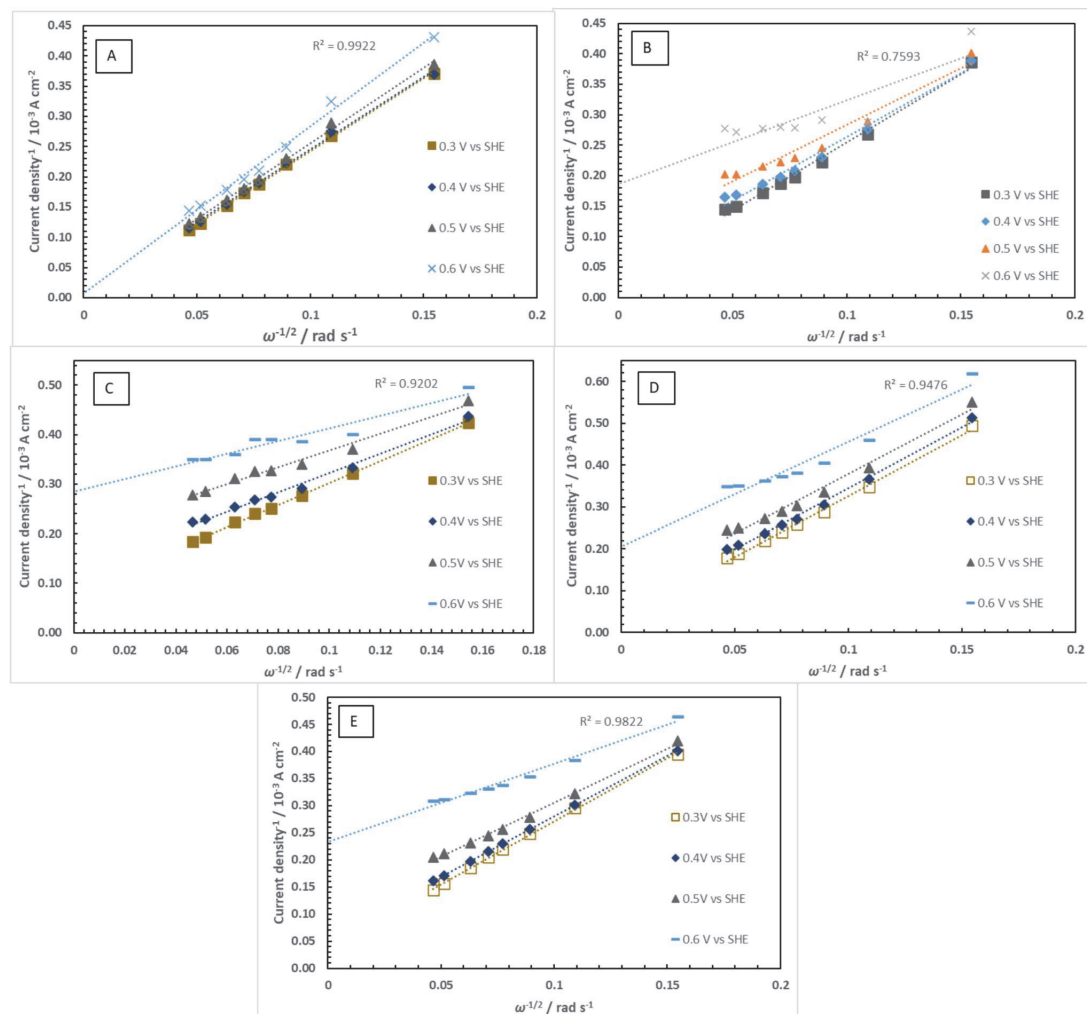


Fig. 4 Koutecky–Levich plots of **A** Pt/XC-72R (H_2O_2 treated); **B** Pt/XC-72R (non-treated); **C** Pt/XC-72R (HNO_3 treated); **D** commercial Pt/C, and **E** Pt/N-XC-72R (not treated) samples at different voltage and rotation rate values

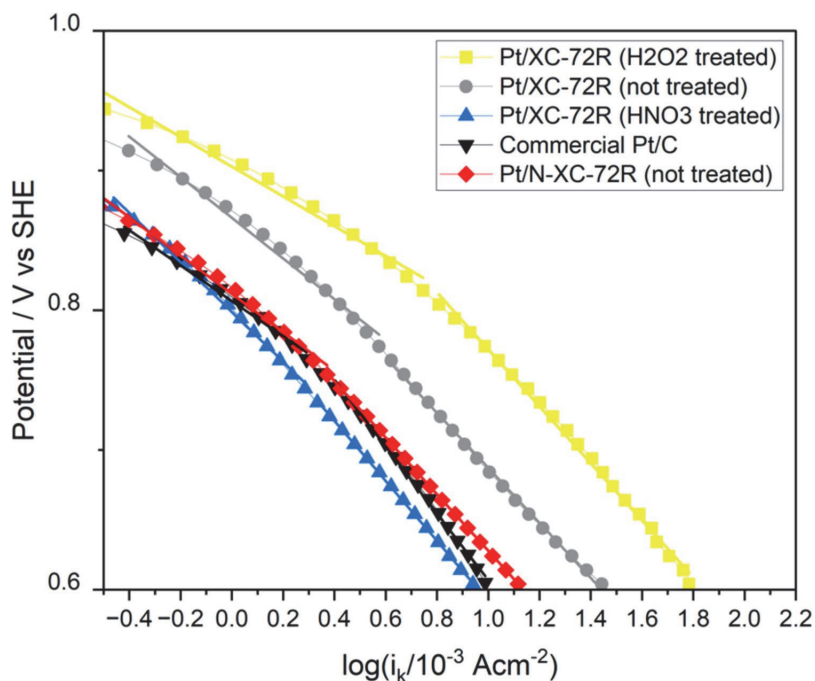
XC-72R (non-treated) has a disproportionate and overlapping dependence, especially at higher-voltage values. Such irregularity might be due to a malfunction during the RDE testing or simply because of the sample's nature. To draw a conclusion regarding the comparison of KL analysis for H_2O_2 - and non-treated samples, the y-intercept value for both plots has been obtained visually. This intercept figure corresponds to the kinetic current density in the absence of the mass transfer limitations and the results are given in Table 2. It must be noted that the rest of the catalyst materials also exhibited a similar linear relationship between j^{-1} and $\omega^{-1/2}$. For comparison, the below table also contains the

calculated i_k , E_{onset} , mass, and specific activity (shortly MA and SA) values for all samples.

The Tafel plots are essential for evaluating ORR performance, and literature reports indicate that a typical Pt/C catalyst exhibits slopes of around 60 mV dec^{-1} at low overpotentials and 120 mV dec^{-1} at higher overpotentials under acidic conditions [16]. The Tafel slopes obtained in this study (Fig. 5) for the catalysts differ from these standard values, which can be attributed to various factors, including differences in studied Pt facets, electrolyte purity, and range of fitting used [16] [17]. At higher overpotentials, the H_2O_2 -treated Pt/XC-72R catalyst demonstrates a Tafel slope

Table 2 Kinetic current density, mass, and specific activity values for all samples at 0.5 V

	Commercial Pt/C	Pt/XC (HNO ₃ treated)	Pt/XC (H ₂ O ₂ treated)	Pt/XC (non-treated)	Pt/N-XC (non-treated)
i_k	0.01 A cm ⁻²	5	100	10	9
MA	0.33 A/mg _{Pt}	0.16	3.3	0.33	0.3
SA	428.2 μA cm ⁻²	1265.8	2926.8	398.4	456.5
E_{ons}	0.89 V	0.93 V	0.95 V	0.86 V	0.90 V

Fig. 5 Tafel plots of all samples

of approximately 106 mV dec⁻¹, indicating more favorable reaction kinetics compared to the other samples. This result aligns with previous findings that highlighted the enhanced catalytic activity of the H₂O₂-treated sample due to the introduction of surface functionalities. In contrast, the commercial Pt/C catalyst exhibits a slightly higher Tafel slope of around 127 mV dec⁻¹, consistent with values reported for Pt (110) facets, where the initial electron transfer to O₂ is considered the rate-limiting step [12]. On the other hand, the HNO₃-treated Pt/XC-72R catalyst shows a higher Tafel slope of about 177 mV dec⁻¹, indicating slower ORR kinetics. This result is in agreement with the previous discussions, where the HNO₃ treatment was shown to introduce surface groups that could hinder the electron transfer process. Similarly, the untreated Pt/XC-72R and Pt/N-XC-72R catalysts exhibit moderate slopes of approximately 146 mV dec⁻¹ and 137 mV dec⁻¹, respectively, demonstrating moderate ORR activity. At lower overpotentials, the trend remains

consistent as H₂O₂-treated Pt/XC-72R catalyst continues to exhibit a relatively low Tafel slope, confirming its superior kinetic performance. Conversely, the HNO₃-treated Pt/XC-72R shows the highest slope at lower overpotentials, further supporting the earlier conclusion that HNO₃ treatment might introduce surface defects or functional groups that negatively impact ORR efficiency. Overall, these results emphasize the critical role of surface treatments and doping strategies in determining ORR kinetics. The consistently lower Tafel slopes of the H₂O₂-treated Pt/XC-72R catalyst across different potential ranges further support the argument that H₂O₂ pre-treatment results in enhanced ORR performance for XC-supported Pt catalysts. In contrast, the higher slopes observed for the HNO₃-treated sample emphasize the need for careful optimization of surface modification processes, aligning with the broader conclusion that effective surface engineering is key to enhancing ORR activity.

The results reveal that Pt/XC (H_2O_2 treated) sample has the highest kinetic current density at 0.5 V (10 times the commercial Pt/C) while the nitric acid-treated material showed the lowest value (half of the commercial Pt/C). Identically, mass and specific activity for the H_2O_2 treated is superior to all other samples indicating excellent catalytic activity while the HNO_3 -treated sample suffers from surprisingly low values. This encourages the assumption that the type of pre-treatment chosen can affect the tendency of a material to be more active toward ORR and it is possible to conclude that Pt/XC-72R (H_2O_2 treated) catalyst has performed better than the commercial Pt/C sample in almost every approach.

3.2 Physical properties of the catalysts

Based on the promising and superior results obtained for the H_2O_2 -treated catalyst, its morphology was further studied with SEM in order to carry out in-depth analysis as shown in Fig. 6.

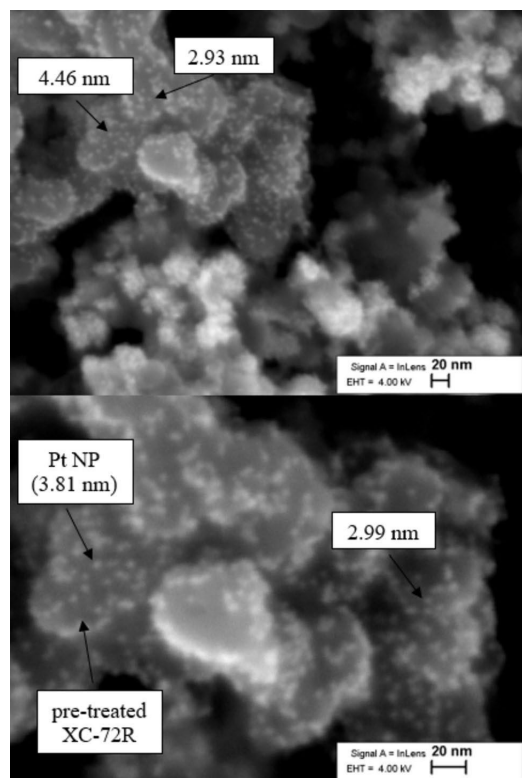


Fig. 6 SEM micrographs of Pt/XC-72R (H_2O_2 treated) sample

SEM images reveal that the majority of Pt NPs are uniformly distributed over XC-72R. Such distribution is a key characteristic for an efficient catalyst material as this increases the EASA and thus the catalytic activity for ORR. There are also agglomerated Pt sites on the sample. However, these sites are rather less populated. Hence, Pt utilization seems to be at an adequate level.

The nanoparticle size of Pt was also calculated with the SEM study and it was identified that the value changes between 2.93 nm and 4.46 nm. In another study, a Pt NP size of 4.4 nm was suggested as the optimum based on its maximum mass activity and balanced electrochemical stability [18]. Although there are also smaller particles present, the optimal value is almost identical to the NP size (4.46 nm) achieved in this study. This agrees well with the previous catalytic activity results collected for the H_2O_2 -treated sample.

On the other hand, the EDX spectrum for both general and Pt-rich areas of the sample was acquired with the data shown in Tables 3 and Table 4, respectively. The spectrum of the general area confirms the presence of C and Pt in the composition and the stoichiometric ratio of Pt to C (1:4) used in synthesis. In case of the Pt-rich area, the weight amount of Pt is about 53% more than the carbon amount.

To obtain more detailed information on the composition and crystal structure of the catalysts, XRD patterns (see Fig. 7) for all samples were obtained. Additionally, XC-72R without catalyst was also studied to detect its peaks and differentiate it from the Pt crystallites.

The calculated crystallite size for Pt/XC-72R (H_2O_2 treated) is similar to the results collected from the SEM measurement (see Table 5). At the same time, the size of the pre-treated samples is found to be higher than the non-treated sample suggesting an increase in particle size caused by the pre-treatment. If this is the case, HNO_3 treatment can

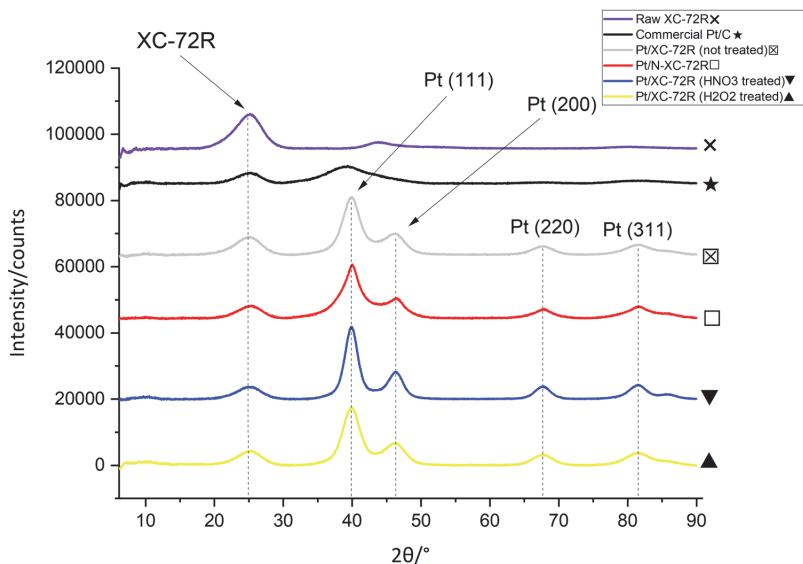
Table 3 General EDX spectrum

	Series	unn. C [wt. %]	norm. C [wt. %]	Atom. C [at. %]	Error [%]
Carbon	K-series	82.92	82.93	98.75	1.5
Platinum	M-series	17.07	17.07	1.25	0.7
Total		100	100	100	

Table 4 Pt-rich area EDX spectrum

	Series	unn. C [wt. %]	norm. C [wt. %]	Atom. C [at. %]	Error [%]
Carbon	K-series	23.59	23.70	83.46	3.5
Platinum	M-series	75.95	76.30	16.54	3.1
Total		99.53	100	100	

Fig. 7 X-ray diffraction (XRD) patterns for all samples



be employed to produce bigger particles, while H_2O_2 treatment may result in NPs with moderate particle size. It seems like N doping of the non-treated XC also leads to crystallite size comparable to that of the H_2O_2 -treated catalyst.

Furthermore, the obtained values show that commercial Pt/C has the lowest Pt crystallite size which can also be seen from its peak at around 40° . In addition, the XRD pattern for the commercial sample did not show the smaller peak at 46° presumably due to missing 200 plane in the lattice and contribution of the XC-72R (which was not present in this case) at 44° , while there were small-scale peaks at 67° and 81° associated with the 220 and 311 planes similar to rest of the samples.

Raman spectroscopy was performed to analyze the structure of carbon black contained in each sample as demonstrated in Fig. 8.

Three main peaks (or bands) are often used to characterize Raman spectra of a given material: the so-called D-band, G-band, and 2D (or G^*) band. In this work, only the first-order spectral range (1000 to 2000 cm^{-1}) is examined in which the corresponding D- and G-bands are shown in Fig. 8. It is possible to learn about the structural properties

of carbon material by finding the Raman shift value for each peak. For example, the D-band is caused by a disorder in the edge of a microcrystalline structure, while the G-band is formed due to the graphene presence [19].

As seen in the spectra, D- and G-bands occur around 1345 and 1595 cm^{-1} in all of the samples. A considerable rise in the intensity level (for D-band) is observed in the case of the pre-treated catalysts possibly due to increased disorder in the XC-72R structure caused by the heat treatment and N-doping of XC-72R in the case of the N-doped catalyst. The commercial Pt/C catalyst has slightly smaller band peaks in comparison to the other materials corresponding to a more ordered structural form of carbon black contained in this catalyst.

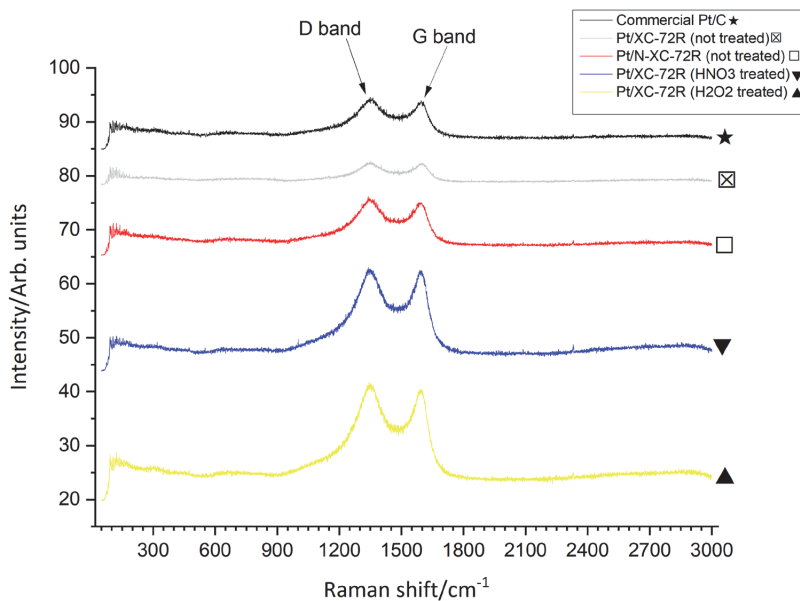
To compare the crystallinity and disorder of the catalysts, analytically obtained peak values are given (see Table 6) in the form of the Raman shifts related to both D and G-bands.

The intensity ratio (I_D/I_G) of samples is often used to compare different materials based on their microstructure. For example, the ratio value for the H_2O_2 -treated material is higher than the non-treated sample. This can be explained by decreased structural order and an increased number of defects in the composition of the Pt/XC-72R (H_2O_2 treated) catalyst. Increasing the number of defects on carbon black after treatment was a desirable property as this can be associated with a more porous structure with a higher number of sites for Pt deposition, thus better utilization, EASA value, and activity.

On the other hand, the crystal structure of the nitric acid-treated catalyst seems to be slightly more ordered like the non-treated material although its peak-intensity figures

Table 5 Crystallite size for each sample (taken from the peak of 111 plane)

	Commercial Pt/C	Pt/XC (HNO_3 treated)	Pt/XC (H_2O_2 treated)	Pt/XC (non-treated)	Pt/N-XC (non-treated)
Cr Size	1.5 (nm)	5.0	3.9	3.6	4.0

Fig. 8 Raman spectra for all samples (532-nm laser line)**Table 6** D- and G-band values for all samples obtained from Raman spectra

	Commercial Pt/C	Pt/XC (HNO ₃ treated)	Pt/XC (H ₂ O ₂ treated)	Pt/XC (non-treated)	Pt/N-XC (non-treated)
D-band	1349.813 (cm ⁻¹)	1340.069	1342.611	1351.508	1340.493
G-band	1594.693 (cm ⁻¹)	1590.033	1591.304	1598.930	1598.083
I_D^*	29.489	38.963	41.640	24.106	30.774
I_G^*	28.921	38.481	40.494	23.835	29.614
I_D/I_G	1.0196	1.0125	1.0283	1.0113	1.0391

*in arbitrary units

are comparable to that of the H₂O₂-treated sample. In case of the N-doped sample, the ratio was the highest, and the intensity values were similar to the commercial Pt/C which indicates that more ordered structure with fewer defects in comparison to the pre-treated materials. Thus, the effect of N-doping on XC-72R seems to be minuscule in terms of its morphology.

To characterize the electrochemical stability of the samples, accelerated stress testing (AST) with 500 potential cycles was applied and cyclic voltammograms before and after the AST were recorded (Fig. 9). Among the samples, Pt/XC-72R (treated with H₂O₂) displayed the most comparable CV to the AST results for the commercial Pt/C. Additionally, a noticeable shift to lower current values at high voltages was observed for all materials after the cycles. Regarding catalytic stability across all the curves, the CV for the H₂O₂-treated catalyst appeared to be minimally impacted by the stress testing, indicating that its durability exceeds that of the other materials, including the commercial Pt/C.

In contrast, Pt/XC-72R (untreated) showed a slightly higher current drop between 1.0 and 1.5 V, whereas the N-doped and HNO₃-treated samples exhibited similar and satisfactory durability.

4 Conclusion

This research focused on the influence of Vulcan XC-72R (carbon black) pre-treatment on the final properties of fuel cell catalyst materials with Pt nanoparticles. For this purpose, firstly catalyst samples with different treatment pathways (H₂O₂ and HNO₃ treatments) were synthesized via the polyol method using ethylene glycol.

Electrochemical characterization revealed that H₂O₂-treated material had the largest EASA surpassing the non-treated and commercial Pt/C catalyst, while HNO₃ treatment resulted in a much smaller EASA value. This suggests that H₂O₂ pre-treatment of XC-72R enhances the

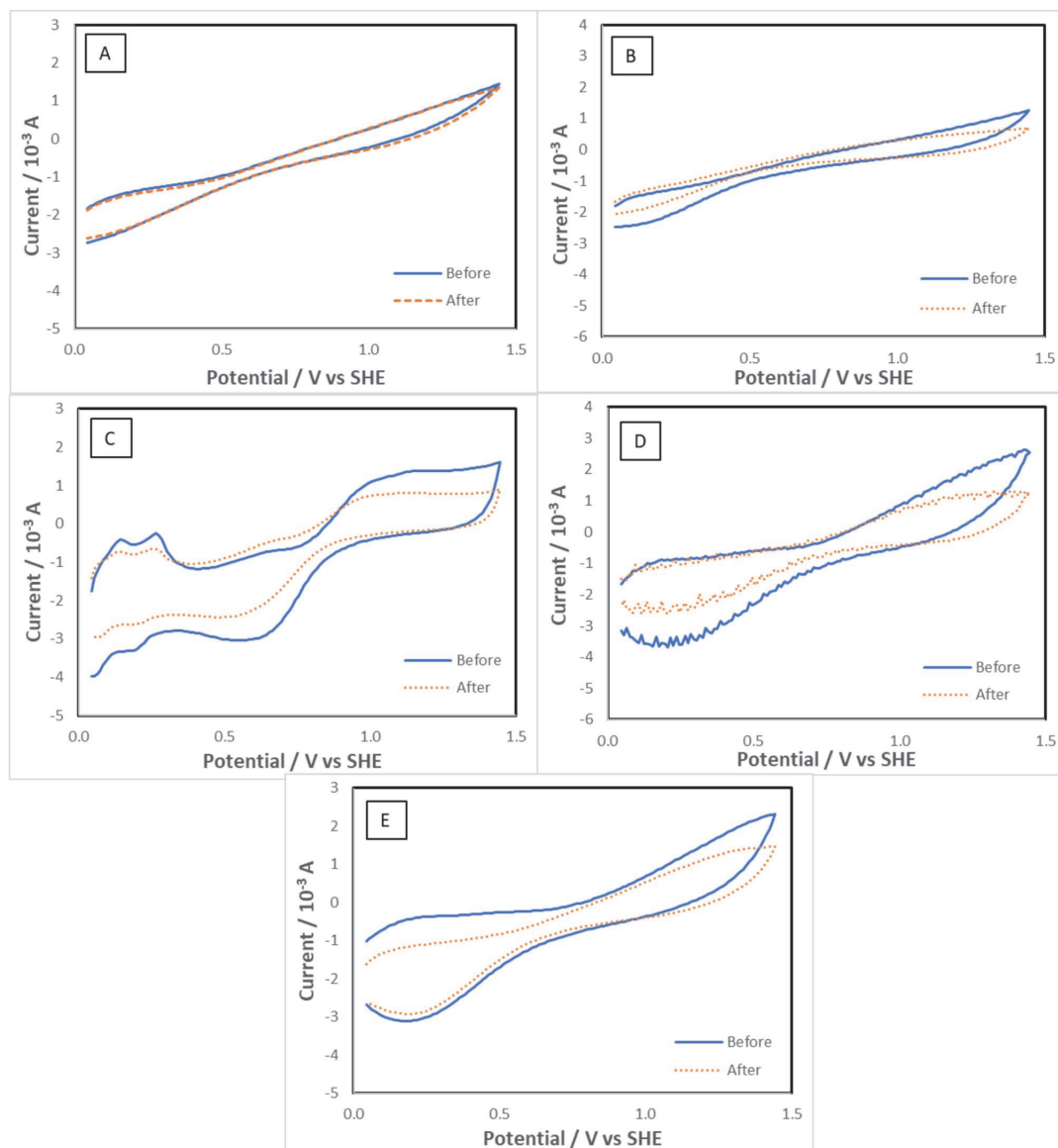


Fig. 9 Cyclic voltammogram curves of **A** Pt/XC-72R (H_2O_2 treated); **B** Pt/XC-72R (non-treated); **C** Pt/XC-72R (HNO_3 treated); **D** commercial Pt/C; and **E** Pt/N-XC-72R (not treated) before and after accelerated stress testing at 500 mVs^{-1} under O_2 saturation ($0.5\text{-M H}_2\text{SO}_4$)

electrochemically active surface area of the final sample. It was also identified that H_2O_2 treatment is linked to a considerable increase in the onset potential and high diffusion-limited current density value of $5.3 \text{ mA}\cdot\text{cm}^{-2}$. However, this was not observed in the case of the Pt/XC-72R (HNO_3 treated) catalyst as its polarization curve was not much different in contrast to the non-treated material despite

having a higher onset potential than the non-treated sample and being quite comparable to the plateau of commercial Pt/C. Higher limiting current values and well-defined current density plateau of the pre-treated catalyst indicated advanced oxygen reduction properties. At the same time, kinetic current density figures obtained from the KL plots showed that H_2O_2 treatment leads to about 10 times higher

kinetic activity, while HNO₃ treatment was associated with lower kinetic activity in contrast to the non-treated and commercial samples.

SEM microscopy of Pt/XC-72R (H₂O₂ treated) catalyst confirmed the presence of Pt nanoparticles on carbon and NP size was estimated to be between 2.93 and 4.46 nm. The optimum (4.4 nm) size for enhanced mass activity is within the range observed in this study [18]. Concerning the XRD results, all synthesized samples (except commercial Pt/C) were associated with FCC polycrystalline Pt reflection planes with major peaks at 40° and 46° 2θ. Crystallite size was calculated to be 3.9 nm for H₂O₂-treated material and 5.0 nm for the nitric acid-treated sample while the non-treated catalyst was in the range of 3.6 nm. This suggests that HNO₃ treatment of XC-72R results in catalysts with high particle size, while H₂O₂ treatment leads to a minimal increase in particle size. Comparison of I_p/I_c ratio showed that Pt/XC-72R (H₂O₂ treated) catalyst material contains Vulcan carbon with less structural order and more defects in comparison to non-treated material which is desirable due to better Pt utilization connected with a higher number of defects. In relation to the nitric acid-treated sample, the crystal structure was assumed to be slightly more ordered although the peak intensities were analogous to that of the H₂O₂ treated catalyst. Despite having the maximum ratio value, the N-doped catalyst's intensity levels were close to the commercial sample indicating a more ordered structure and fewer defects. This means that N-doping did not have much effect on the morphology of XC-72R. To conclude, it was found that H₂O₂ pre-treatment of XC-72R results in a substantial increase in the catalytic activity of the final Pt catalyst for ORR.

Acknowledgements The work was financed by Estonian Research Council (PSG 312, EAG271 and PUTJD1233 grants) and ERA.Net RUS Plus grant "HeDoCat."

Author Contribution EN: Writing the manuscript draft, electrochemical measurements and comments; MG, VM and PW: Physical characterization and comments; SR and IK: Project administration—review & editing. All authors reviewed the manuscript.

Data Availability No datasets were generated or analysed during the current study.

Declarations

Conflict of interests The authors declare no competing interests.

References

- Solomon S, Plattner GK, Knutti R, Friedlingstein P (2009) Irreversible climate change due to carbon dioxide emissions. *Proc Natl Acad Sci U S A* 106:1704–1709. https://doi.org/10.1073/PNAS.0812721106/SUPPL_FILE/0812721106SI.PDF
- Wee JH (2010) Contribution of fuel cell systems to CO₂ emission reduction in their application fields. *Renew Sustain Energy Rev* 14:735–744. <https://doi.org/10.1016/J.RSER.2009.10.013>
- Thompson ST, James BD, Huya-Kouadio JM et al (2018) Direct hydrogen fuel cell electric vehicle cost analysis: System and high-volume manufacturing description, validation, and outlook. *J Power Sources* 399:304–313. <https://doi.org/10.1016/J.JPOWSOUR.2018.07.100>
- Andrade TS, Thiringer T (2024) Low platinum fuel cell as enabler for the hydrogen fuel cell vehicle. *J Power Sources* 598:234140. <https://doi.org/10.1016/J.JPOWSOUR.2024.234140>
- Kobayashi A, Fujii T, Takeda K et al (2022) Effect of Pt Loading percentage on carbon blacks with large interior nanopore volume on the performance and durability of polymer electrolyte fuel cells. *ACS Appl Energy Mater* 5:316–329. https://doi.org/10.1021/ACSAEM.1C02836/ASSET/IMAGES/LARGE/AE1C02836_0011.JPG
- Kumar SMS, Hidyatai N, Herrero JS et al (2011) Efficient tuning of the Pt nano-particle mono-dispersion on Vulcan XC-72R by selective pre-treatment and electrochemical evaluation of hydrogen oxidation and oxygen reduction reactions. *Int J Hydrogen Energy* 36:5453–5465. <https://doi.org/10.1016/J.IJHYDENE.2011.01.124>
- Holade Y, Sahin NE, Servat K et al (2015) Recent advances in carbon supported metal nanoparticles preparation for oxygen reduction reaction in low temperature fuel cells. *Catalysts* 5:310–348. <https://doi.org/10.3390/CATAL5010310>
- Moreno-Castilla C, Ferro-García MA, Joly JP et al (1995) Activated carbon surface modifications by nitric acid, hydrogen peroxide, and ammonium peroxydisulfate treatments. *Langmuir* 11:4386–4392. https://doi.org/10.1021/LA00011A035/ASSET/LA00011A035.FP.PNG_V03
- Najafi E, Ratso S, Foroozan A et al (2024) Functionalization of CO₂-derived carbon support as a pathway to enhancing the oxygen reduction reaction performance of Pt electrocatalysts. *Energy Fuels*. https://doi.org/10.1021/ACS.ENERGYFUELS.4C02407/SUPPL_FILE/EF4C02407_SI_001.PDF
- Debe MK (2012) Electrocatalyst approaches and challenges for automotive fuel cells. *Nature* 486(7401):43–51. <https://doi.org/10.1038/nature11115>
- Bard AJ, Faulkner LR (2000) *Electrochemical Methods: Fundamentals and Applications*, 2nd ed. WILEY
- Marković NM, Gasteiger HA, Grgur BN, Ross PN (1999) Oxygen reduction reaction on Pt(111): effects of bromide. *J Electroanal Chem* 467:157–163. [https://doi.org/10.1016/S0022-0728\(99\)00020-0](https://doi.org/10.1016/S0022-0728(99)00020-0)
- Zhao Y, Chu Y, Ju X et al (2018) Carbon-supported copper-based nitrogen-containing supramolecule as an efficient oxygen reduction reaction catalyst in neutral medium. *Catalysts* 8:53. <https://doi.org/10.3390/CATAL8020053>
- Zhang W, Shaikh AU, Tsui EY, Swager TM (2009) Cobalt porphyrin functionalized carbon nanotubes for oxygen reduction. *Chem Mater* 21:3234–3241. https://doi.org/10.1021/CM900747T/SUPPL_FILE/CM900747T_SI_001.PDF
- Kim JH, Kim YT, Joo SH (2020) Electrocatalyst design for promoting two-electron oxygen reduction reaction: Isolation of active site atoms. *Curr Opin Electrochem* 21:109–116. <https://doi.org/10.1016/J.COELEC.2020.01.007>
- Shinagawa T, Garcia-Esparza AT, Takanabe K (2015) Insight on Tafel slopes from a microkinetic analysis of aqueous electrocatalysis for energy conversion. *Sci Rep* 5:13801. <https://doi.org/10.1038/srep13801>

17. Holewinski A, Linic S (2012) Elementary mechanisms in electrocatalysis: revisiting the ORR tafel slope. *J Electrochem Soc* 159:H864–H870. <https://doi.org/10.1149/2.022211JES>
18. Xu Z, Zhang H, Zhong H et al (2012) Effect of particle size on the activity and durability of the Pt/C electrocatalyst for proton exchange membrane fuel cells. *Appl Catal B* 111–112:264–270. <https://doi.org/10.1016/J.APCATB.2011.10.007>
19. Li Z, Deng L, Kinloch IA, Young RJ (2023) Raman spectroscopy of carbon materials and their composites: Graphene, nanotubes and fibres. *Prog Mater Sci* 135:101089. <https://doi.org/10.1016/J.PMATSCI.2023.101089>

Publisher's Note Springer Nature remains neutral with regard to jurisdictional claims in published maps and institutional affiliations.

Springer Nature or its licensor (e.g. a society or other partner) holds exclusive rights to this article under a publishing agreement with the author(s) or other rightsholder(s); author self-archiving of the accepted manuscript version of this article is solely governed by the terms of such publishing agreement and applicable law.

Authors and Affiliations

Erkin Najafli¹ · Maarja Grossberg² · Valdek Mikli² · Peter Walke² · Sander Ratso¹ · Ivar Kruusenberg¹

✉ Ivar Kruusenberg
ivar.kruusenberg@kbfi.ee

² Department of Materials and Environmental Technology,
Tallinn University of Technology, Ehitajate Tee 5,
19086 Tallinn, Estonia

¹ National Institute of Chemical Physics and Biophysics,
Akadeemia Tee 23, 12618 Tallinn, Estonia

Curriculum vitae

Personal data

Name: Erkin Najafli
Date of birth: 05.01.1997
Place of birth: Azerbaijan
Citizenship: Azerbaijan

Contact data

E-mail: neceflierkin@gmail.com

Education

2020–2025 Tallinn University of Technology, PhD
2018–2020 Tallinn University of Technology, Materials and Processes for Sustainable Energetics, MSc
2013–2017 Azerbaijan State Oil and Industrial University, Electrical and Power Engineering, BSc
2002–2013 Secondary school No. 12, high school

Language competence

Azerbaijani Native
English Fluent
Turkish Fluent
Estonian Intermediate

Professional employment

2023–present Interuniversity Microelectronics Centre (IMEC), research and development engineer
2021–2023 National Institute of Chemical Physics and Biophysics, early-stage researcher

Participation in conferences

2023 Poster presentation at 74th Annual Meeting of the International Society of Electrochemistry (Lyon, France)

List of publications:

1. **Erkin Najafli**, Maarja Grossberg, Valdek Mikli, Peter Walke, Sander Ratso, Ivar Kruusenberg, Optimizing Pt Catalyst Performance for Oxygen Reduction Reaction via Surface Functionalization of Vulcan XC-72R Carbon Black Support Journal of Applied Electrochemistry 2025, in press. DOI: 10.1007/s10800-024-02238-1.
2. **Erkin Najafli**, Sander Ratso, Yurii P. Ivanov, Matija Gatalo, Luka Pavko, Can Rüstü Yörük, Peter Walke, Giorgio Divitini, Nejc Hodnik, and Ivar Kruusenberg, Sustainable CO₂-Derived Nanoscale Carbon Support to a Platinum Catalyst for Oxygen Reduction Reaction ACS Applied Nano Materials 2023 6 (7), 5772–5780 DOI: 10.1021/acsnm.3c00208
3. **Erkin Najafli**, Sander Ratso, Amir Foroozan, Navid Noor, Drew C. Higgins, and Ivar Kruusenberg, Functionalization of CO₂-Derived Carbon Support as a Pathway to Enhancing the Oxygen Reduction Reaction Performance of Pt Electrocatalysts Energy & Fuels 2024 38 (16), 15601–15610 DOI: 10.1021/acs.energyfuels.4c02407

Elulookirjeldus

Isikuandmed

Nimi: Erkin Najafli
Sünniaeg: 05.01.1997
Sünnikoht: Aserbaidžaan
Kodakondsus: Aserbaidžani

Kontaktandmed

E-post: neceflerkin@gmail.com

Hariduskäik

2020–2025 Tallinna Tehnikaülikool, PhD
2018–2020 Tallinna Tehnikaülikool, Materjalid ja protsessid jätkusuutlikus
energeetikas, MSc
2013–2017 Aserbaidžaaani Riiklik Nafta ja Tööstusülikool, elektri ja
energeetikatehnika, BSc
2002–2013 Keskkool nr 12, keskharidus

Keelteoskus

Aserbaidžaaani keel emakeel
Inglise keel kõrgtase
Türgi keel kõrgtase
Eesti keel kesktase

Teenistuskäik

2023 – ... Interuniversity Microelectronics Centre (IMEC),
teadus- ja arendusinsener
2021–2023 Keemilise ja bioloogilise füüsika instituut, nooremteadur

Osalemine konverentsidel

2023 Posterettekannepostitus Rahvusvahelise Elektrokeemia Seltsi 74.
aastakoosolekul (Lyon, Prantsusmaa)

Teadustegevus

Teadusartiklite ja konverentsiettekannete loetelu on toodud inglisekeelse elulookirjelduse juures.

ISSN 2585-6901 (PDF)
ISBN 978-9916-80-292-2 (PDF)